INTERIM REPORT

Hand-Held UXO Discriminator

SERDP Project MR-1667

SEPTEMBER 2010

Erika Gasperikova
Lawrence Berkeley National Laboratory

This document has been cleared for public release

SERDP
DOD • EPA • DOE

Disclaimer

This document was prepared as an account of work sponsored by the United States Government. While this document is believed to contain correct information, neither the United States Government nor any agency thereof, nor The Regents of the University of California, nor any of their employees, makes any warranty, express or implied, or assumes any legal responsibility for the accuracy, completeness, or usefulness of any information, apparatus, product, or process disclosed, or represents that its use would not infringe privately owned rights. Reference herein to any specific commercial product, process, or service by its trade name, trademark, manufacturer, or otherwise, does not necessarily constitute or imply its endorsement, recommendation, or favoring by the United States Government or any agency thereof, or The Regents of the University of California. The views and opinions of authors expressed herein do not necessarily state or reflect those of the United States Government or any agency thereof or The Regents of the University of California.

Ernest Orlando Lawrence Berkeley National Laboratory is an equal opportunity employer.

TABLE OF CONTENT

1. INTRODUCTION **4**

2. TECHNOLOGY DESCRIPTION **6**

3. DEMONSTRATION SURVEY **11**

4. DATA ANALYSIS AND INTERPRETATION **13**

4.1 TRAINING DATA 13
4.2 CALIBRATION GRID 14
4.3 BLIND TEST GRID 17

5. PERFORMANCE ASSESSMENT **23**

5.1 STATISTICAL APPROACH - EMPIRICAL LIKELIHOOD RATIO METHOD 23
5.2 TEMPLATE-MATCH APPROACH 28

6. CONCLUSIONS **32**

7. ACKNOWLEDGMENTS **33**

8. REFERENCES **33**

9. ACRONYMS **35**

TABLE 1 ..... **36**

APPENDIX 1 ..... **37**

1. INTRODUCTION

In 2003, the Defense Science Board observed: "The … problem is that instruments that can detect the buried UXOs also detect numerous scrap metal objects and other artifacts, which leads to an enormous amount of expensive digging. Typically 100 holes may be dug before a real UXO is unearthed! The Task Force assessment is that much of this wasteful digging can be eliminated by the use of more advanced technology instruments that exploit modern digital processing and advanced multi-mode sensors to achieve an improved level of discrimination of scrap from UXOs." In keeping with these remarks and with prior funding (UX-1225, MM-0437, and MM-0838), the LBNL group has successfully designed and built the cart-mounted Berkeley UXO Discriminator (BUD) and demonstrated its performance at various test sites (cf. Gasperikova et al., 2007, 2008, and 2009).

Because hand-held systems have the advantage of being lightweight, compact, portable, and deployable under most site conditions, they are particularly useful in areas of dense vegetation or challenging terrain. In heavily wooded areas or areas with steep or uneven terrain, hand-held sensors may be the only suitable device for UXO detection and discrimination because it can be carried through spaces that the operator could walk through or at least approach. Furthermore, it is desirable to find and characterize a metallic object without the need to accurately locate the sensors at multiple positions around the target. The ideal system would thus locate and characterize the target from a single position of the sensor and indicate to the operator where to flag the target for subsequent study.

Based on these considerations, we designed and built a sensor package in a shape of a 14-in (0.35 m) cube. This hand-held prototype incorporates the key features of the cart-mounted system – (a) three orthogonal transmitters and ten pairs of receivers, and (b) difference or gradient measurements that significantly reduce the ambient and motion noise, and greatly enhance the sensitivity to the gradients of the target. The system characterizes the target from a single position. Results from a local test site were in a good agreement with theoretical performance calculations of such a device. This survey was designed to demonstrate performance of the system under realistic survey conditions at the Aberdeen Proving Ground (APG) in Aberdeen, MD. The survey was preformed in an area with known items ("Calibration Grid"), and in a seeded blind test area (the "Blind Test Grid"). The ground truth for the surveys conducted on the Blind Test Grid was withheld from the testers. Only the graded test scores based on target detection and target classification were provided. For more information, see http://aec.army.mil/usaec/technology/uxo01c03.html.

2. TECHNOLOGY DESCRIPTION

The SERDP and ESTCP have supported LBNL in development of a device that not only detects the object itself but also quantitatively determines its size, shape, and orientation. In a hand-held system the sensor package must be easily maneuvered over rough terrain, through brush, etc. A useful criterion might be that it could be carried through spaces that the operator could traverse or at least approach. To avoid the reliance on accurate multiple positioning of any system it has been shown that (1) the object must be illuminated with three different polarizabilities of the transmitted field and that (2) to determine its location from a single position of the transmitter-receiver system multiple receivers must be used. To accommodate the first requirement a hand-held design incorporates three orthogonal transmitter loops much like the cart-mounted system. To accommodate the second requirement the hand-held UXO discriminator uses ten pairs of receivers. The same discrimination abilities afforded by the cart-mounted system are available in the hand-held unit albeit with slightly reduced depth of detection. The hand-held UXO discriminator is able to discriminate small (20 mm) objects at a depth of 0.45 m and large (105 and 155 mm) objects at a depth of 0.85 m and to detect them down to 1.15 m. The hand-held prototype is shown in Figure 1. The transmitter-receiver configuration is shown in Figure 1a while the assembled transmitter-receiver cube is shown in Figure 1b.

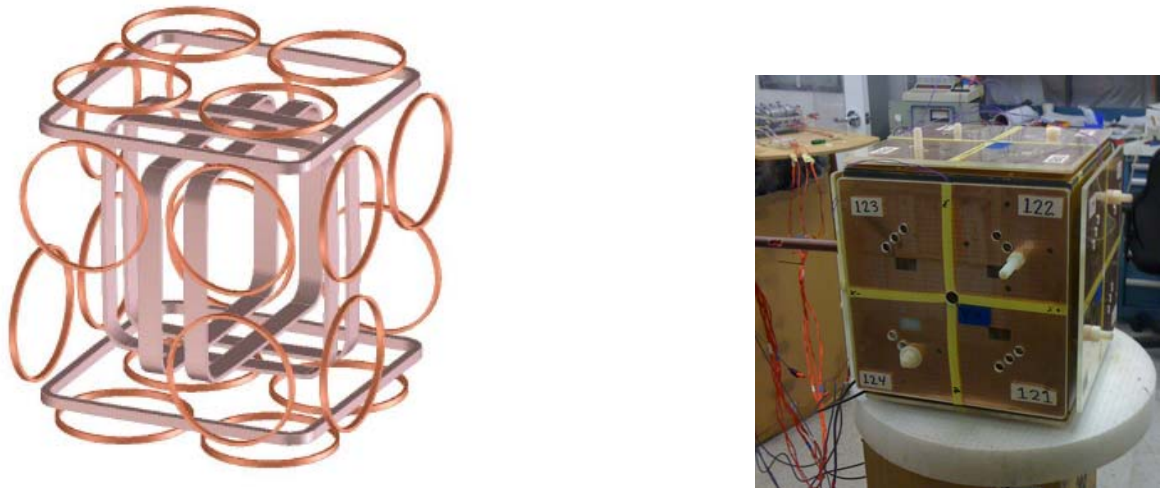

Figure 1. LBNL Hand-held UXO Discriminator - (a) transmitter-receiver array configuration, (b) assembled prototype.

The hand-held UXO discriminator employs three orthogonal transmitters and ten pairs of differenced receivers. Each vertical face of the cube has three induction coils, while the two horizontal faces have four induction coils, each sensitive to the magnetic field component normal to the face. Receivers on opposite faces of the cube are paired along the symmetry lines through the center of the system and each pair sees identical fields during the on-time of current pulses in the transmitter coils. They are wired in opposition to produce zero output during the on–time of the pulses in three orthogonal transmitters. This configuration dramatically reduces noise in measurements by canceling background electromagnetic fields (these fields are uniform over the scale of the receiver array and are consequently nulled by the differencing operation), and by canceling noise contributed by the tilt of the receivers in the Earth's magnetic field, thus greatly enhances receivers' sensitivity to gradients of the target response.

The transmitter coils are powered separately from the data acquisition board. Pulsers provide resonant circuit switching to create bi-polar half-sine pulses of 300 μs width. The current has a

~40 A peak and a resonant circuit voltage of ~400 Volts. The operational overall half-sine duty cycle is ~12%. Transients are digitized with a sampling interval of 4 μs. The sensors are critically damped 5-inch coils with a self-resonant frequency of 75 kHz. Data acquisition is performed on a single board. This board has 12 high-speed ADC channels for the output. Ten of these channels are used for the signal from receiver coils, and the remaining two channels provide information about the system (i.e. tilt information, transmitter current).

An important feature of the hand-held UXO discriminator is an inversion algorithm, which is used to determine target properties from measurements with a given transmitter-receiver configuration. At any given time the response is inverted to yield the location (x, y, z) of the target, its attitude and its principal polarizabilities, which yield an apparent aspect ratio. Signal-to-noise (S/N) estimates (or measurements) are interpreted in this inversion to yield error estimates on the location, attitude and polarizabilities.

It has been demonstrated that a satisfactory classification scheme is one that determines the principal dipole polarizabilities of a target – a near intact UXO displays a single major polarizability coincident with the long axis of the object and two equal transverse polarizabilities. The induced moment of a target depends on the strength of the transmitted inducing field. The moment normalized by the inducing field is the polarizability. This description of the inherent polarizabilities of a target is a key in discriminating UXO from irregular scrap metal. Figures 2 and 3 illustrate a discrimination capability of the system for UXO object and a scrap metal, respectively. While UXO objects have a single major polarizability coincident with the long axis of the object and two equal transverse polarizabilities (Figure 2), scrap metal exhibits three

distinct principal polarizabilities (Figure 3). There are clear distinctions between symmetric intact UXO and irregular scrap metal. Moreover, UXO have unique polarizability signatures, and thus distinctions can be made among various UXOs.

Object orientation and equivalent dipole polarizability estimates of large and shallow UXO or scrap are more problematic as they are affected by higher order (non-dipole) terms induced in objects due to source field gradients along the length of the objects. In the case of the large and shallow objects, the hand-held system can be easily raised an appropriate distance above the object such that the dipole model approximation for polarizability estimates is appropriate.

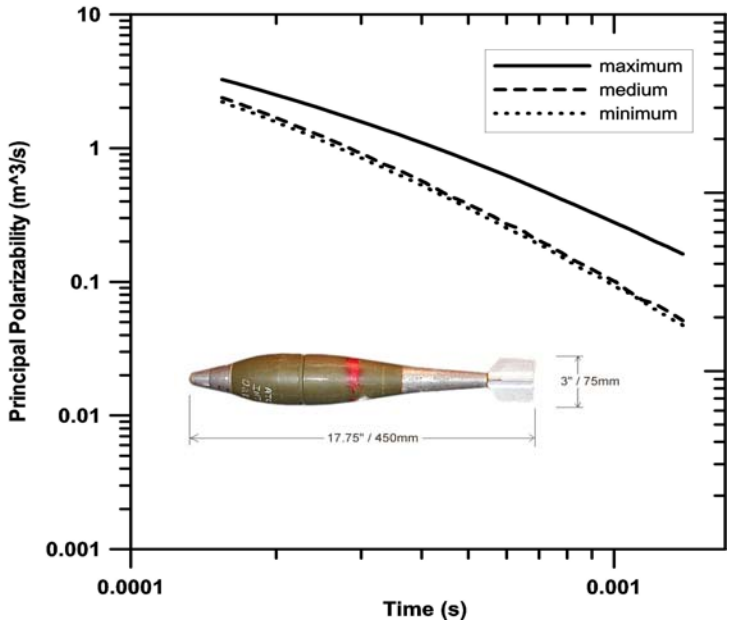

Figure 2. Inversion results for the principal polarizabilities of 81 mm mortar.

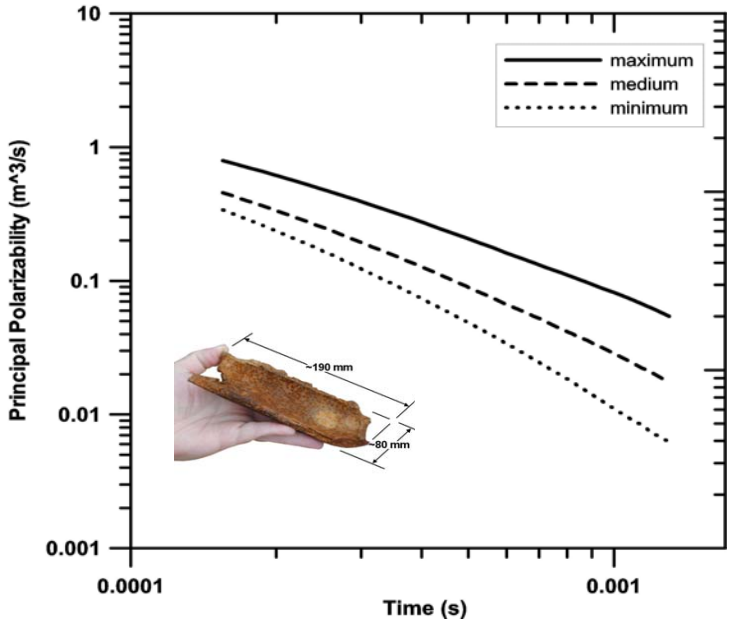

Figure 3. Inversion results for the principal polarizabilities of 19x8 cm scrap metal.

3. DEMONSTRATION SURVEY

The demonstration survey was performed between June 21, 2010 and July 1, 2010. The hand-held UXO discriminator was operated in a cued mode. The system was brought to marked locations and run in the characterization/discrimination mode. The three discriminating polarizability responses along with the object depth and horizontal location with respect to the center of the bottom plane of the cube were recorded and visually presented on the computer screen. Additional values recorded at each location were the S/N ratio, and a polarizability index, which is an average value of the product of time (in seconds) and polarizability rate (in m^3/s) over the 46 sample times logarithmically spaced from 80 to 1460 μs. The survey took two weeks. The schedule accommodated partial days when the base was closed. We had a one-day delay because of a problem with the system. An unusual and unexpected heat wave made the first half of the survey extra challenging. The system performed well, and we collected a high quality data. Figure 4 illustrates the deployment of the hand-held UXO discriminator in the field.

Figure 4. LBNL hand-held UXO discriminator at APG.

The Calibration Grid consists of 66 cells 4 m on a side arranged in 11×6 layout (A-K and 1-6). The APG personnel marked all 66 cell centers locations with plastic pin flags. These cells contain 14 different munitions types (from 20 mm projectile to 155 mm projectile), and eight representative clutter items buried at various orientations and depths. The shallowest object is a horizontal 40 mm projectile at 0.0 m depth, and the deepest object is a horizontal 155 mm projectile at 1.08 m depth. We took measurements along lines 2 m apart, with a 2 m distance between the measurements on each line. In addition to soundings at centers of grid cells, we collected data at 0.15 m before and 0.15 m after cell centers along survey lines. When polarizability inversions didn't agree in appearance, provided that the central sounding had S/N larger than four, eight additional soundings were acquired, at 0.3 m and 0.5 m offset on the arms of a cross, centered on the cell center.

The Blind Test Grid is 40×40 m area. The individual cells are 1×1 m with an empty 1×1 m cells in between. There are 400 opportunities/flags arranged in 20×20 layout (A-T and 1-20). Again, all 400 points were marked with plastic pin flags. The Blind Test Grid is made up of six different types of munitions and clutter found in the Calibration Grid, and in the direct and indirect fire sub-areas of the Open Field. We took measurements along the lines 1 m apart, with a 1 m distance between the measurements on each line. In addition to soundings at the test grid cell centers, we collected data at 0.15 m before and 0.15 m after cell centers along the survey lines. When polarizability inversions didn't agree in appearance, provided that the central sounding had S/N larger than four, eight additional soundings were acquired, at 0.3 m and 0.5 m offset on the arms of a cross, centered on the cell center.

4. DATA ANALYSIS AND INTERPRETATION

Ten channels of field data were recorded at a rate of 250 k-samples/second for each of three transmitters. Field data were stacked together in a field programmable gate array (FPGA) and transferred to a field computer (laptop) forming a primitive stack. An even number of primitive stacks was averaged together to form stacked data for further processing. The peak transmitter current was estimated from the stacked transmitter current channel record, and the data were normalized by that value. Nominal transmitter shut-off time was estimated, and induction responses were computed at 46 logarithmically spaced times between 80 and 1460 μs, averaged in half-sine windows with widths 10% the center time after transmitter pulse shut-off. Responses were differenced with background responses collected over an area determined to be free of metallic objects. The resulting 30 channels of normalized responses were then inverted for a candidate object position and principal polarizabilities as a function of time after transmitter shut-off.

4.1 Training Data

The empirical densities for UXO and scrap classes are derived from the training data. The UXO class training data included polarizability responses collected over UXO at the local test facility as well as at the APG Calibration Grid. Both sets contain responses from 14 different munition types (from 20 mm projectile to 155 mm projectile) buried at various orientations and depths. These responses are considered reliable at observation times from 80 μs to 1460 μs after the

extinction of the primary field. These were supplemented with an approximately equal number of additional UXO polarizability responses previously collected using the cart-mounted system (BUD). Adding them to the training data allowed for better estimates of the densities of polarizability responses. For the scrap response class, the responses from the APG Calibration Grid were supplemented with BUD scrap responses from previous surveys at Camp Sibert, AL, and San Luis Obispo, CA. The BUD responses are considered reliable from 140 μs to 1400 μs. To extend them to the window of the hand-held prototype responses, least squares predictions of responses and suitable noise was based on the responses from the original BUD time window, with prediction coefficients based on the hand-held responses.

4.2 Calibration Grid

The Calibration Grid is 44×24 m area with cells in 11×6 layout. All 66 centers were marked with plastic flags, since at the moment our system doesn't have GPS navigation capabilities. We took measurements along lines 2 m apart, with a 2 m distance between the measurements on each line. In addition to the soundings at the grid cell centers, we collected data at 0.15 m before and 0.15 m after the cell center along the survey lines. The soundings were differenced with the background reference soundings taken within the previous 30-40 minutes at a nearby site determined by the field operator to be free from metallic objects. An estimate of S/N was made based on signal levels relative to median drift amounts recorded during the tests at our field test facility in California (Richmond Field Station, RFS). The estimate is

$$S/N = \rho^{-1} \frac{1}{N} \sum_{ijk}^{N} \rho\left(\frac{|S_{ijk}|}{\text{median}_{ijk}}\right)$$

where $\rho(r)$ is the negative of a log likelihood function estimated from median normalized system drifts between reference soundings taken before and after UXO soundings, $\rho(r)^{-1}$ is its inverse, S_{ijk} is the signal at the i'th time in the j'th receiver pair in the response to the k'th transmitter, $median_{ijk}$ is the median absolute value of the drift for the ijk'th time receiver pair and transmitter combination in the stability measurements, N is the product of the number of receiver pairs (10), the number of transmitters (3), and the number of response time averages considered (46), which is used also for the summation.

The Calibration Grid S/N map is shown in Figure 5. The recovered responses (66) of the objects at the center of each cell were used as the training data for the Blind Test Grid objects discrimination and identification. The polarizability plots of these objects are shown in Appendix 1. The title of the plot consists of a prefix CAL indicating that data are from the Calibration Grid, followed by the x cell location (x goes from 0 to 44 m, from left to right, which is a west-east direction in Figure 5), followed by the y cell location (y goes from 0 to 24 m, from top to bottom, which is a north-south direction in Figure 5). The rest of the file name can be ignored – Run and four-digit number is a counter that guarantees uniqueness of the file name, and various extensions between periods indicate a sequence of the files used in the inversion. For example, CAL−x34−y22−Run−0346.bin−diff.avg.inv is a response of the cell with x=34 m and y=22 m, which is the cell I6. We took additional sub-grid measurements around the cell center when recovered polarizabilities significantly departed from a nominal response of the object in that cell or S/N was too low. Based on our detection threshold of S/N less than four, cell C3 would be considered empty, while in reality it contained a small piece of scrap. Cells with S/N between four and six, which were considered as “can’t analyze” in our analysis, were H4 (60 mm mortar

at 0.6 m depth) and K4 (105 mm projectile at 1.05 m depth). Cell A6 contained the deepest object – 155 mm projectile at 1.08 m depth. Based on our previous measurements this would produce a low S/N. However, because of a surface nearby metallic object, this cell S/N was high, although we were not able to identify this deep object correctly.

If one compares the object depths estimated by the inversion algorithm and the true object depths, 56% of the object depths were within ±0.05 m, 33% were between 0.05 and 0.15 m, and 11% had the depth differences more than 0.15 m. The cells with the largest difference in the object depth were E5, G3, J2, and J3. Cells A6, H4, and K4 that we could not analyze also fall into this category.

Table 1 shows the Calibration Grid discrimination results. The first column is the cell name; the second column is the calculated probability of being UXO (p(UXO)) (anything with p(UXO)>0.0005 was considered as UXO, 9999 indicates data in "can't analyze" category); the third column is the estimated object depth; the forth column is the object identification by our algorithm; the fifth column is the ground truth; the sixth column is the true object depth; the seventh column is the file used for the analysis (this is the same as the plot title in the Appendix 1).

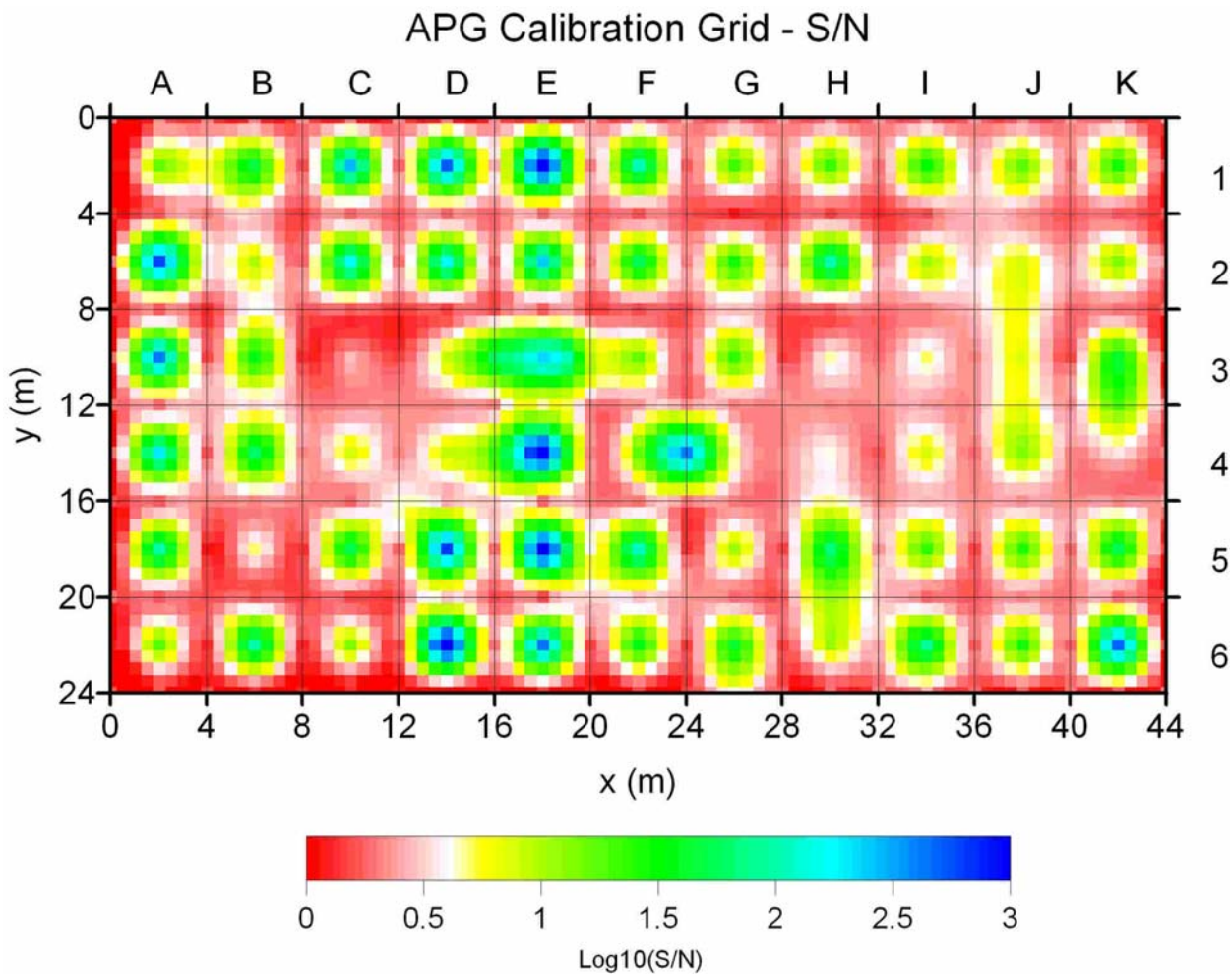

Figure 5. Signal-to-noise ratio map of the APG Calibration Grid. Colors are plotted on a logarithmic scale for better visibility. The detection threshold of S/N=4 is equal to 0.6 on the logarithmic scale.

4.3 Blind Test Grid

The soundings were collected at the test grid cell centers (400 opportunities), and at 0.15 m before and 0.15 m after the cell center along the survey lines, with the system oriented in a single direction. The soundings were differenced with the background reference soundings taken within the previous 30-40 minutes at a nearby site determined by the field operator to be free from metallic objects. The estimate of S/N was calculated as described above. The cells with S/N

values greater than four were considered occupied. When S/N values were over 400 the system was either raised 0.2 m or 0.4 m, or moved away by 0.25 and 0.5 m to reduce the S/N below 400 and the measurements were repeated.

When polarizability inversions from soundings taken at a common height agreed in appearance, then the sounding nearest laterally to the interpreted object was used for discrimination. Otherwise, provided that the central sounding had S/N larger than four, eight additional soundings were acquired, at 0.3 m and 0.5 m offset on the arms of a cross, centered on the cell center. When polarizability inversions from the soundings agreed in appearance then the sounding nearest to the interpreted object was used for discrimination. When a subset of inversions agreed in appearance then the subset member closest to the interpreted object was used for discrimination. When polarizability inversions from all soundings in a cell were of disparate appearance, multi-site inversion was performed on the soundings, and if it fit the data to better than 50% at the site closest to the interpreted object, the resultant dipole polarizabilities were used for discrimination, otherwise data from this cell were considered as “can’t analyze”. Similarly, any sounding with an estimated S/N below six, which our discrimination procedure estimated to be scrap, was considered as “can’t analyze”. The Blind Test Grid S/N map is shown in Figure 6. There are six types of UXO present at the APG Blind Test Grid - 25 mm, 37 mm, 60 mm, 81 mm, 105 mm (IF=indirect fire) projectiles, and 105 mm HEAT mortar (DF=direct fire).

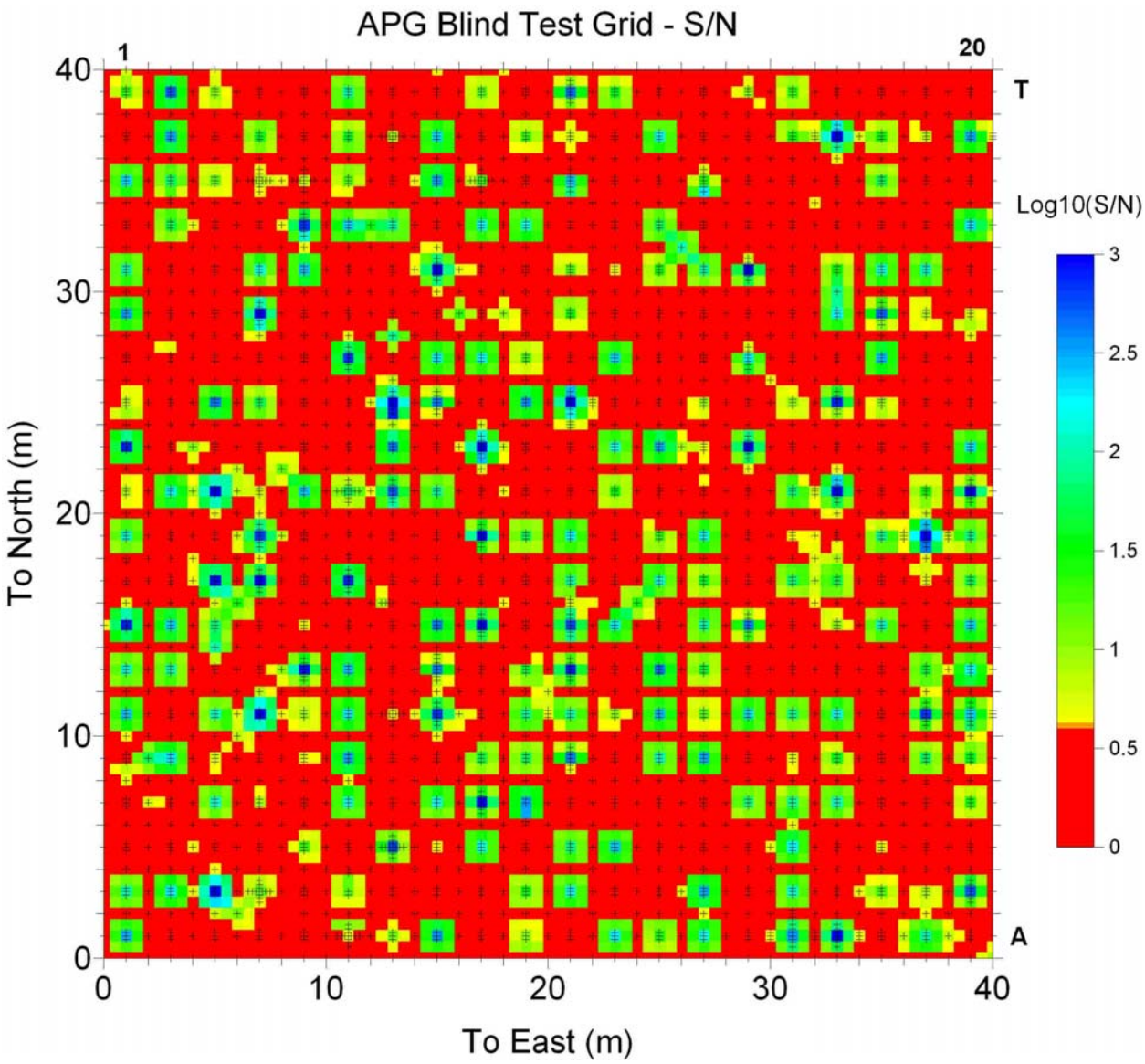

Figure 6. Signal-to-noise ratio map of the APG Blind Test Grid. Colors are plotted on a logarithmic scale for better visibility. The detection threshold of S/N=4 is equal to 0.6 on the logarithmic scale.

Principal polarizabilities from the soundings that have been selected for the discrimination were analyzed using a variant of the empirical likelihood ratio method (outlined in Gasperikova, et al. 2009). In the empirical likelihood ratio method, probability densities of principal polarizability

responses were estimated from the training data, previously collected UXO and scrap responses separately.

We condensed each polarizability response down to a set of n_{feat} = 10 numbers, nine of which were averages of products of major, intermediate, and minor principal polarizabilities with time, in three time bands. The logarithm of their vector magnitude was used as the tenth parameter, and the first nine values were normalized by that magnitude. Parameter vectors of this form were differenced with the vector of their component median values over the training data for their class (UXO or scrap) for use in forming damped trimmed covariance matrices C^{uxo} and C^{scrap}, for UXO and scrap responses, which were used in forming the empirical probability densities for UXO and scrap training data.

The empirical densities for polarizability responses of UXO and scrap were formed by centering a generalized Cauchy density at each of the different polarizability responses from the class and summing over the responses from the class. The generalized Cauchy density that was used for a class was based on the damped trimmed estimate of the response covariance matrix for the class C^{class}, with length scale reduced by a factor of $(n^{class})^{-1/n_{feat}}$, so that the contribution from each response filled $1/n^{class}$ of the volume occupied by the whole distribution, where n^{class} was the number of responses being summed over to form the density estimate. The overall form was

$$f^{(class)}(v_j^{(class)}) = K \sum_{i \text{ in class}} \frac{1}{\left[1 + (v_j^{(class)} - v_i^{(class)})^t (C^{(class)})^{-1} (v_j^{(class)} - v_i^{(class)}) \gamma (n^{(class)})^{2/n_{feat}}\right]^{m^{(class)}/2}}$$

where $\gamma = 0.2986/m^{class}$, and v_j was the vector point where the density was being evaluated, v_i were the training response vectors the density was based on, and K was

$$K = \frac{1}{2}\left(\frac{\gamma}{\pi}\right)^{n_{feat}/2} \frac{\Gamma(m^{class}/2)}{\Gamma(m^{class} - n_{feat}/2)} (\det(C^{(class)}))^{-1/2}$$

where $\Gamma()$ is the gamma function, and m^{class} was a parameter which was adjusted using cross validation to maximize the likelihood of the training data.

The probability that a response vector v_j is due to UXO is

$$p^{(uxo)}(v_j) = \frac{\alpha^2_{uxo} f^{(uxo)}(v_j)}{\alpha^2_{uxo} f^{(uxo)}(v_j) + \alpha^2_{scrap} f^{(scrap)}(v_j)}$$

where α^2_{uxo} and α^2_{scrap} are a priori relative probabilities of UXO and scrap, and only the ratio of $\alpha^2_{uxo}/\alpha^2_{scrap}$ is significant.

In artillery ranges where no cleanup has been done, assuming a dud rate of 0.1 and that ordnance is blown into five detectable pieces, a reasonable value for $\alpha^2_{uxo}/\alpha^2_{scrap}$ would be 0.02. However, in a small test grid, constructed to emphasize the ability of equipment to discriminate between UXO and scrap, it is reasonable to emplace a much higher ratio of UXO to scrap, such as 1:1, which would suggest using a value of $\alpha^2_{uxo}/\alpha^2_{scrap} = 1$. In our 2006 survey at the Yuma Proving Ground (YPG) Blind Test Grid we estimated there were 230 occupied cells and 183 UXO, yielding a UXO/scrap ratio of 183/47 suggesting using $\alpha^2_{uxo}/\alpha^2_{scrap} = 3.89$. Using this value, all responses with $p^{(uxo)}(v_j) \geq 0.0005$ were considered UXO. Probabilities estimated using the empirical likelihood ratio discrimination method tend to vary by orders of magnitude so the exact value of $\alpha^2_{uxo}/\alpha^2_{scrap}$ only affected four to six objects with $p^{(uxo)}$ near the cut-off value.

Just as UXO and scrap class polarizability response densities were estimated, we estimated densities for the polarizability responses of different types of UXO. However, due to the limited number of responses of individual UXO in our response library, we used the overall UXO trimmed covariance matrix estimate C^{uxo} in the place of individual UXO type covariance matrices in their estimated distributions. Similarly, for individual UXO types, in the generalized Cauchy density formula for the exponent m^{class} we used the exponent estimated for the overall distribution of UXO responses m^{uxo}. Given empirical distributions $f^{class_k}(v_j)$ for classes class_k, and a priori expectations of relative frequencies $\alpha^2_{class_k}$ for the different classes, the probability that a response is from an object in class_q is

$$p^{(class_q)}(v_j) = \frac{\alpha^2_{class_q} f^{(class_q)}(v_j)}{\sum_k \alpha^2_{class_k} f^{(class_k)}(v_j)}$$

Here, scrap was included as one of the classes in the denominator. For want of prior expectations as to the expected relative frequency of different UXO types, the different $\alpha^2_{class_k}$ were taken to be equal for all the classes except for scrap, and the sum of $\alpha^2_{class_k}$ over UXO classes was equal to the α^2_{uxo} above.

5. PERFORMANCE ASSESSMENT

For the hand-held prototype performance evaluation we submitted two tables with following information:

(a) cell is empty or occupied

(b) object depth below the system

(c) identification as a scrap or intact UXO

(d) if cell was identified as containing UXO, type of UXO

(e) cells with data that can't be analyzed.

The first approach was a statistical approach described in Chapter 4. The second approach was a template match approach. In both approaches the cell was considered empty if S/N was less than four, and "can't analyze" category if S/N was between four and six.

5.1 Statistical Approach - Empirical Likelihood ratio Method

The statistical approach used reprocessed data, and it is described in Chapter 4. In this approach from 400 flag/cell locations, eight were labeled as "can't analyze", and 178 were identified as empty, so the discrimination was done on 214 flags. From those, 32 were identified as scrap and safe to leave in the ground, and 182 were identified as UXO. This was based on the probability of being UXO (p(UXO)) larger or equal to 0.0005. If one would use p(UXO)>0.0015, the number of scrap metals would increase to 36. Figure 7 shows the empty cells in green, occupied cells in red, and "can't analyze" locations in blue. Figure 8 shows the location of UXO in red and

scrap in green. Figure 9 shows the recovered object depths. All objects in the Blind Test Grid were shallower than 0.5 m.

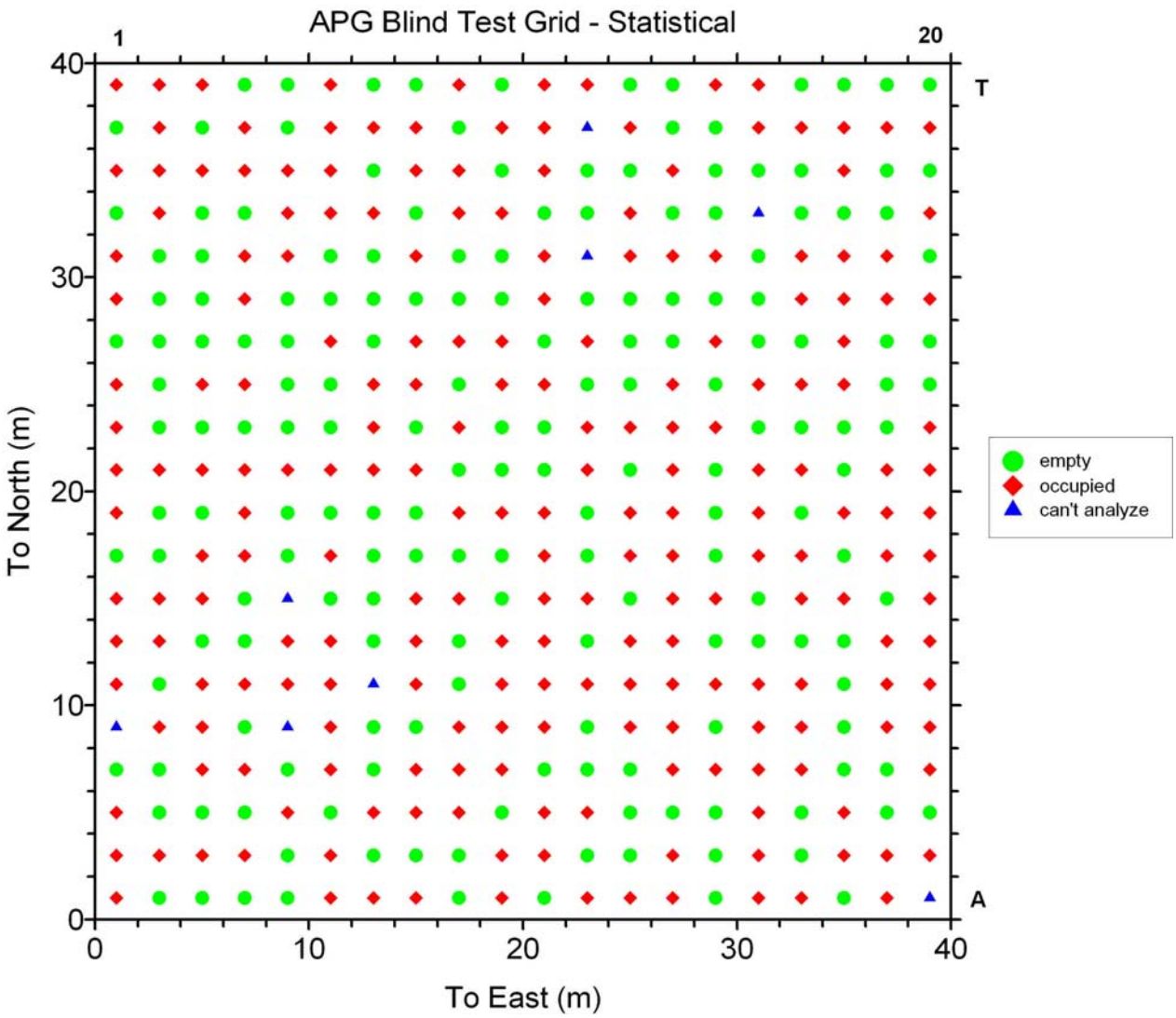

Figure 7. The APG Blind Test Grid cells identified as empty (green circle), occupied (red diamond) or "can't analyze" (blue triangle) using the statistical approach.

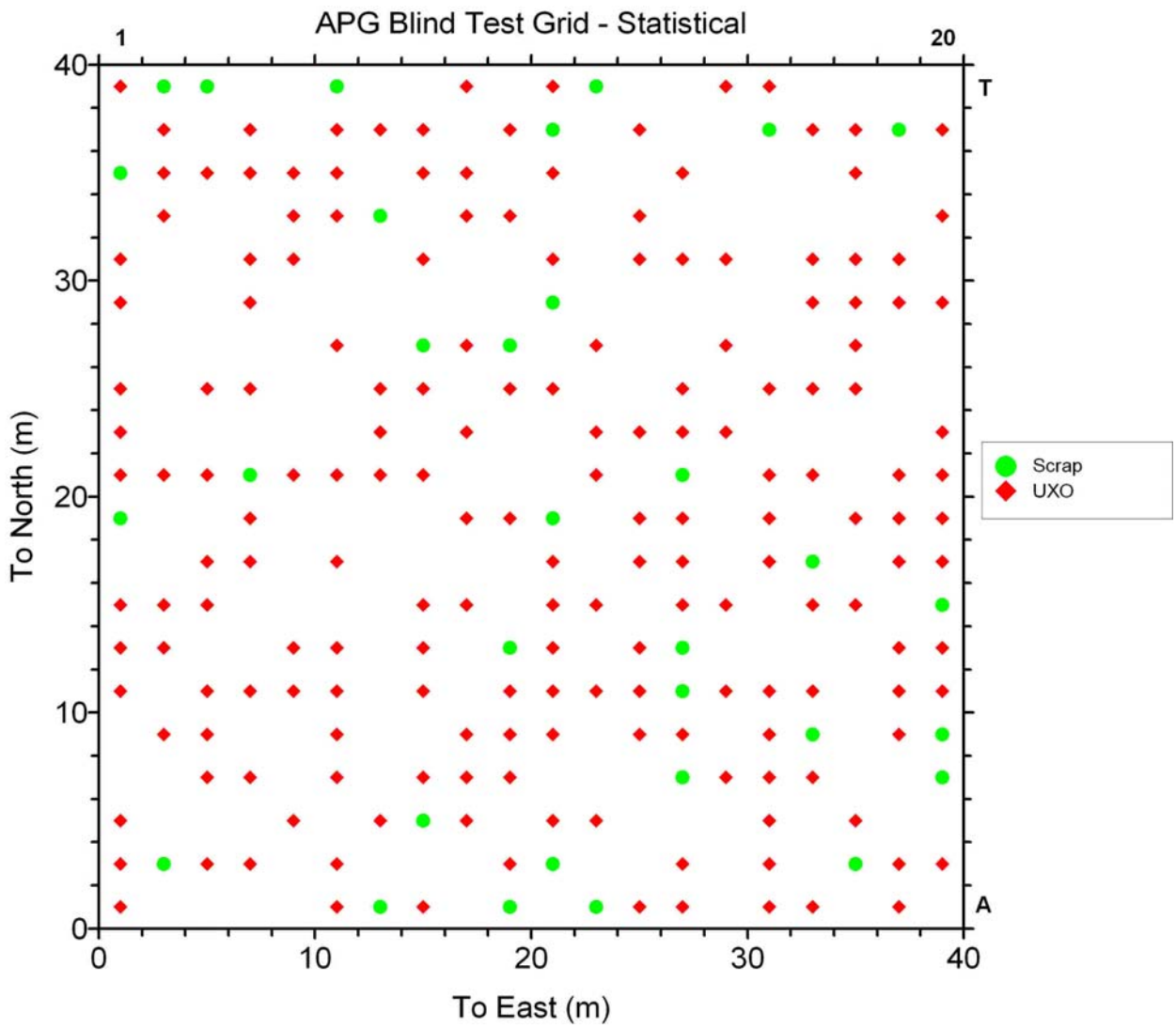

Figure 8. The APG Blind Test Grid cells identified as scrap (green circle) or UXO (red diamond) using the statistical approach.

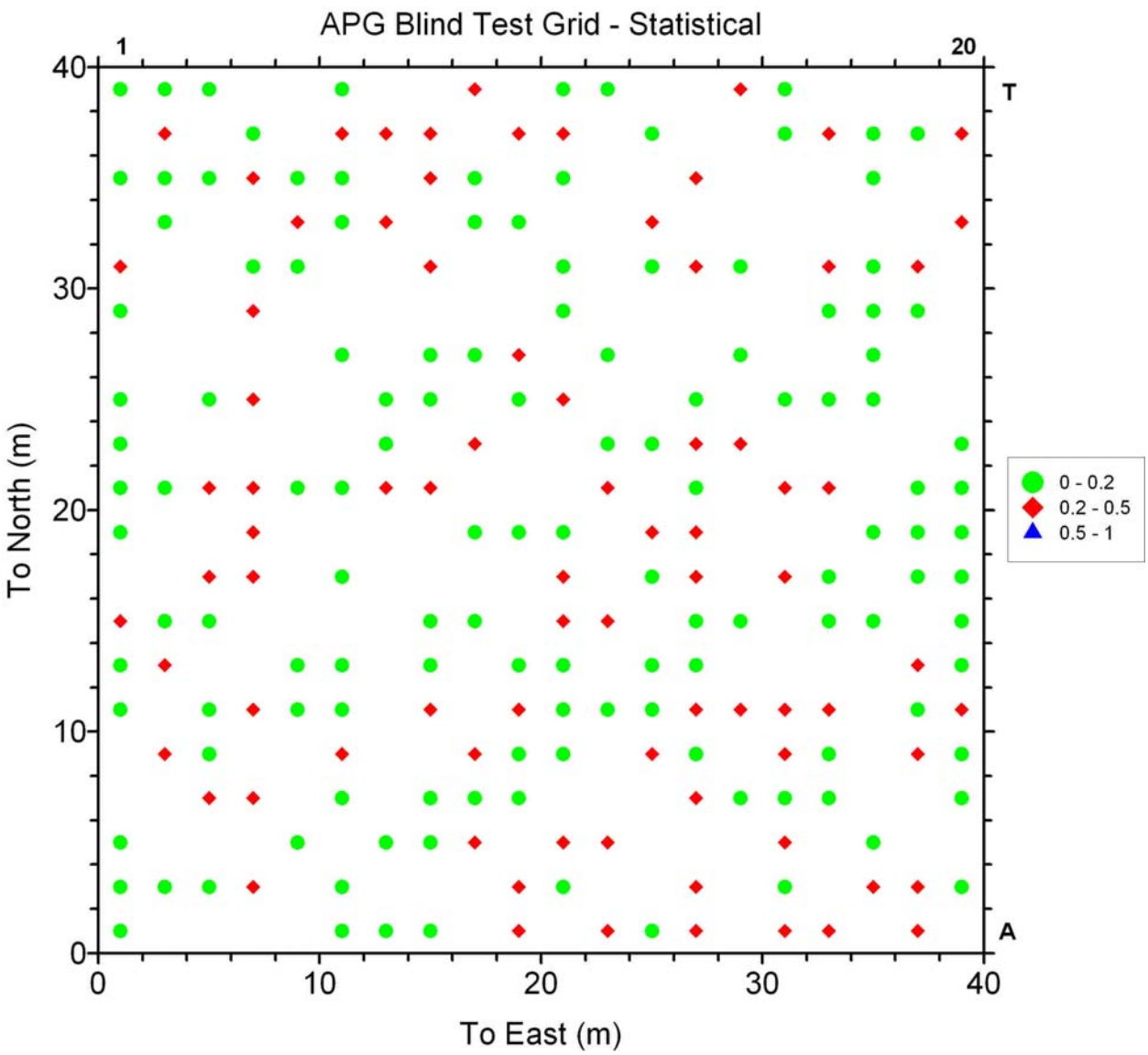

Figure 9. The APG Blind Test Grid – recovered object depths.

The scoring results are shown in Table 2. In this approach we correctly identified 96% and 94% of munitions in the response and discrimination stages, respectively. The objects missed were some of 60 mm, 81 mm, and 105 mm projectiles/mortars at the depth greater than eight times of the objects diameter. 98% of scrap was correctly identified in the response stage, and the probability of false positive in the discrimination stage was 0.77. The background alarm rates for the response and discrimination stages were 0.10 and 0.07, respectively. The efficiency rate at

the operating point was 0.99, with the false positive rejection rate of 0.21 and the background alarm rejection rate of 0.32. For the case with no loss in the UXO detection (the efficiency rate equal to 1.0), both false positive and background alarm rejection rates were zero; hence all detected objects would have to be dug out. Table 2b shows the Blind Test Grid correct UXO type classification of targets that were correctly discriminated as munitions. Overall 67% of munitions were classified correctly.

Table 2a. Blind Grid scoring results for the statistical approach

	Response Stage				**Discrimination Stage**			
Munitions[a] Scores	***P_d^{res}: by type***				***P_d^{disc}: by type***			
	All Types	**105-mm**	**81/60-mm**	**37/25-mm**	**All Types**	**105-mm**	**81/60-mm**	**37/25-mm**
	0.98	0.96	1.00	1.00	0.97	0.94	1.00	1.00
	0.96	0.90	0.97	1.00	0.94	0.87	0.97	1.00
	0.91	0.79	0.88	0.93	0.90	0.75	0.88	0.93
By Depth[b]								
0 to 4D	1.00	1.00	1.00	1.00	1.00	1.00	1.00	1.00
4D to 8D	1.00	1.00	1.00	1.00	1.00	1.00	1.00	1.00
8D to 12D	0.56	0.50	0.00	1.00	0.44	0.33	0.00	1.00
Clutter Scores	***P_{cd}***				***P_{fp}***			
By Mass								
By Depth[b]	**All Mass**	**0 to 0.25 kg**	**>0.25 to 1 kg**	**>1 to 10 kg**	**All Mass**	**0 to 0.25 kg**	**>0.25 to 1 kg**	**>1 to 10 kg**
All Depth	0.99				0.82			
	0.98	0.95	1.00	1.00	0.77	0.71	0.79	1.00
	0.95				0.71			
0 to 0.15 m	0.98	0.96	1.00	1.00	0.77	0.74	0.78	1.00
0.15 to 0.3 m	0.94	0.80	1.00	1.00	0.75	0.40	0.86	1.00
0.3 to 0.6 m	N/A	N/A	N/A	N/A	N/A	N/A	N/A	N/A
Background Alarm Rates								
	P_{ba}^{res}: 0.10				**P_{ba}^{disc}:** 0.07			

[a]The two numbers to the right of the all types munitions result are an upper and lower 90 percent confidence level for an assumed binomial distribution.
[b]All depths are measured to the center of the object.

Table 2b. Blind Grid correct UXO type classification of targets correctly discriminated as munitions for the statistical approach

Size	Percentage
25mm	100%
37mm	100%
60mm	100%
81mm	13%
105mm	67%
105 artillery	20%
Overall	67%

5.2 Template-match Approach

The template match approach used data processed in the field in the first pass (no repeat or cross measurements), and compared polarizability curves of unknown objects to the polarizabilities of the objects in the database/library. Parameters used in this approach were (a) a similarity of major polarizability curves, (b) the similarity of medium and minor polarizability curves, and (d) the distance between major and medium/minor polarizabilities. In this approach from 400 flag/cell locations, 18 were labeled as "can't analyze". Fourteen of these responses had S/N between four and six, three locations with S/N less than four but with inconsistent responses, and one with a relatively high S/N but again with an inconsistent response. 181 cells with S/N less than four were considered empty, and therefore the discrimination was done on 201 flags. From those 54 were identified as scrap, and safe to leave in the ground, and 147 were identified as UXO or objects that have to be dug.

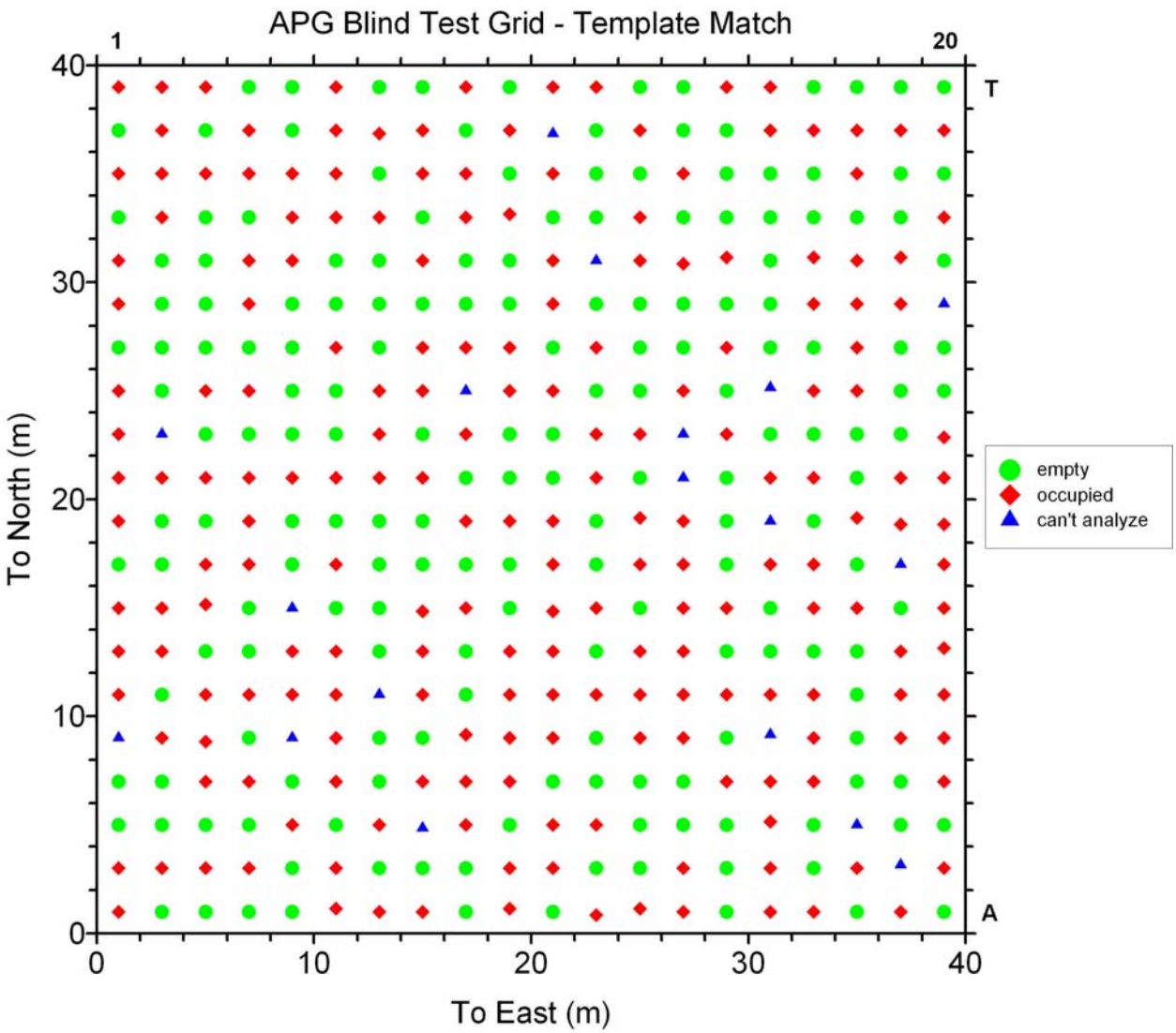

Figure 10. The APG Blind Test Grid cells identified as empty (green circle), occupied (red diamond) or "can't analyze" (blue triangle) using the template match approach.

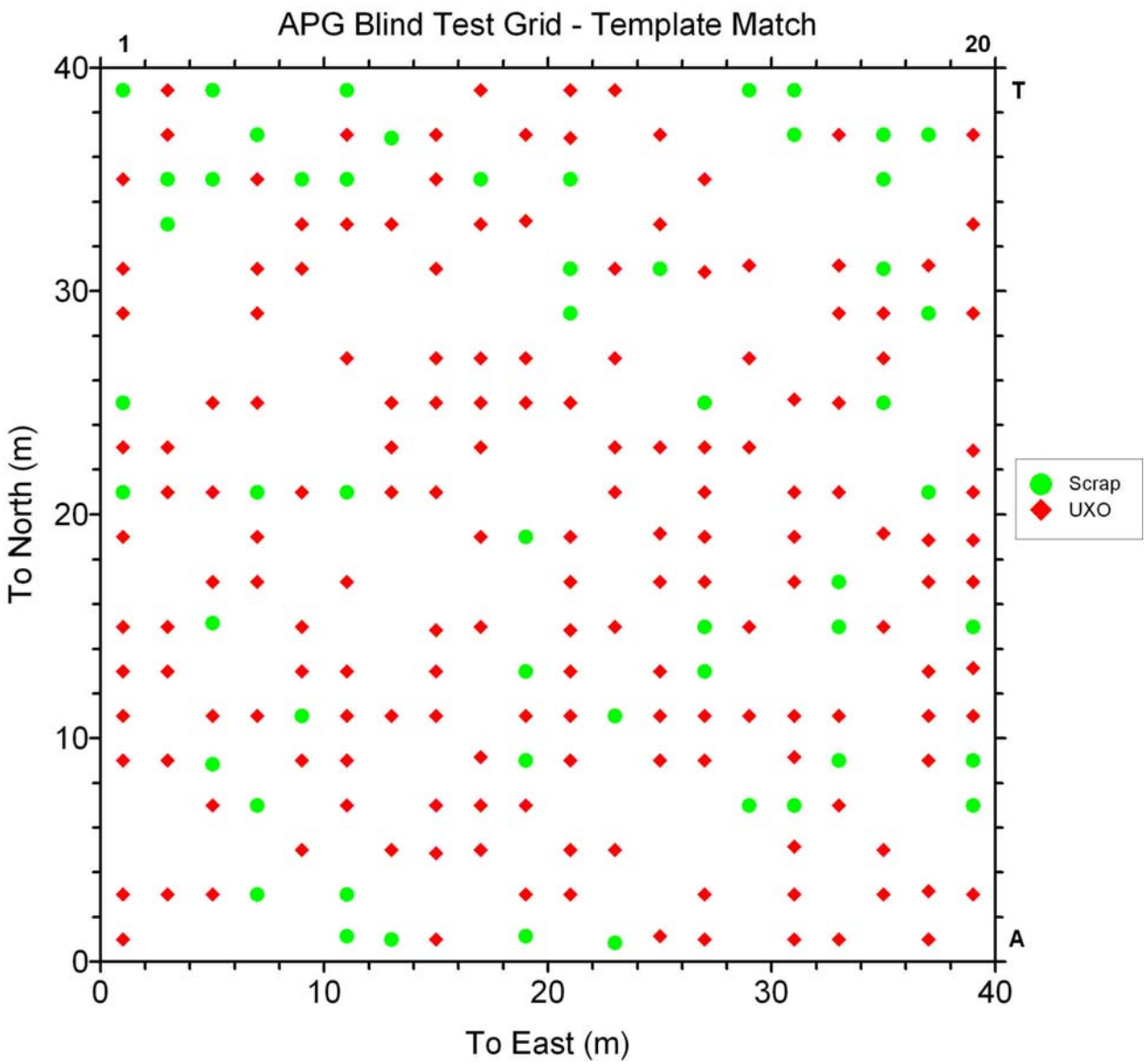

Figure 11. The APG Blind Test Grid cells identified as scrap (green circle) or UXO (red diamond) using the template match approach.

The scoring results are shown in Table 3. In this approach we correctly identified 97% and 97% of munitions in the response and discrimination stages, respectively. We were not able to detect some of 105 mm projectiles/mortars at the depth greater than eight times of the objects diameter. We correctly discriminated all detected munitions. We also correctly identified 97% of scrap in the response stage, and the probability of false positive in the discrimination stage was 0.49. The

background alarm rates for the response and discrimination stages were 0.08 and 0.05, respectively. The efficiency rate at the operating point was 1.0, with the false positive rejection rate of 0.49 and the background alarm rejection rate of 0.44. Table 3b shows the Blind Test Grid correct UXO type classification of targets correctly discriminated as munitions. Overall 72% of munitions were classified correctly. In this case, we did not separate 105 mm projectiles from 105 mm mortars.

Table 2a. Blind Grid scoring results for the template match approach

	Response Stage				**Discrimination Stage**			
Munitions[a] Scores	***P_d^{res}: by type***				***P_d^{disc}: by type***			
	All Types	**105-mm**	**81/60-mm**	**37/25-mm**	**All Types**	**105-mm**	**81/60-mm**	**37/25-mm**
	0.99	0.96	1.00	1.00	0.99	0.96	1.00	1.00
	0.97	0.90	1.00	1.00	0.97	0.90	1.00	1.00
	0.93	0.79	0.93	0.93	0.93	0.79	0.93	0.93
By Depth[b]								
0 to 4D	1.00	1.00	1.00	1.00	1.00	1.00	1.00	1.00
4D to 8D	1.00	1.00	1.00	1.00	1.00	1.00	1.00	1.00
8D to 12D	0.67	0.50	1.00	1.00	0.67	0.50	1.00	1.00
Clutter Scores	***P_{cd}***				***P_{fp}***			
By Mass								
By Depth[b]	**All Mass**	**0 to 0.25 kg**	**>0.25 to 1 kg**	**>1 to 10 kg**	**All Mass**	**0 to 0.25 kg**	**>0.25 to 1 kg**	**>1 to 10 kg**
All Depth	0.99				0.55			
	0.97	0.93	1.00	1.00	0.49	0.24	0.67	1.00
	0.93				0.43			
0 to 0.15 m	0.97	0.94	1.00	1.00	0.46	0.23	0.67	1.00
0.15 to 0.3 m	0.94	0.80	1.00	1.00	0.69	0.40	0.71	1.00
0.3 to 0.6 m	N/A	N/A	N/A	N/A	N/A	N/A	N/A	N/A
Background Alarm Rates								
	P_{ba}^{res}: 0.08				**P_{ba}^{disc}:** 0.05			

[a]The two numbers to the right of the all types munitions result are an upper and lower 90-percent confidence interval for an assumed binomial distribution.
[b]All depths are measured to the center of the object.

Table 3b. Blind Grid correct UXO type classification of targets correctly discriminated as munitions for the template match approach

Size	Percentage
25mm	93%
37mm	100%
60mm	33%
81mm	53%
105mm	77%
Overall	72%

6. CONCLUSIONS

This survey showed that the same discrimination capabilities afforded by the cart-mounted system are available in the hand-held unit, although with a slightly reduced depth of detection. If only single objects are present, taking the measurements 0.15 m before and after, and at the flag location, along the survey lines, resulted in less than 10% of locations that could not be analyzed, while correctly discriminating all munitions with the S/N above the threshold. Although only 7% of the soundings used in the discrimination were from locations different from the flag locations, having three measurements per flag helped with the data quality control, and they were essential especially when a person other than the one interpreting the data acquired the data. This is a very important finding, since it simplifies the field data acquisition and makes surveys more efficient. If flag locations were to contain multiple objects, however, multiple measurements around the flag would be required to identify them correctly.

7. ACKNOWLEDGMENTS

This work was partially supported by the U.S. Department of Energy and LBNL under Contract No. DE-AC02-05CH11231, and the U. S. Department of Defense under the Strategic Environmental Research and Development Program Project MR-1667.

8. REFERENCES

Gasperikova, E., Smith, J.T., Morrison, H.F., Becker, A., 2007, Berkeley UXO Discriminator (BUD): SAGEEP, Denver.

Gasperikova, E., J. T. Smith, H. F. Morrison, A. Becker, 2007, UXO Detection and Discrimination with Berkeley UXO Discriminator (BUD), UXO Forum, Orlando, FL

Gasperikova, E., J. T. Smith, H. F. Morrison, A. Becker, 2007, Berkeley UXO Discriminator (BUD) at Camp Sibert, AL, Partners in Environmental Technology Technical Symposium & Workshop**,** Washington D.C.

Gasperikova, E., J. T. Smith, H. F. Morrison, A. Becker, 2007, BUD Results from ESTCP Demonstration Sites, Partners in Environmental Technology Technical Symposium & Workshop**,** Washington D.C.

Gasperikova, E., J. T. Smith, H. F. Morrison, A. Becker, 2008, UXO Identification Using Berkeley UXO Discriminator (BUD), IEEE International Geoscience & Remote Sensing Symposium, Boston, MA

Gasperikova, E., Smith, J.T., Morrison, H.F., Becker, A., and Kappler, K, 2009, UXO detection and identification based on intrinsic target polarizabilities – A case history: Geophysics, **74**, No.1, B1-B8.

Gasperikova, E., Smith, J.T., Kappler, K, Morrison, H.F., and Becker, A., 2010, Hand-held UXO Discriminator: SERDP Report.

Smith, J.T., and Morrison, H.F., 2004, Estimating equivalent dipole polarizabilities for the inductive response of isolated conductive bodies: IEEE Trans. Geosci. Remote Sensing, **42**, p. 1208-1214.

Smith, J.T., Morrison, H.F., and Becker, A., 2004, Resolution depths for some transmitter-receiver configurations: IEEE Trans. Geosci. Remote Sensing, **42**, p. 1215-1221.

Smith, J.T., Morrison, H.F., and Becker, A., 2005, Optimizing receiver configurations for resolution of equivalent dipole polarizabilities in situ: IEEE Trans. Geosci. Remote Sensing, **43**, p. 1490 - 1498.

Smith, J.T., Morrison, H.F., Doolittle, L.R., and Tseng, H-W., 2007, Multi-transmitter null coupled systems for inductive detection and characterization of metallic objects: Journal of Applied Geophysics, **61**, p. 227–234

9. ACRONYMS

APG	Aberdeen Proving Ground
BUD	Berkeley UXO Discriminator
ESTCP	Environmental Security Technology Certification Program
FPGA	Field Programmable Gate Array
LBNL	Lawrence Berkeley National Laboratory
RFS	Richmond Field Station
SERDP	Strategic Environmental Research and Development Program
S/N	Signal-to-noise
UXO	Unexploded Ordnance
YPG	Yuma Proving Ground

TABLE 1. The Calibration Grid discrimnation results

Cell	p(UXO)	obj_depth(m)	LBL_ID	Army_ID	true_depth(m)	file_name
A1	0.997886	0.7155	105mmHEAT	155mmP	0.7	CAL_x1.85_y2_Run_0120.bin_diff.avg.inv
B1	0.999979	0.3241	57mm	57mmP	0.32	CAL_x6_y2_Run_0127.bin_diff.avg.inv
C1	0.999611	0.1559	BLU	BLU-26	0.12	CAL_x10.15_y2_Run_0132.bin_diff.avg.inv
D1	0.871131	0.2464	105mmHEAT	Clutter-Frag	0.14	CAL_x14_y2_Run_0136.bin_diff.avg.inv
E1	0.999997	0.1758	105mmIF	105mm(IF)	0.05	CAL_x18_y2_Run_0140.bin_diff.avg.inv
F1	0.99933	0.2123	25mm	25mm(DF)	0.2	CAL_x22_y2_Run_0144.bin_diff.avg.inv
G1	0.999995	0.289	37mm	37mm(DF)	0.17	CAL_x25.85_y2_Run_0147.bin_diff.avg.inv
H1	0.999999	0.3767	2.75"	60mm(IF)	0.34	CAL_x30.15_y2_Run_0153.bin_diff.avg.inv
I1	1	0.4788	2.75"	81mm(IF)	0.43	CAL_x34.15_y2_Run_0157.bin_diff.avg.inv
J1	0.999899	0.4838	57mm	105mm(DF)	0.58	CAL_x38_y2_Run_0160.bin_diff.avg.inv
K1	0.999805	0.5494	57mm	105mm(IF)	0.55	CAL_x41.85_y2_Run_0163.bin_diff.avg.inv
A2	0.999998	0.256	2.75"	2.75Rocket	0.18	CAL_x1.85_y6_Run_0005.bin_diff.avg.inv
B2	0.999977	0.3574	20mm	20mmP	0.23	CAL_x6_y6.multi.list.2dip.inv.2
C2	0.999855	0.199	BLU	BLU-26	0.14	CAL_x9.85_y6_Run_0013.bin_diff.avg.inv
D2	0.154639	0.1602	105mmHEAT	Clutter-Frag	0.02	CAL_x14_y6_Run_0018.bin_diff.avg.inv
E2	0.999968	0.1695	81mm	81mm(IF)	0.11	CAL_x18_y6_Run_0022.bin_diff.avg.inv
F2	0.999977	0.259	25mm	25mm(DF)	0.19	CAL_x22.15_y6_Run_0027.bin_diff.avg.inv
G2	0.999998	0.2546	37mm	37mm(DF)	0.24	CAL_x26_y6_Run_0030.bin_diff.avg.inv
H2	0.999999	0.2684	60mm	60mm(IF)	0.33	CAL_x30_y6_Run_0034.bin_diff.avg.inv
I2	0.995702	0.5801	60mm	81mm(IF)	0.49	CAL_x33.85_y6_Run_0037.bin_diff.avg.inv
J2	0.9991	0.5584	57mm	105mm(DF)	0.75	CAL_x38.15_y6_Run_0395.bin_diff.avg.inv
K2	0.971501	0.7871	57mm	105mm(IF)	0.69	CAL_x42_y6.multi.list.2dip.inv.2
A3	0.999997	0.112	37mm	40mmP	0	CAL_x1.85_y10_Run_0081.bin_diff.avg.inv
B3	0.999999	0.3676	BDU	BDU-28	0.23	CAL_x6_y10.multi.list.2dip.lim2.inv.2
C3	2.00E-06	0.0482	25mm	Clutter-Frag	0.11	CAL_x10_y10_Run_0090.bin_diff.avg.inv
D3	1.00E-06	0.1937	M42	Clutter-Frag	0.15	CAL_x14_y10_Run_0094.bin_diff.avg.inv
E3	0.999999	0.1281	37mm	37mm(DF)	0.09	CAL_x18.85_y10_Run_0100.bin_diff.avg.inv
F3	0.983962	0.3257	25mm	25mm(DF)	0.3	CAL_x22_y10_Run_0103.bin_diff.avg.inv
G3	0.998628	0.5194	37mm	37mm(DF)	0.34	CAL_x26_y10.multi.list.2dip.lim.inv.2
H3	0.997232	0.5039	60mm	60mm(IF)	0.55	CAL_x30_y10_Run_0112.bin_diff.avg.inv
I3	0.999965	0.5361	60mm	81mm(IF)	0.6	CAL_x34_y10_Run_0116.bin_diff.avg.inv
J3	0.664619	0.4319	57mm	105mm(DF)	0.88	CAL_x38_y10.multi.list.2dip.inv.2
K3	0.999999	0.5447	105mmIF	105mm(IF)	0.5	CAL_x42_y10_Run_0124.bin_diff.avg.inv
A4	0.999997	0.1665	37mm	40mmP	0.11	CAL_x2.15_y14_Run_0158.bin_diff.avg.inv
B4	1	0.1756	BDU	BDU-28	0.17	CAL_x6_y14_Run_0161.bin_diff.avg.inv
C4	0	0.1845	25mm	Clutter-Frag	0.2	CAL_x10_y14_Run_0165.bin_diff.avg.inv
D4	1.00E-06	0.2246	25mm	Clutter-Frag	0.12	CAL_x14_y14_Run_0169.bin_diff.avg.inv
E4	0.980758	0.0651	25mm	25mm(DF)	0.04	CAL_x18_y14_Run_0172.bin_diff.avg.inv
F4	0.999549	0.3496	25mm	25mm(DF)	0.3	CAL_x21.85_y14_Run_0178.bin_diff.avg.inv
G4	0.999988	0.3396	37mm	37mm(DF)	0.39	CAL_x26.15_y14_Run_0407.bin_diff.avg.inv
H4	9999	0.3666	57mm	60mm(IF)	0.6	CAL_x30.15_y14_Run_0188.bin_diff.avg.inv
I4	0.999975	0.6603	105mmIF	81mm(IF)	0.62	CAL_x34.15_y14_Run_0192.bin_diff.avg.inv
J4	0.999685	0.5795	105mmIF	105mm(DF)	0.61	CAL_x37.85_y14_Run_0194.bin_diff.avg.inv
K4	9999	0.1079	25mm	105mm(IF)	1.05	CAL_x42.15_y14_Run_0441.bin_diff.avg.inv
A5	0.999655	0.3825	2.75"	2.75Rocket	0.34	CAL_x2_y18_Run_0233.bin_diff.avg.inv
B5	0.999996	0.2372	20mm	20mmP	0.19	CAL_x6_y18_Run_0237.bin_diff.avg.inv
C5	0.999939	0.1913	M42	M42	0.21	CAL_x10_y18_Run_0241.bin_diff.avg.inv
D5	0.710493	0.1791	60mm	Clutter-Frag	0.08	CAL_x14_y18_Run_0245.bin_diff.avg.inv
E5	0.999999	0.3152	60mm	60mm(IF)	0.05	CAL_x18.15_y18_Run_0253.bin_diff.avg.elev20.inv
F5	0.99954	0.2405	25mm	25mm(DF)	0.26	CAL_x22_y18_Run_0256.bin_diff.avg.elev20.inv
G5	0.999999	0.2924	37mm	37mm(DF)	0.3	CAL_x26.15_y18_Run_0261.bin_diff.avg.elev20.inv
H5	0.999993	0.2915	60mm	60mm(IF)	0.28	CAL_x30.15_y18_Run_0266.bin_diff.avg.inv
I5	0.999999	0.4523	60mm	81mm(IF)	0.53	CAL_x34.15_y18_Run_0270.bin_diff.avg.inv
J5	0.999816	0.5495	105mmIF	105mm(DF)	0.56	CAL_x38_y18_Run_0273.bin_diff.avg.inv
K5	1	0.5387	105mmIF	105mm(IF)	0.48	CAL_x42.15_y18_Run_0278.bin_diff.avg.inv
A6	9999	0.078	57mm	155mmP	1.08	CAL_x1.7_y22_Run_0422.bin_diff.avg.inv
B6	0.999987	0.2824	57mm	57mmP	0.32	CAL_x6.15_y22_Run_0318.bin_diff.avg.inv
C6	0.999802	0.2824	M42	M42	0.23	CAL_x10_y22_Run_0321.bin_diff.avg.inv
D6	0.999905	0.1737	105mmIF	Clutter-Frag	0.04	CAL_x14.15_y22_Run_0326.bin_diff.avg.inv
E6	1	0.1666	105mmHEAT	105mm(DF)	0.04	CAL_x17.85_y22_Run_0328.bin_diff.avg.inv
F6	0.989512	0.3119	25mm	25mm(DF)	0.26	CAL_x22_y22_Run_0333.bin_diff.avg.inv
G6	0.999999	0.2241	37mm	37mm(DF)	0.18	CAL_x26_y22_Run_0338.bin_diff.avg.inv
H6	0.999999	0.3981	60mm	60mm(IF)	0.34	CAL_x30_y22_Run_0342.bin_diff.avg.inv
I6	0.999999	0.379	2.75"	81mm(IF)	0.35	CAL_x34_y22_Run_0346.bin_diff.avg.inv
J6	0.999998	0.5612	105mmIF	105mm(DF)	0.47	CAL_x37.85_y22_Run_0349.bin_diff.avg.inv
K6	0.999999	0.3542	105mmIF	105mm(IF)	0.32	CAL_x42.15_y22_Run_0356.bin_diff.avg.inv

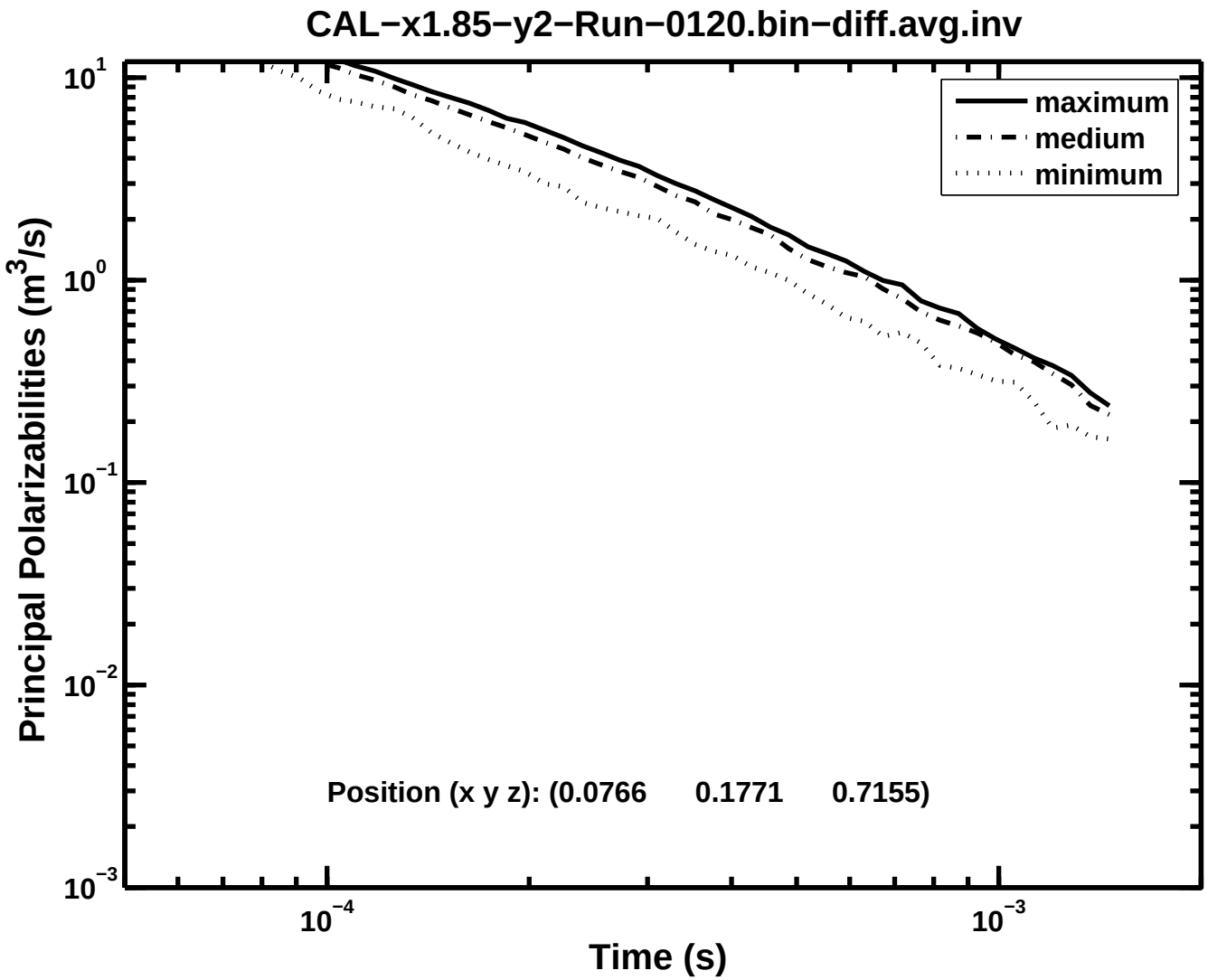
CAL−x1.85−y2−Run−0120.bin−diff.avg.inv
maximum
medium
minimum
Principal Polarizabilities (m3/s)
10^1
10^0
10^−1
10^−2
10^−3
Position (x y z): (0.0766 0.1771 0.7155)
10^−4
10^−3
Time (s)

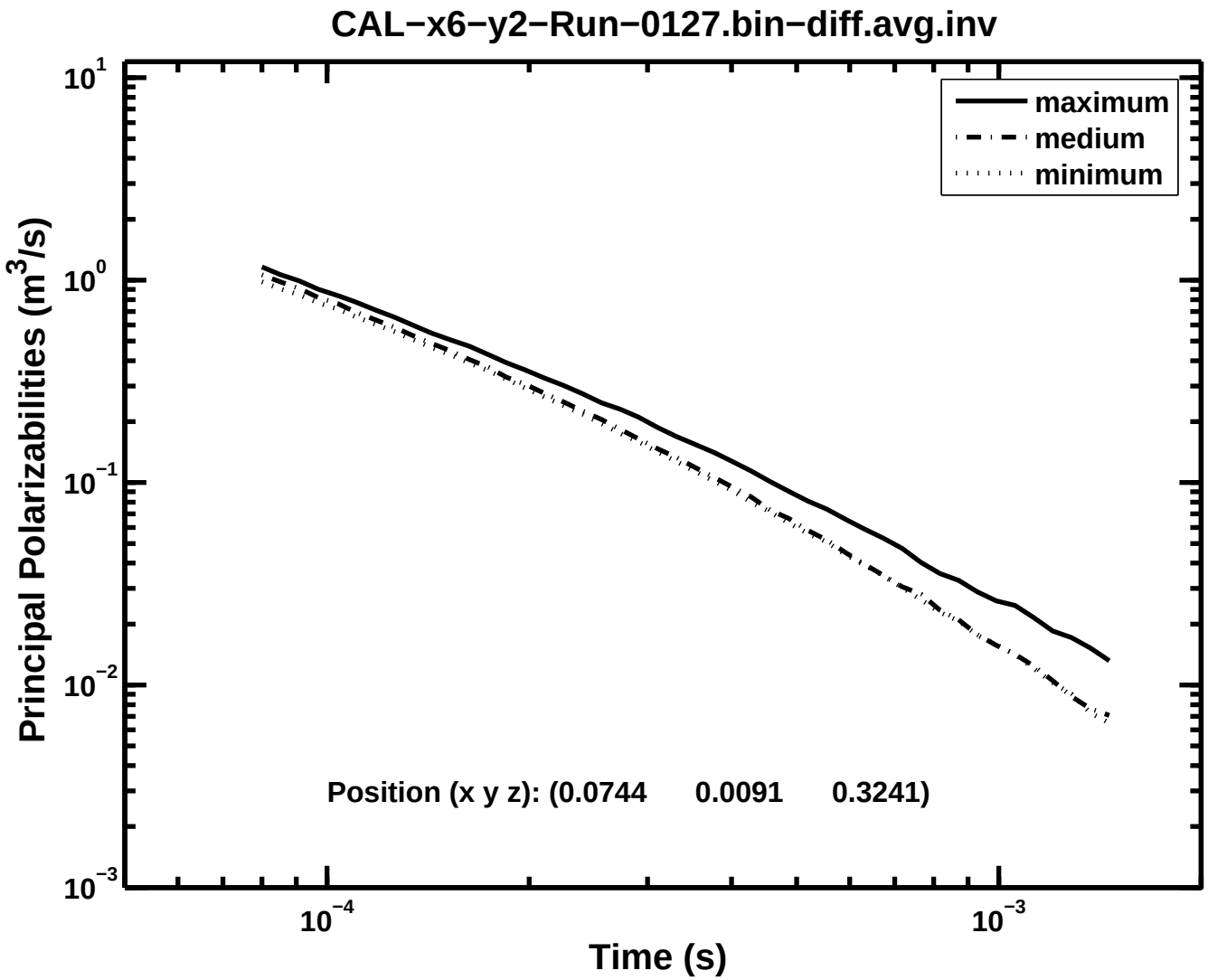
CAL−x6−y2−Run−0127.bin−diff.avg.inv
maximum
medium
minimum
Principal Polarizabilities (m3/s)
10^1
10^0
10^−1
10^−2
10^−3
Position (x y z): (0.0744 0.0091 0.3241)
10^−4
10^−3
Time (s)

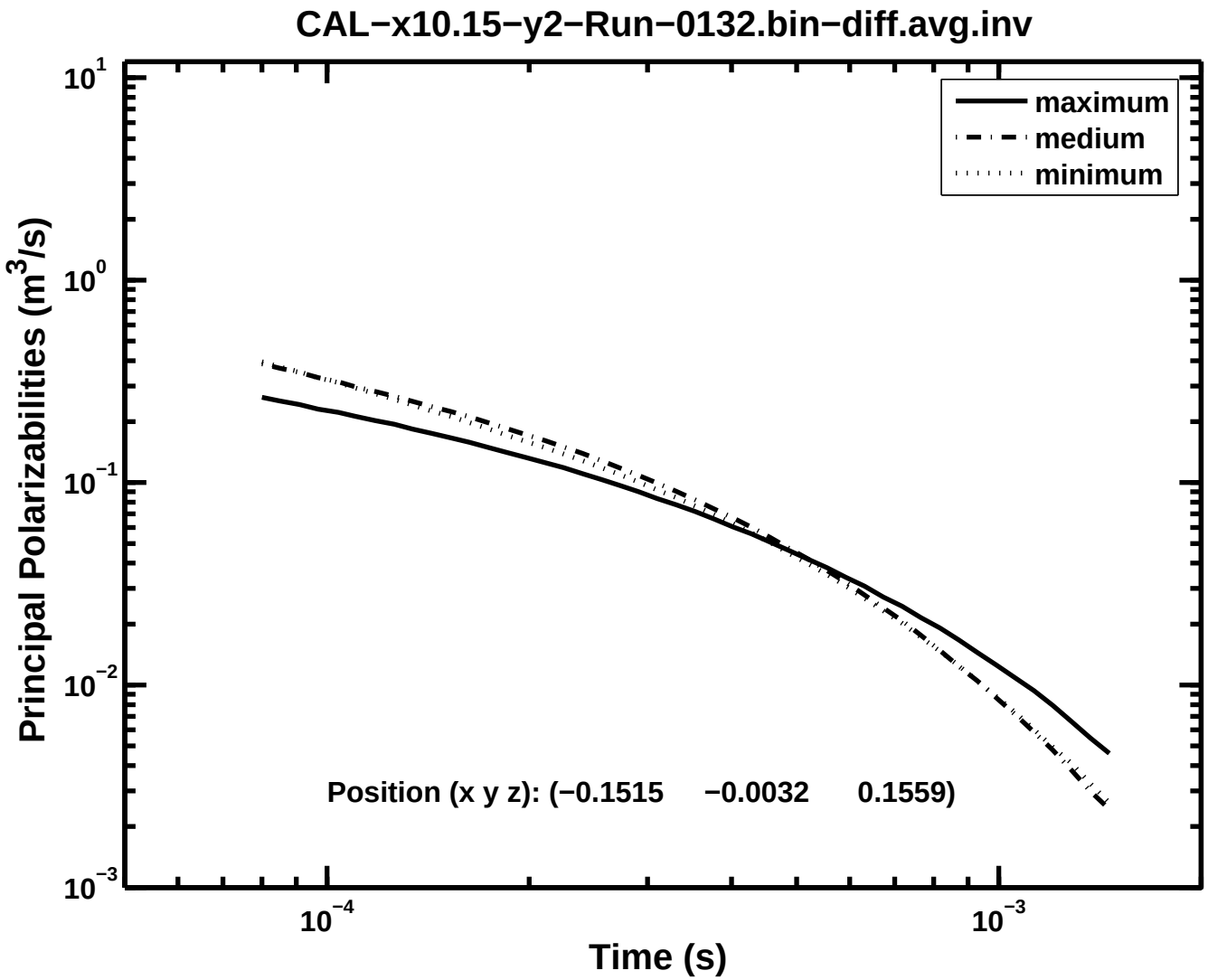
CAL−x10.15−y2−Run−0132.bin−diff.avg.inv
maximum
medium
minimum
Principal Polarizabilities (m3/s)
10^1
10^0
10^−1
10^−2
10^−3
Position (x y z): (−0.1515 −0.0032 0.1559)
10^−4
10^−3
Time (s)

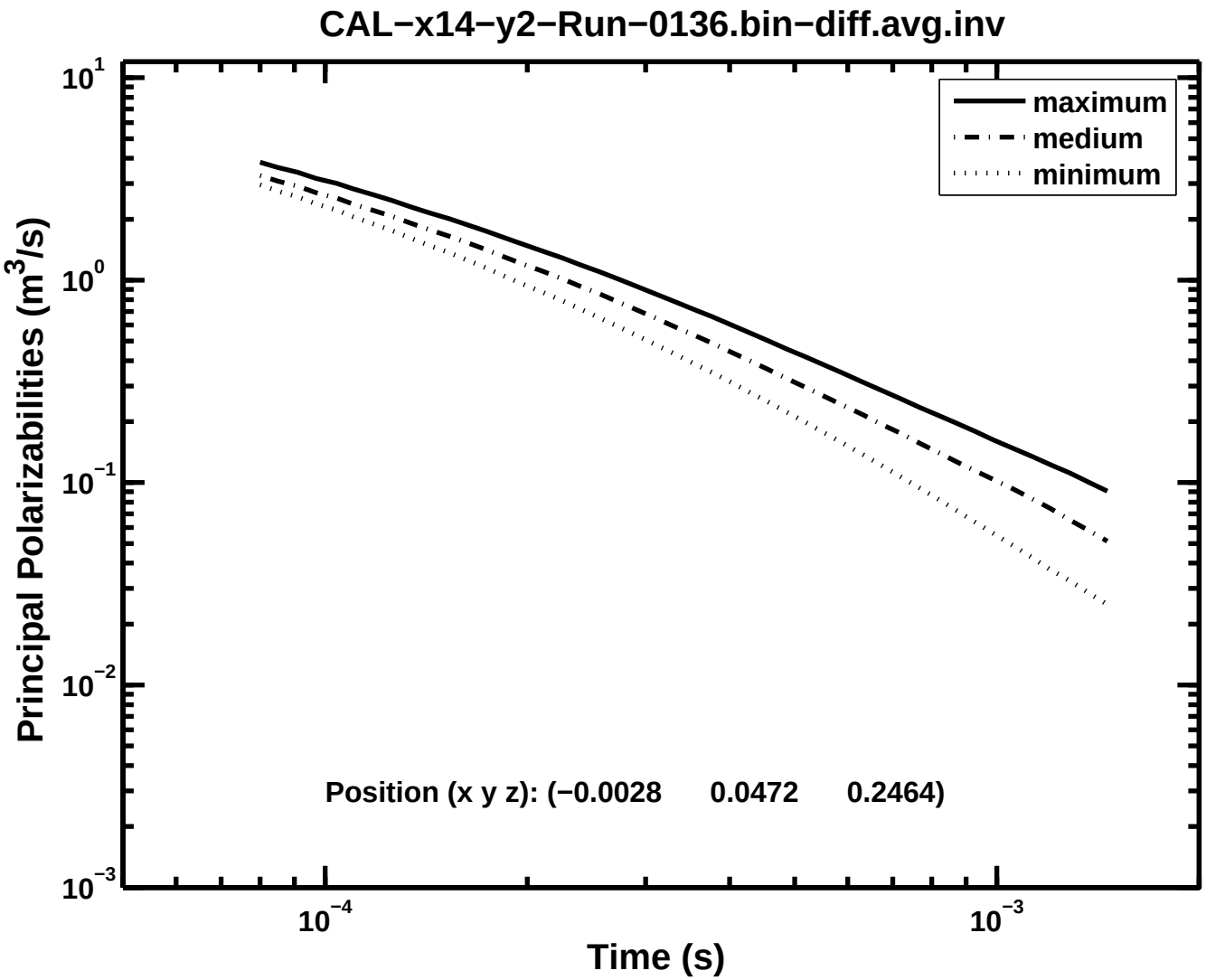
CAL−x14−y2−Run−0136.bin−diff.avg.inv
maximum
medium
minimum
Position (x y z): (−0.0028 0.0472 0.2464)
Principal Polarizabilities (m3/s)
Time (s)
10^1
10^0
10^−1
10^−2
10^−3
10^−4
10^−3

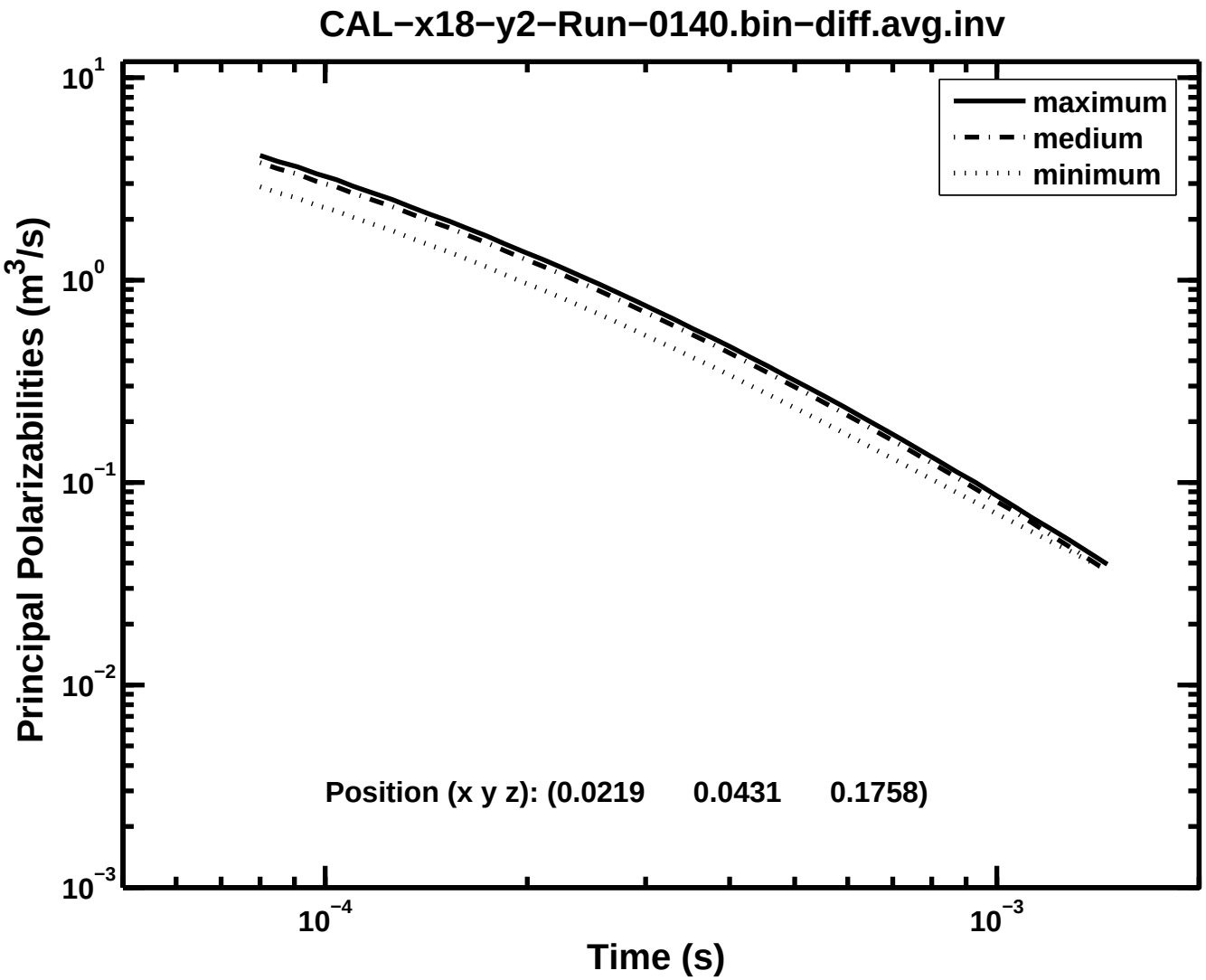
CAL−x18−y2−Run−0140.bin−diff.avg.inv
maximum
medium
minimum
Principal Polarizabilities (m3/s)
10^1
10^0
10^−1
10^−2
10^−3
Position (x y z): (0.0219 0.0431 0.1758)
10^−4
10^−3
Time (s)

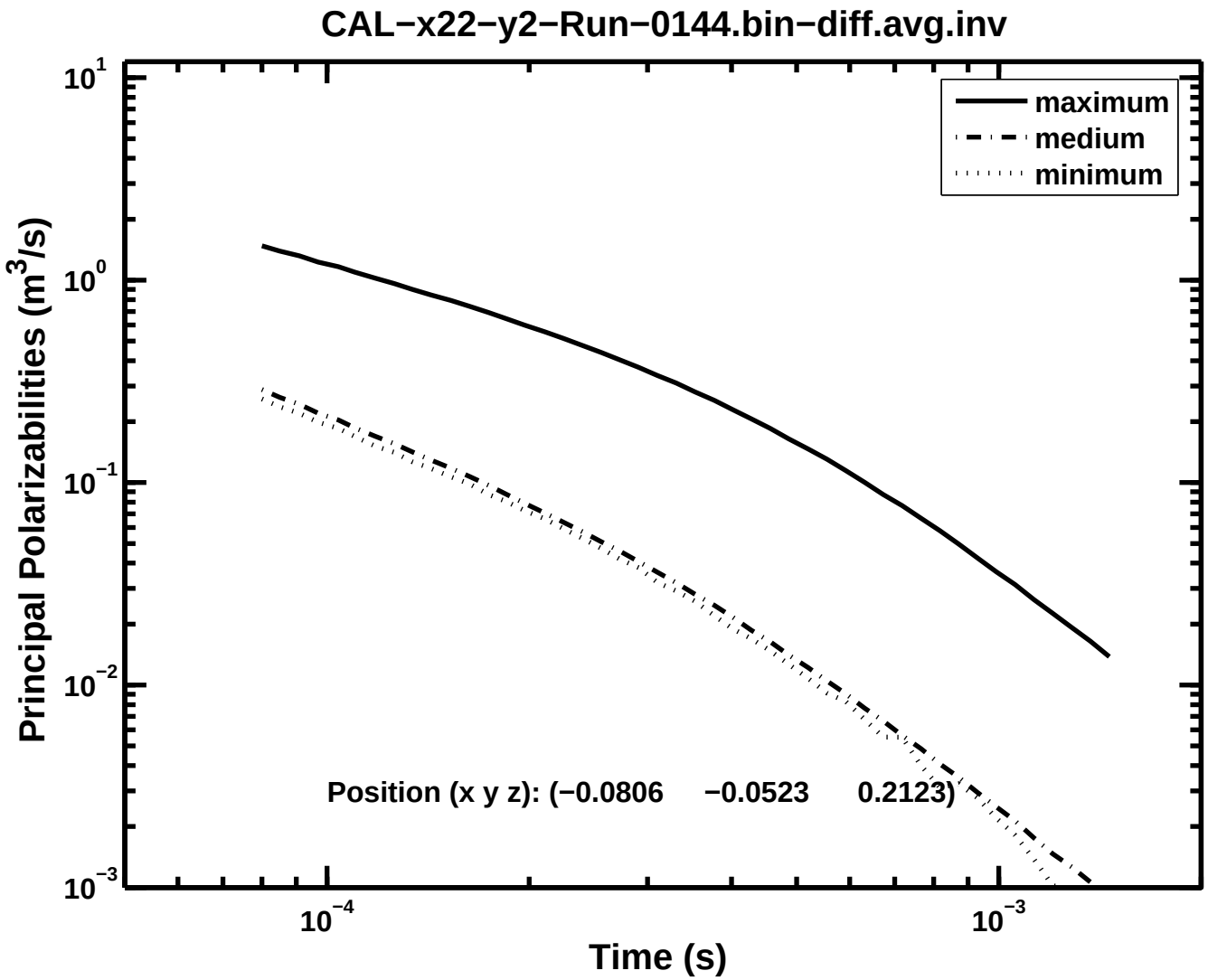
CAL−x22−y2−Run−0144.bin−diff.avg.inv
maximum
medium
minimum
Principal Polarizabilities (m3/s)
10^1
10^0
10^−1
10^−2
10^−3
Position (x y z): (−0.0806 −0.0523 0.2123)
10^−4
10^−3
Time (s)

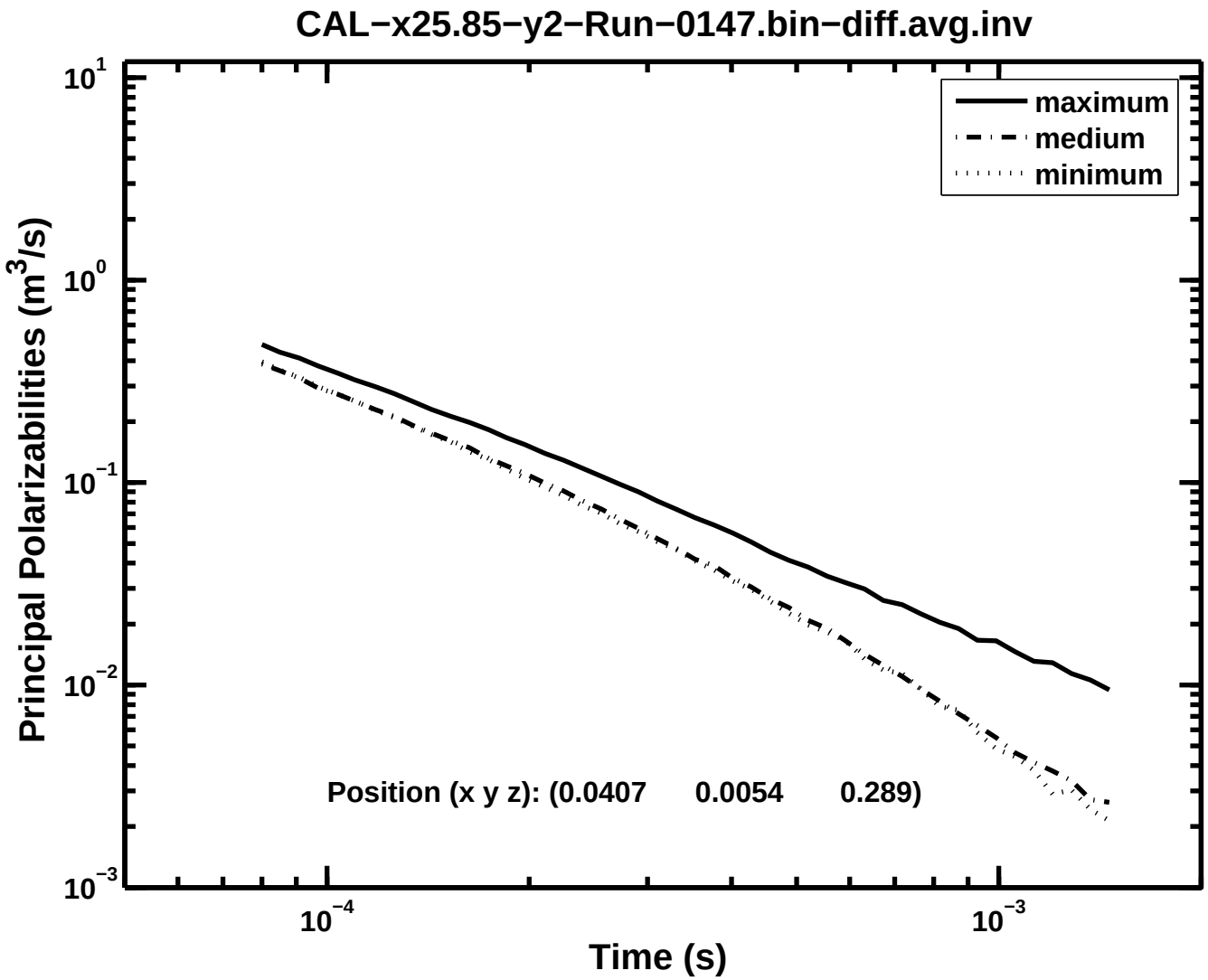
CAL−x25.85−y2−Run−0147.bin−diff.avg.inv
maximum
medium
minimum
Principal Polarizabilities (m3/s)
10^1
10^0
10^−1
10^−2
10^−3
Position (x y z): (0.0407 0.0054 0.289)
10^−4
10^−3
Time (s)

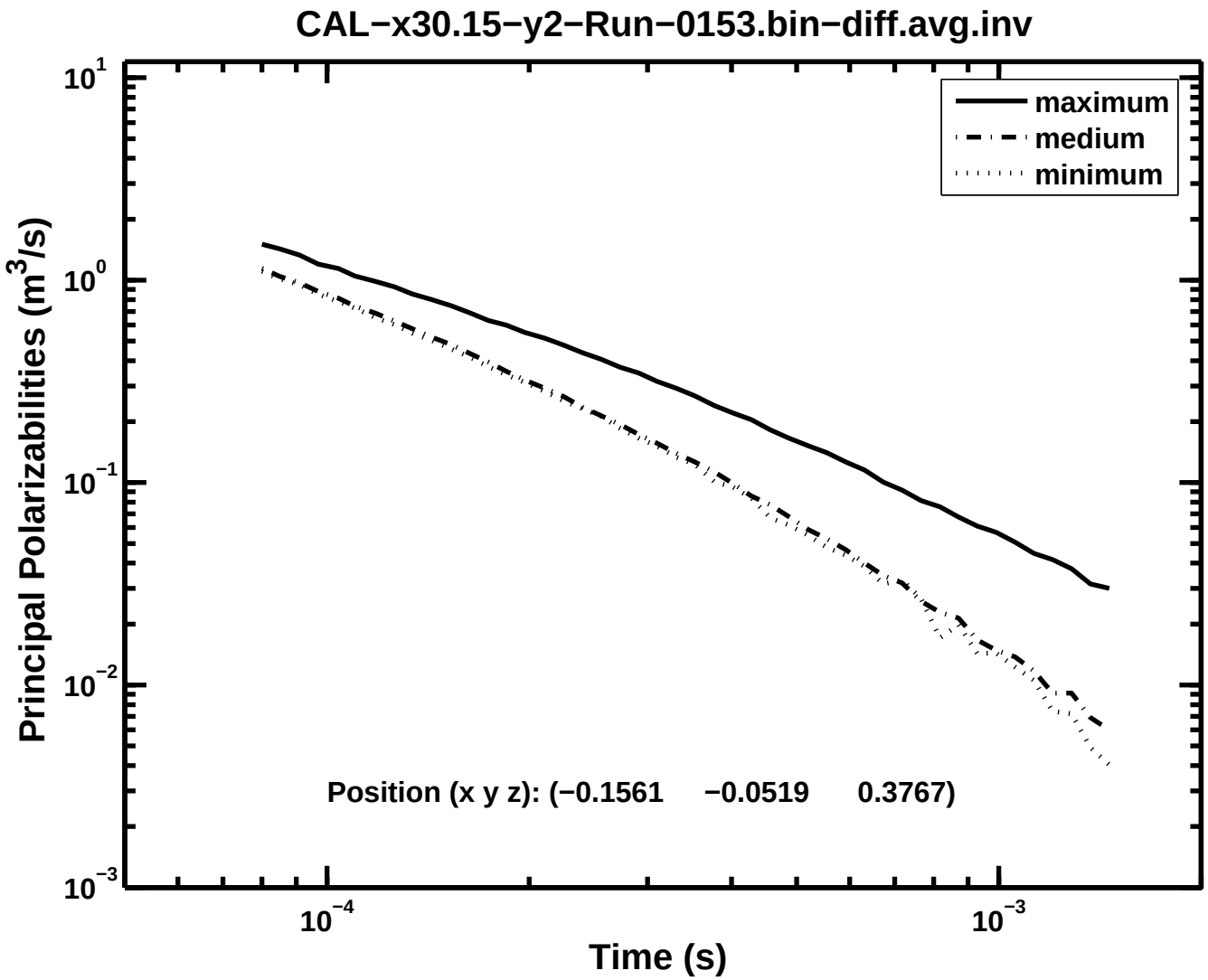
CAL−x30.15−y2−Run−0153.bin−diff.avg.inv
maximum
medium
minimum
Principal Polarizabilities (m3/s)
10^1
10^0
10^−1
10^−2
10^−3
Position (x y z): (−0.1561 −0.0519 0.3767)
10^−4
10^−3
Time (s)

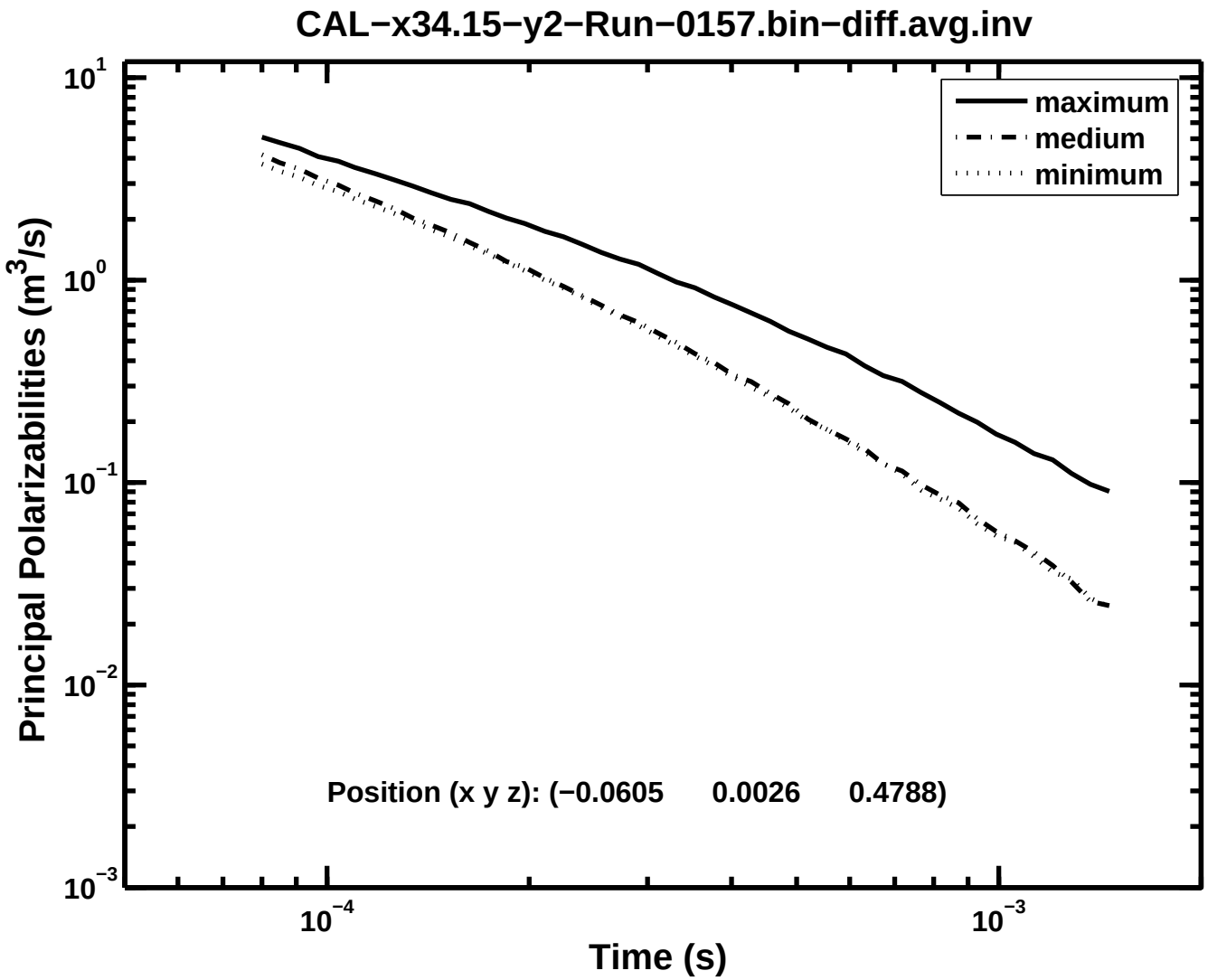
CAL−x34.15−y2−Run−0157.bin−diff.avg.inv
maximum
medium
minimum
Principal Polarizabilities (m3/s)
10^1
10^0
10^−1
10^−2
10^−3
Position (x y z): (−0.0605 0.0026 0.4788)
10^−4
10^−3
Time (s)

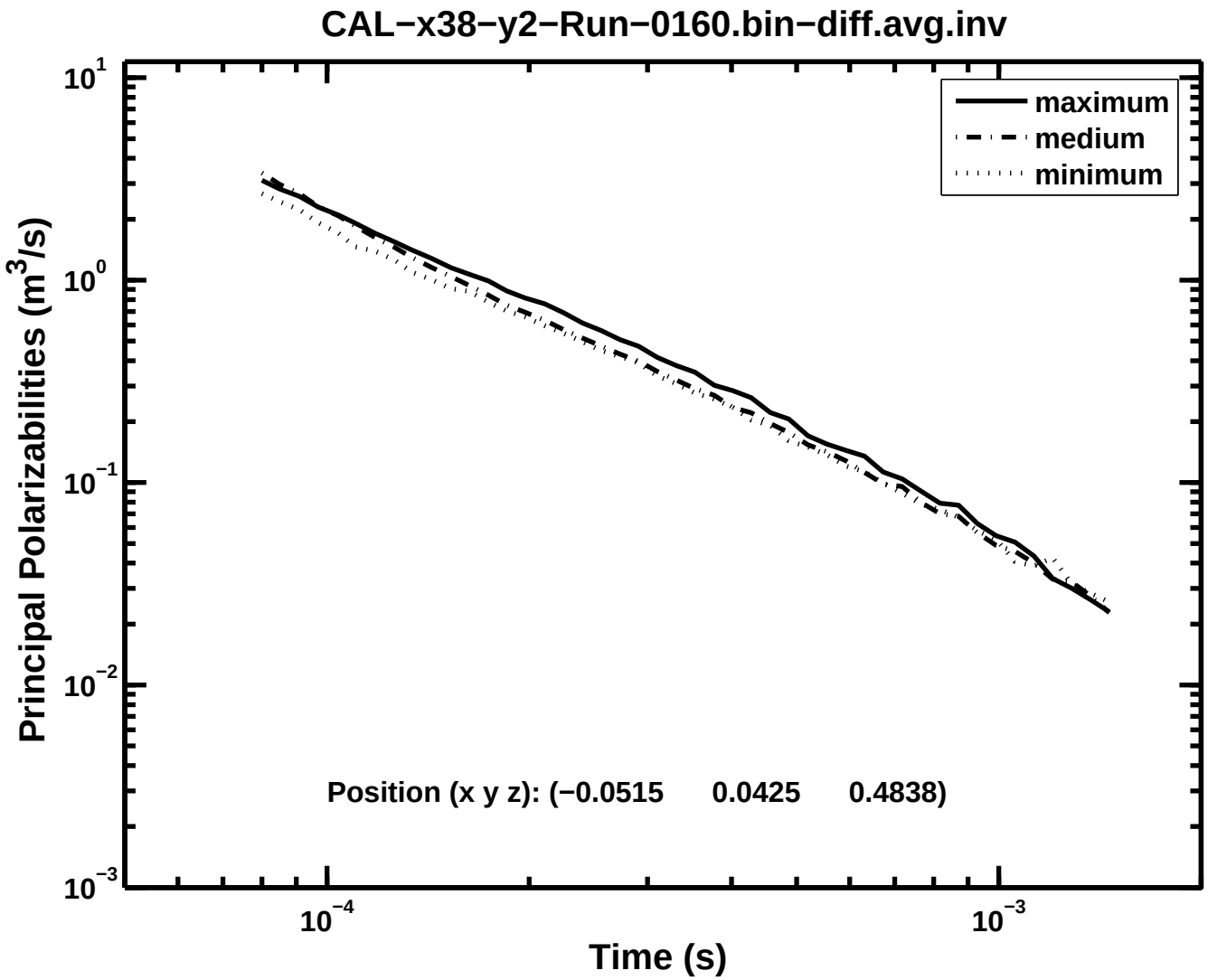
CAL−x38−y2−Run−0160.bin−diff.avg.inv
maximum
medium
minimum
Principal Polarizabilities (m3/s)
10^1
10^0
10^−1
10^−2
10^−3
Position (x y z): (−0.0515 0.0425 0.4838)
10^−4
10^−3
Time (s)

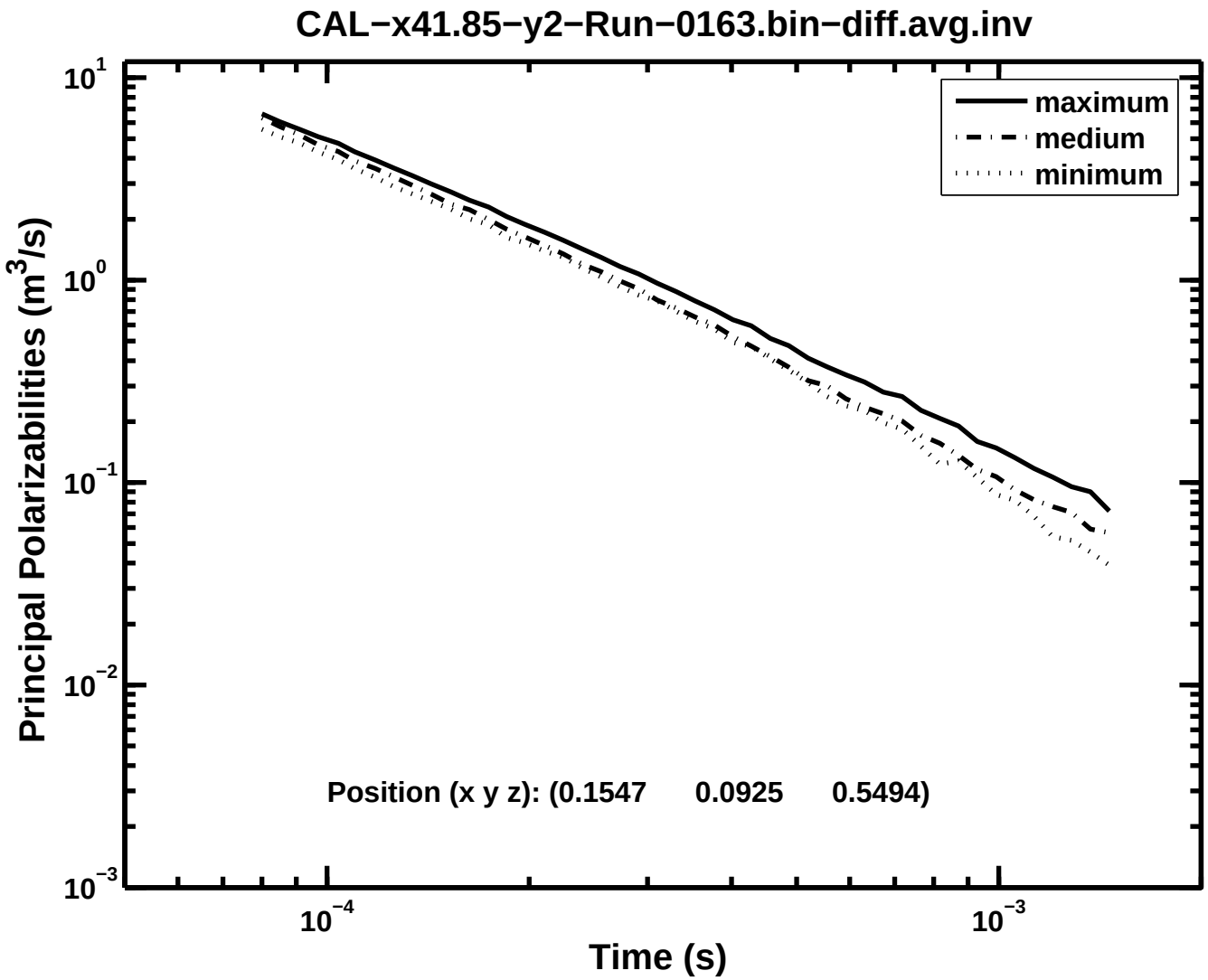
CAL−x41.85−y2−Run−0163.bin−diff.avg.inv
maximum
medium
minimum
Position (x y z): (0.1547 0.0925 0.5494)
Principal Polarizabilities (m3/s)
Time (s)
10^1
10^0
10^−1
10^−2
10^−3
10^−4
10^−3

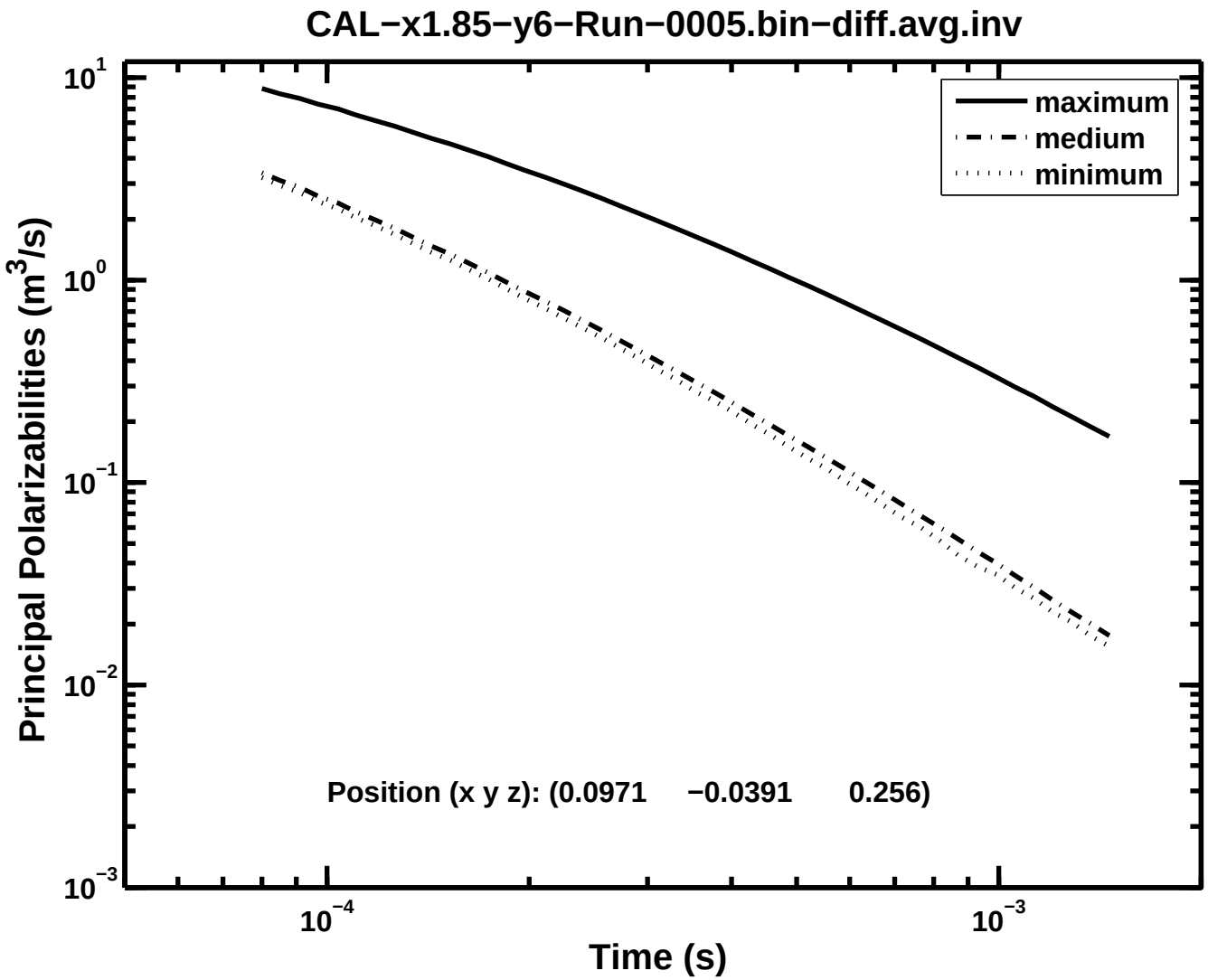
CAL−x1.85−y6−Run−0005.bin−diff.avg.inv
maximum
medium
minimum
Principal Polarizabilities (m3/s)
10^1
10^0
10^−1
10^−2
10^−3
Position (x y z): (0.0971 −0.0391 0.256)
10^−4
10^−3
Time (s)

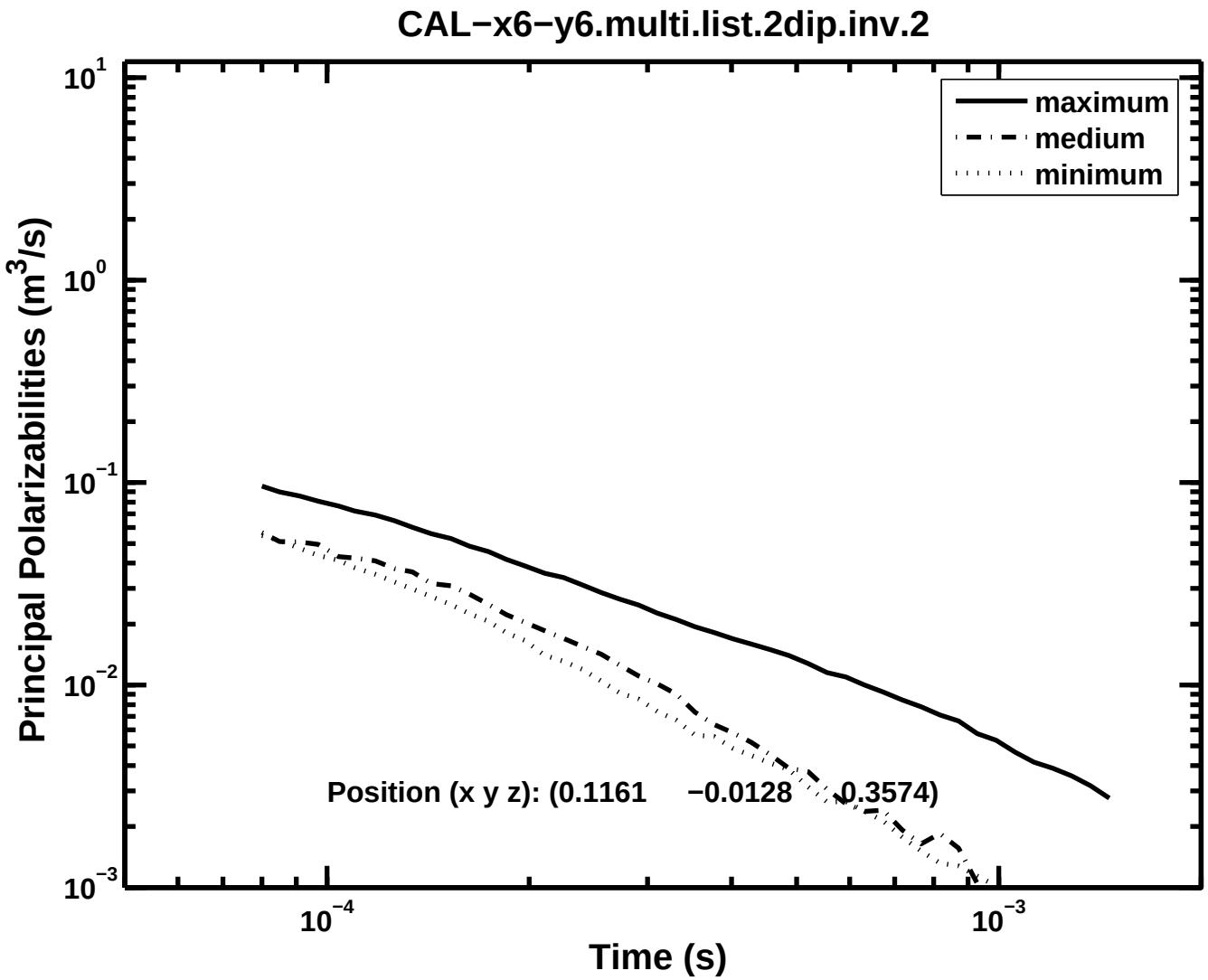
CAL−x6−y6.multi.list.2dip.inv.2
maximum
medium
minimum
Principal Polarizabilities (m3/s)
10^1
10^0
10^−1
10^−2
10^−3
Position (x y z): (0.1161 −0.0128 0.3574)
10^−4
10^−3
Time (s)

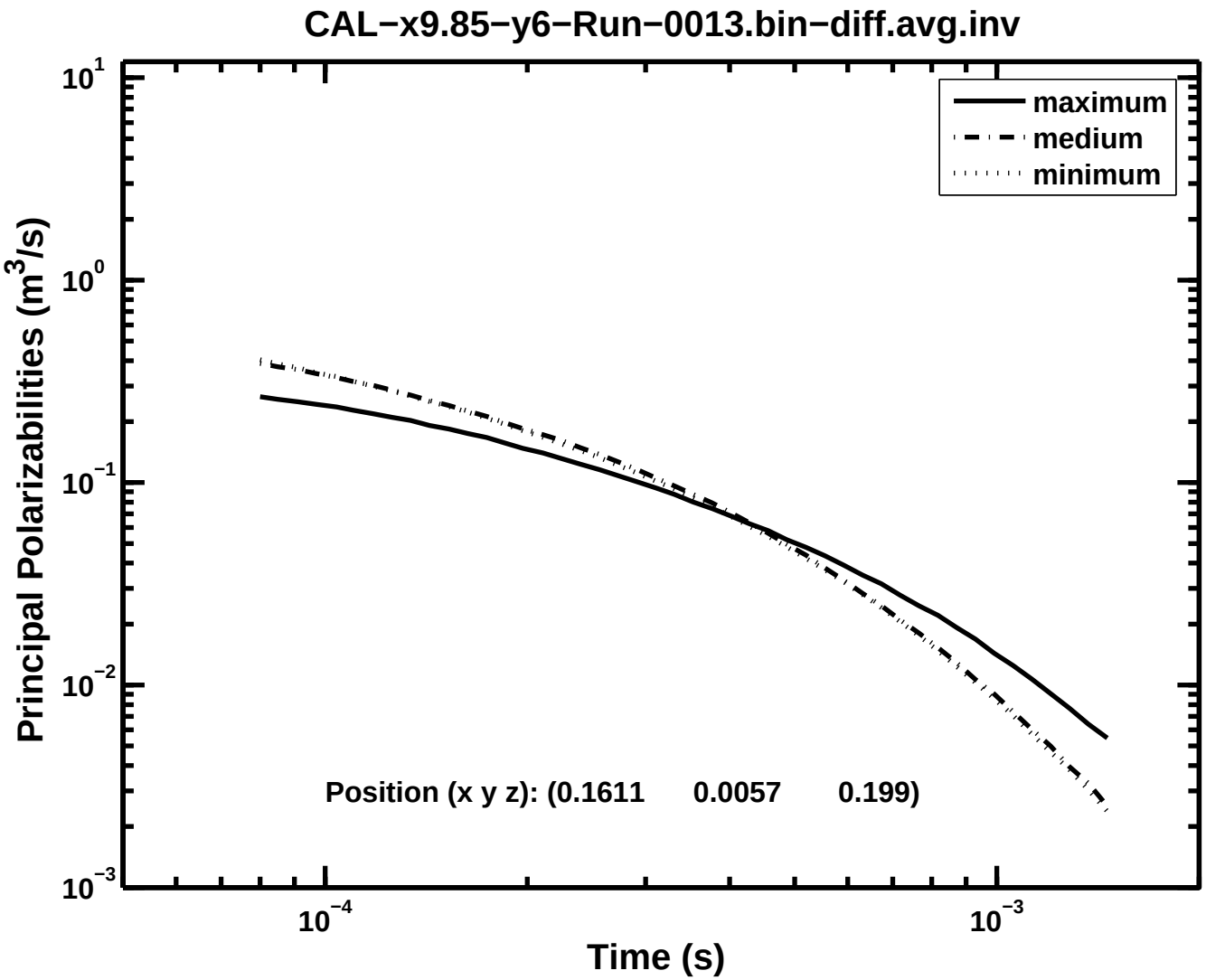
CAL−x9.85−y6−Run−0013.bin−diff.avg.inv
maximum
medium
minimum
Principal Polarizabilities (m3/s)
10^1
10^0
10^−1
10^−2
10^−3
Position (x y z): (0.1611 0.0057 0.199)
10^−4
10^−3
Time (s)

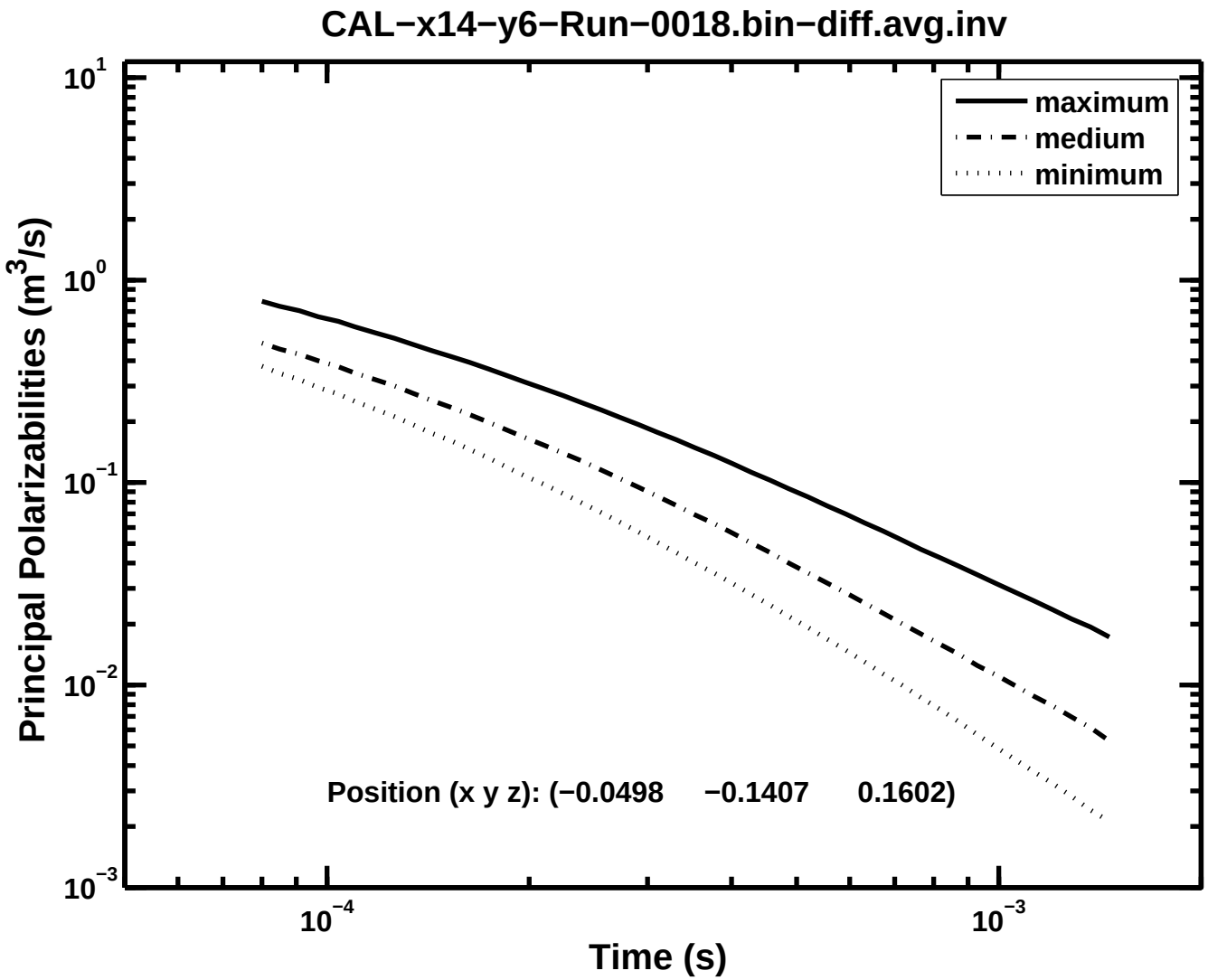
CAL−x14−y6−Run−0018.bin−diff.avg.inv
maximum
medium
minimum
Principal Polarizabilities (m3/s)
10^1
10^0
10^−1
10^−2
10^−3
Position (x y z): (−0.0498 −0.1407 0.1602)
10^−4
10^−3
Time (s)

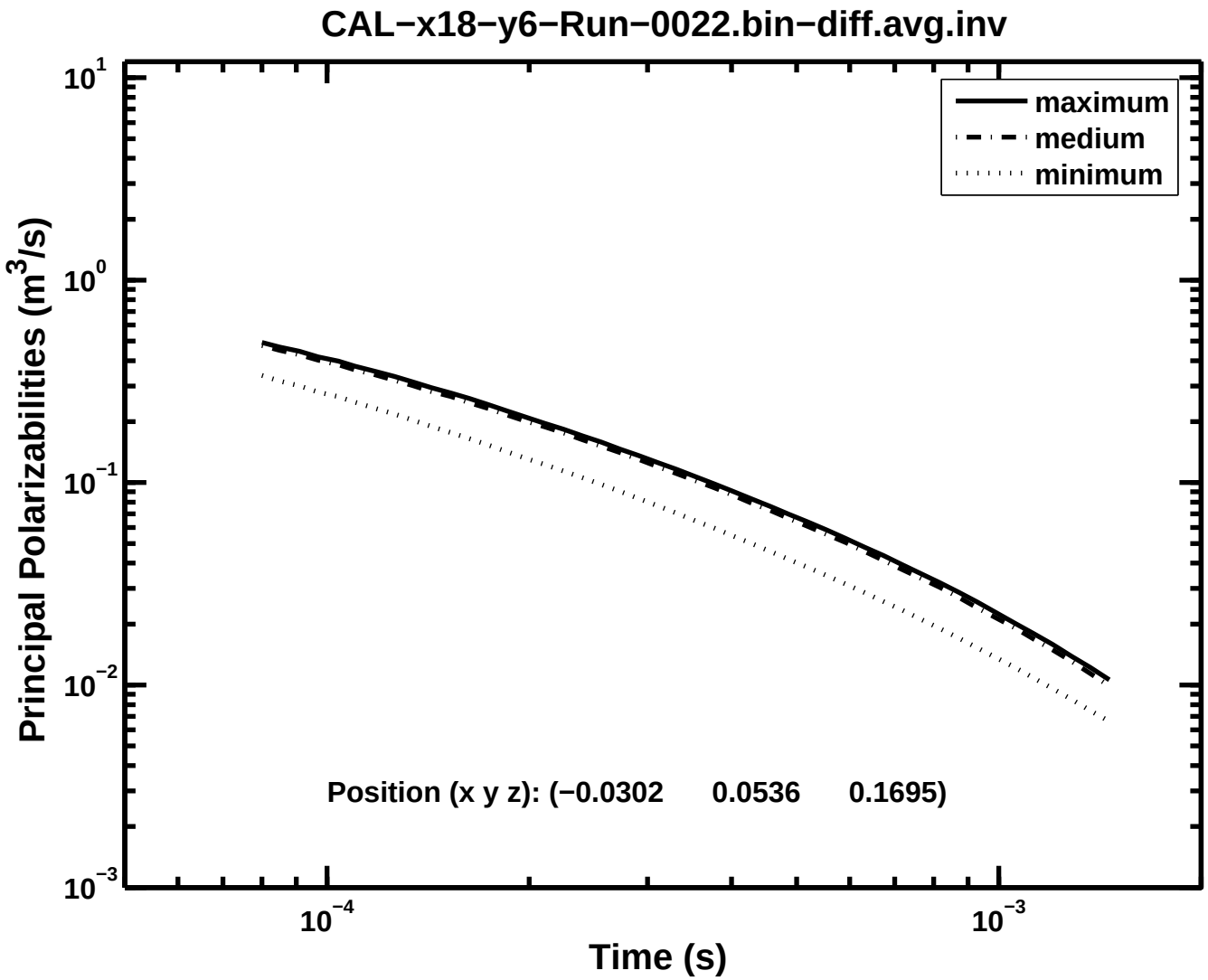
CAL−x18−y6−Run−0022.bin−diff.avg.inv
maximum
medium
minimum
Principal Polarizabilities (m3/s)
10^1
10^0
10^−1
10^−2
10^−3
Position (x y z): (−0.0302 0.0536 0.1695)
10^−4
10^−3
Time (s)

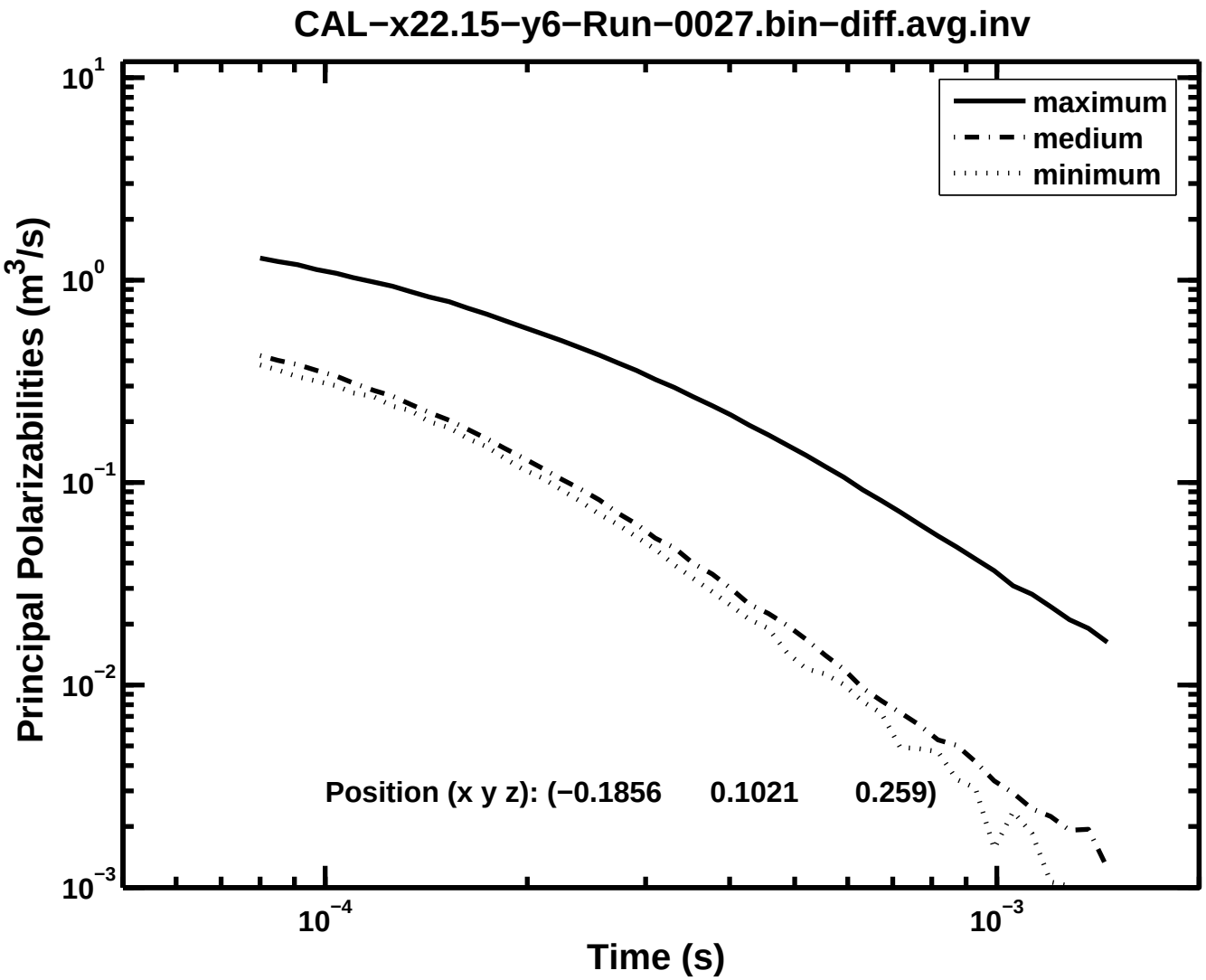
CAL−x22.15−y6−Run−0027.bin−diff.avg.inv
maximum
medium
minimum
Position (x y z): (−0.1856 0.1021 0.259)
Principal Polarizabilities (m3/s)
Time (s)
10^1
10^0
10^−1
10^−2
10^−3
10^−4
10^−3

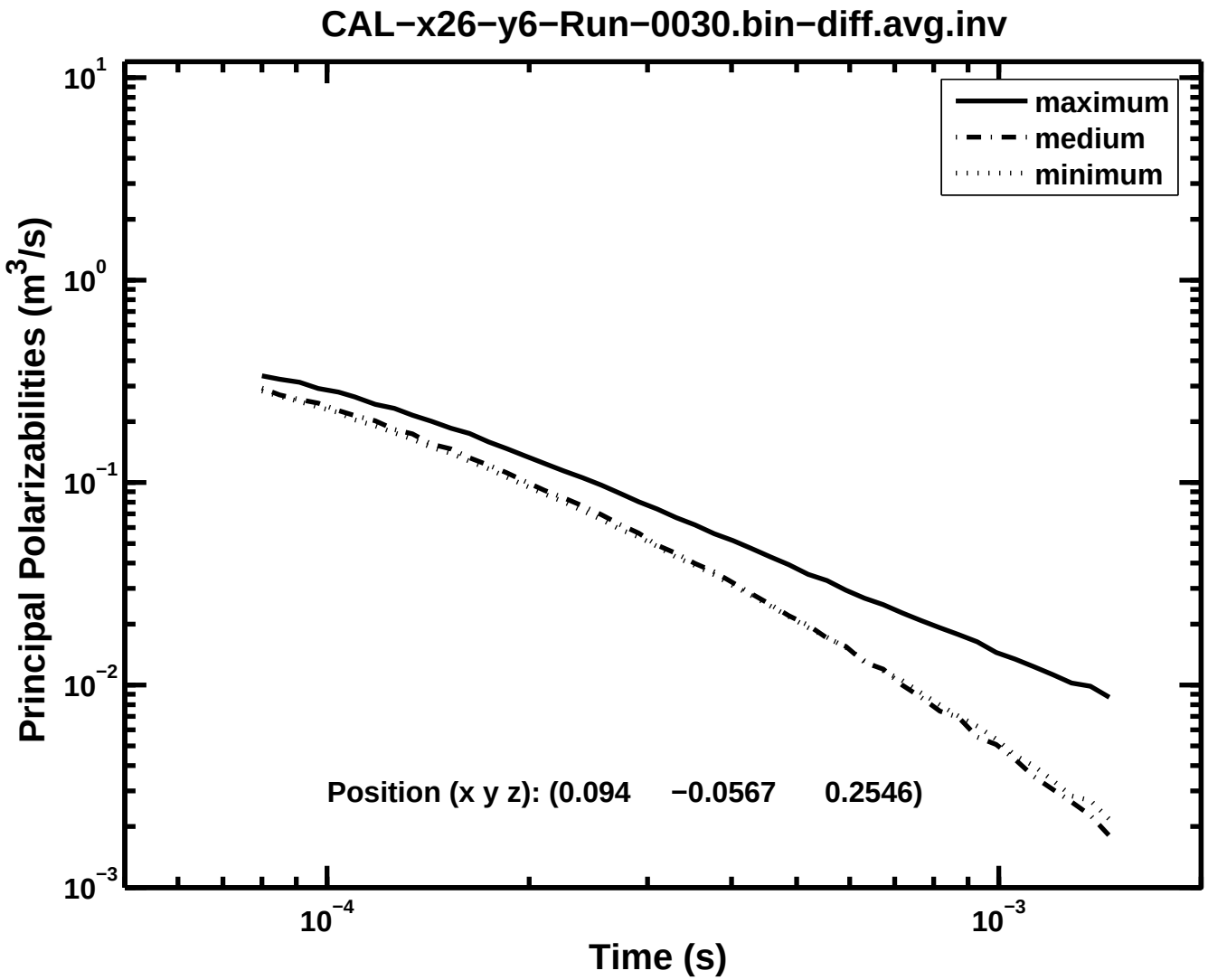
CAL−x26−y6−Run−0030.bin−diff.avg.inv
maximum
medium
minimum
Principal Polarizabilities (m3/s)
10^1
10^0
10^−1
10^−2
10^−3
Position (x y z): (0.094 −0.0567 0.2546)
10^−4
10^−3
Time (s)

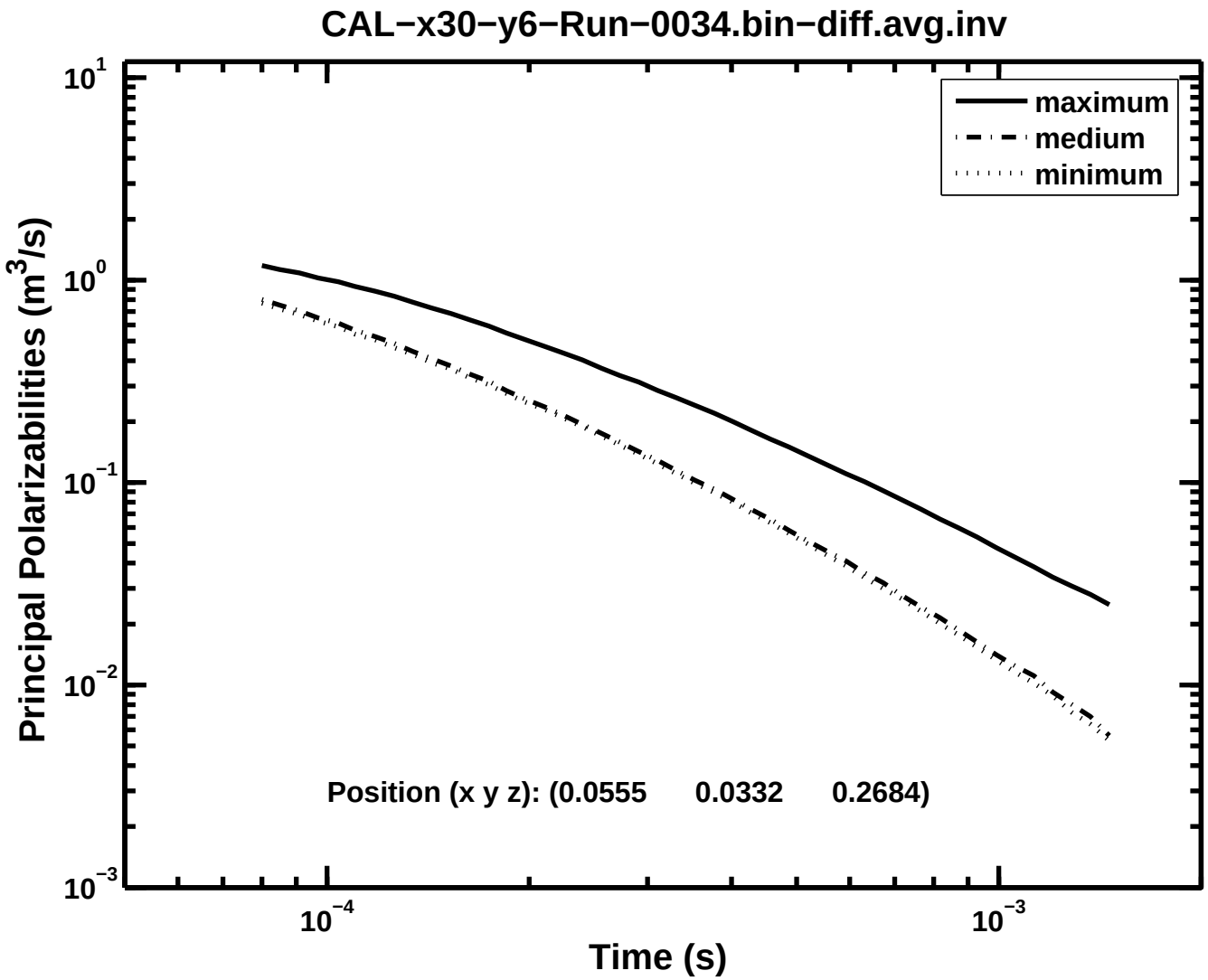
CAL−x30−y6−Run−0034.bin−diff.avg.inv
maximum
medium
minimum
Principal Polarizabilities (m3/s)
10^1
10^0
10^−1
10^−2
10^−3
Position (x y z): (0.0555 0.0332 0.2684)
10^−4
10^−3
Time (s)

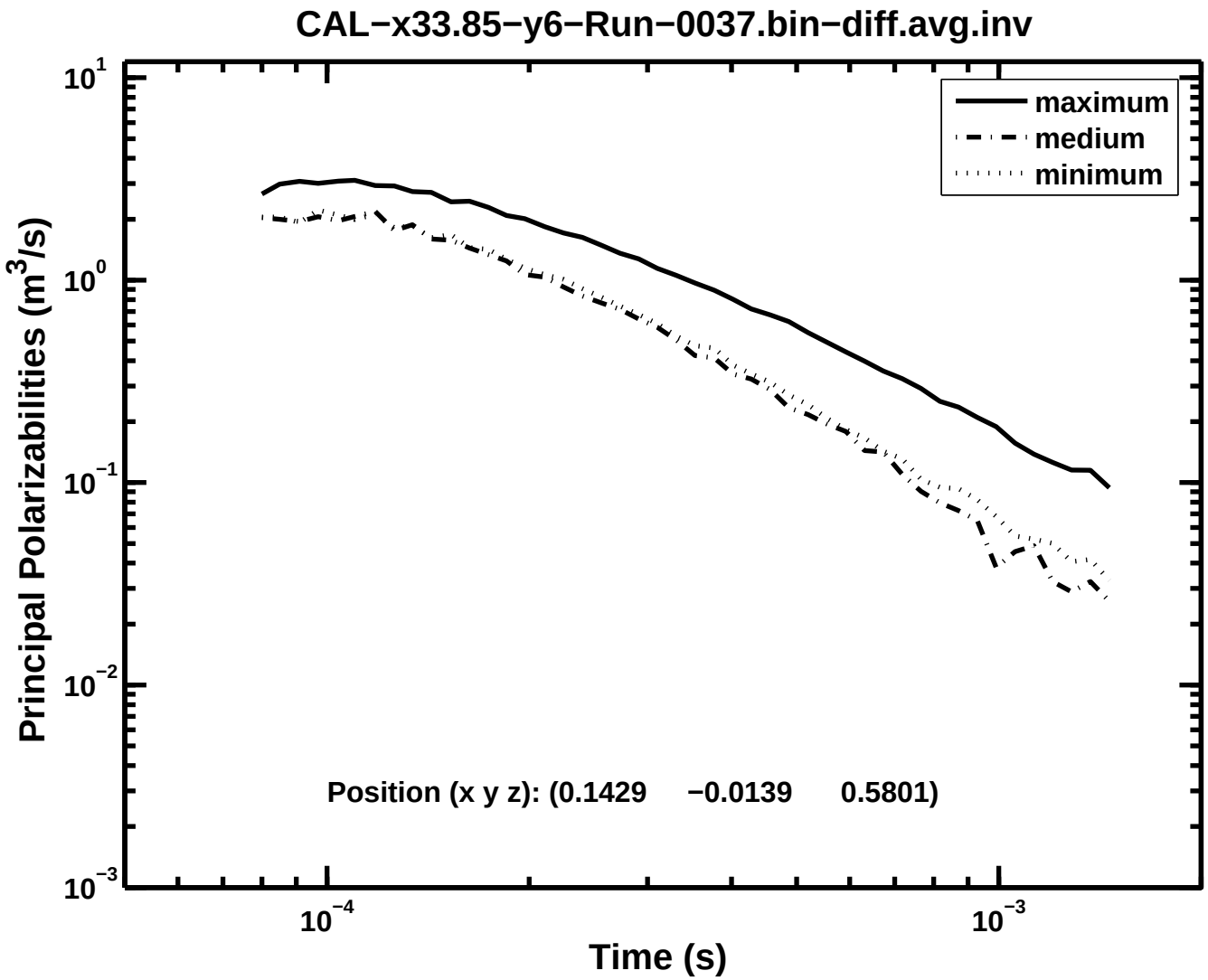
CAL−x33.85−y6−Run−0037.bin−diff.avg.inv
maximum
medium
minimum
Principal Polarizabilities (m3/s)
10^1
10^0
10^−1
10^−2
10^−3
Position (x y z): (0.1429 −0.0139 0.5801)
10^−4
10^−3
Time (s)

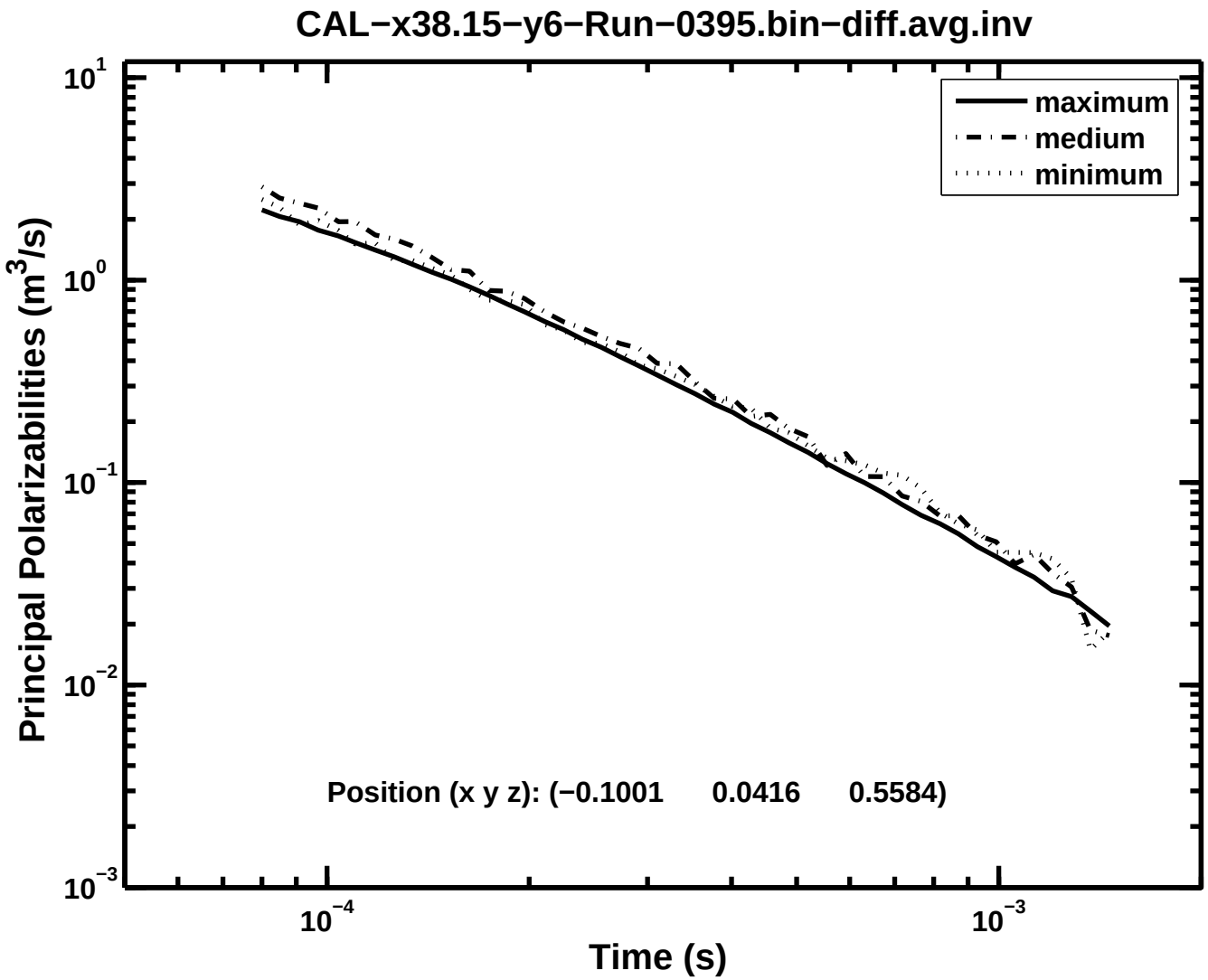
CAL−x38.15−y6−Run−0395.bin−diff.avg.inv
maximum
medium
minimum
Principal Polarizabilities (m3/s)
10^1
10^0
10^−1
10^−2
10^−3
Position (x y z): (−0.1001 0.0416 0.5584)
10^−4
10^−3
Time (s)

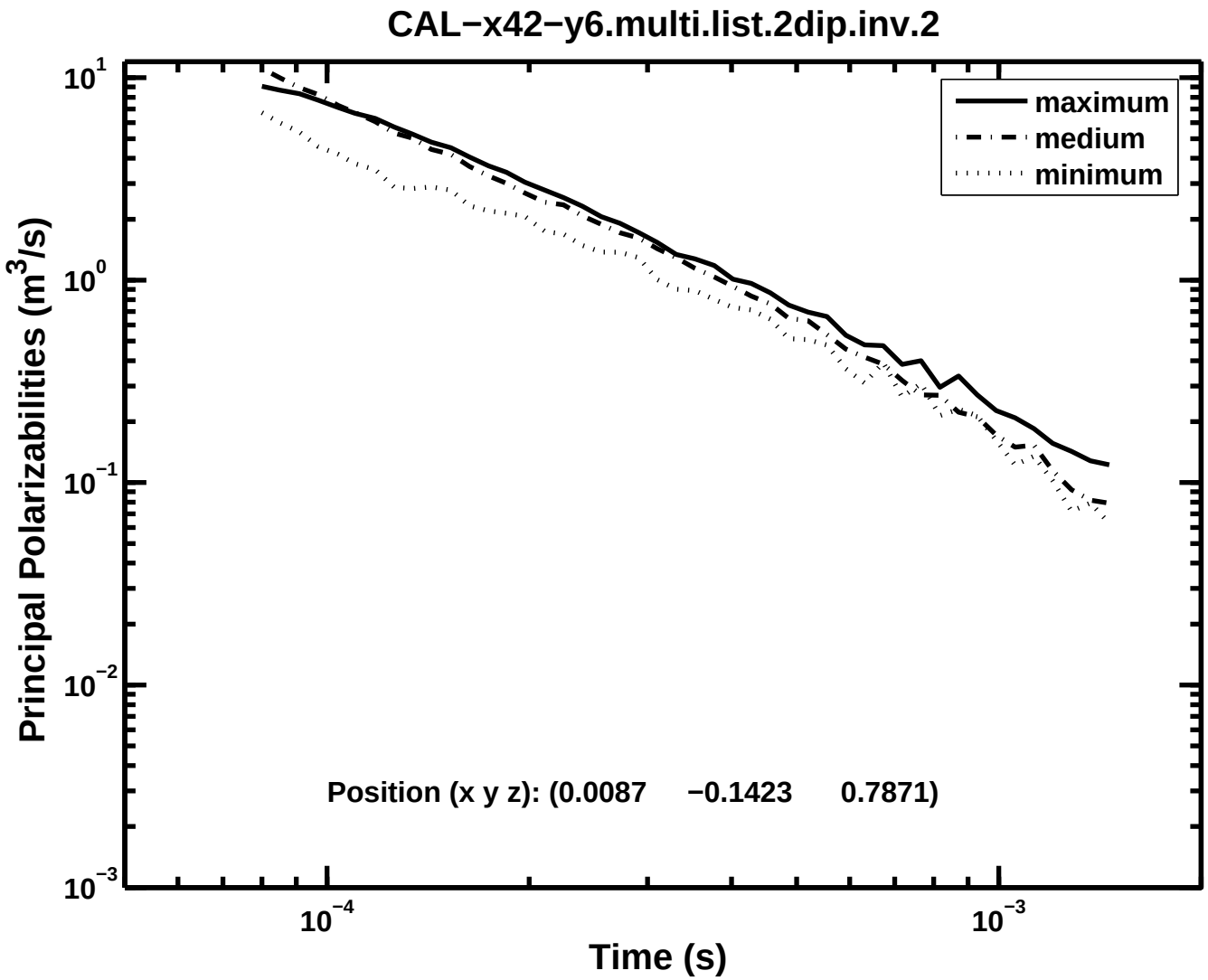
CAL−x42−y6.multi.list.2dip.inv.2
maximum
medium
minimum
Position (x y z): (0.0087 −0.1423 0.7871)
Principal Polarizabilities (m3/s)
Time (s)
10^1
10^0
10^−1
10^−2
10^−3
10^−4
10^−3

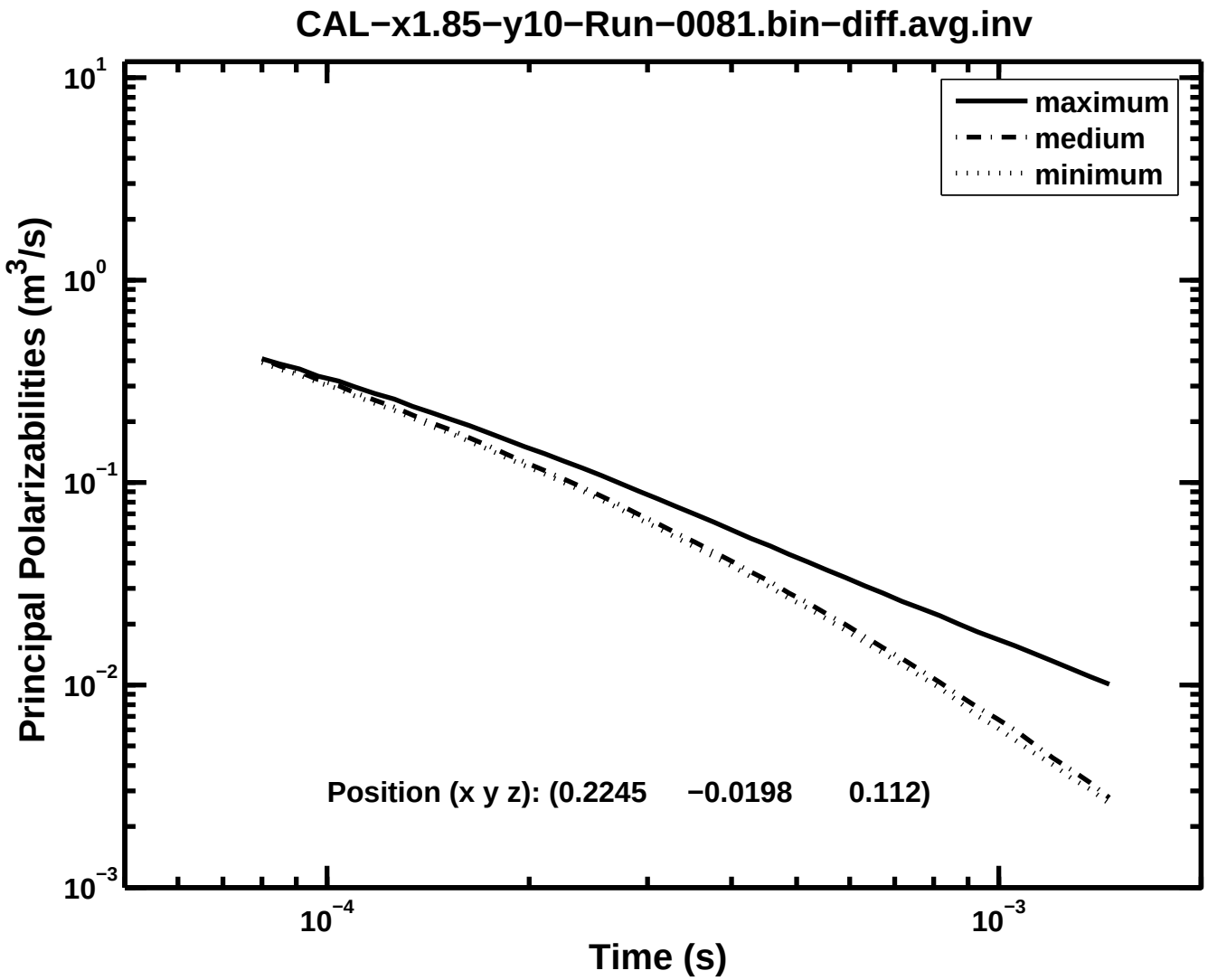
CAL−x1.85−y10−Run−0081.bin−diff.avg.inv
maximum
medium
minimum
Principal Polarizabilities (m3/s)
10^1
10^0
10^−1
10^−2
10^−3
Position (x y z): (0.2245 −0.0198 0.112)
10^−4
10^−3
Time (s)

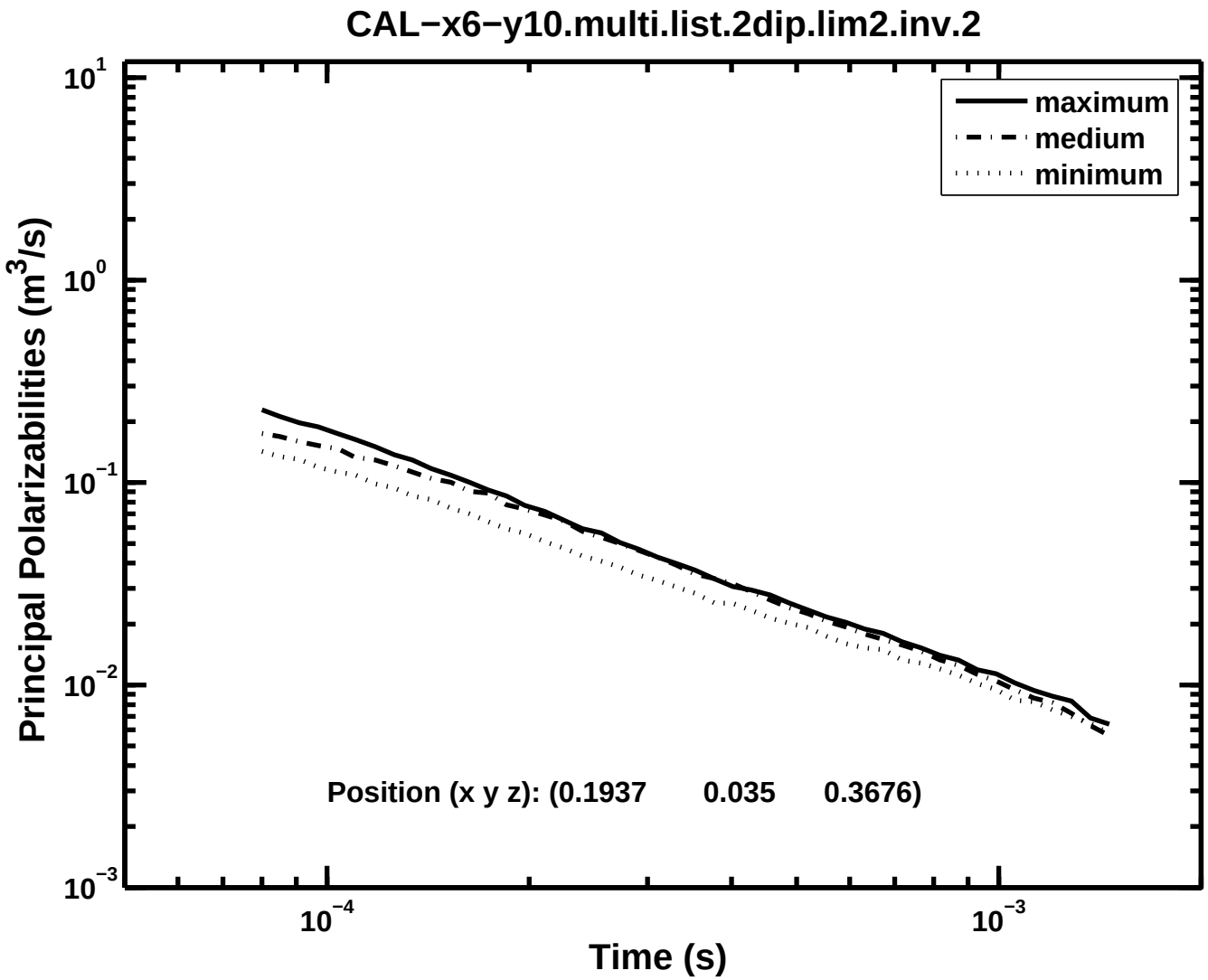
CAL−x6−y10.multi.list.2dip.lim2.inv.2
maximum
medium
minimum
Principal Polarizabilities (m3/s)
10^1
10^0
10^−1
10^−2
10^−3
Position (x y z): (0.1937 0.035 0.3676)
10^−4
10^−3
Time (s)

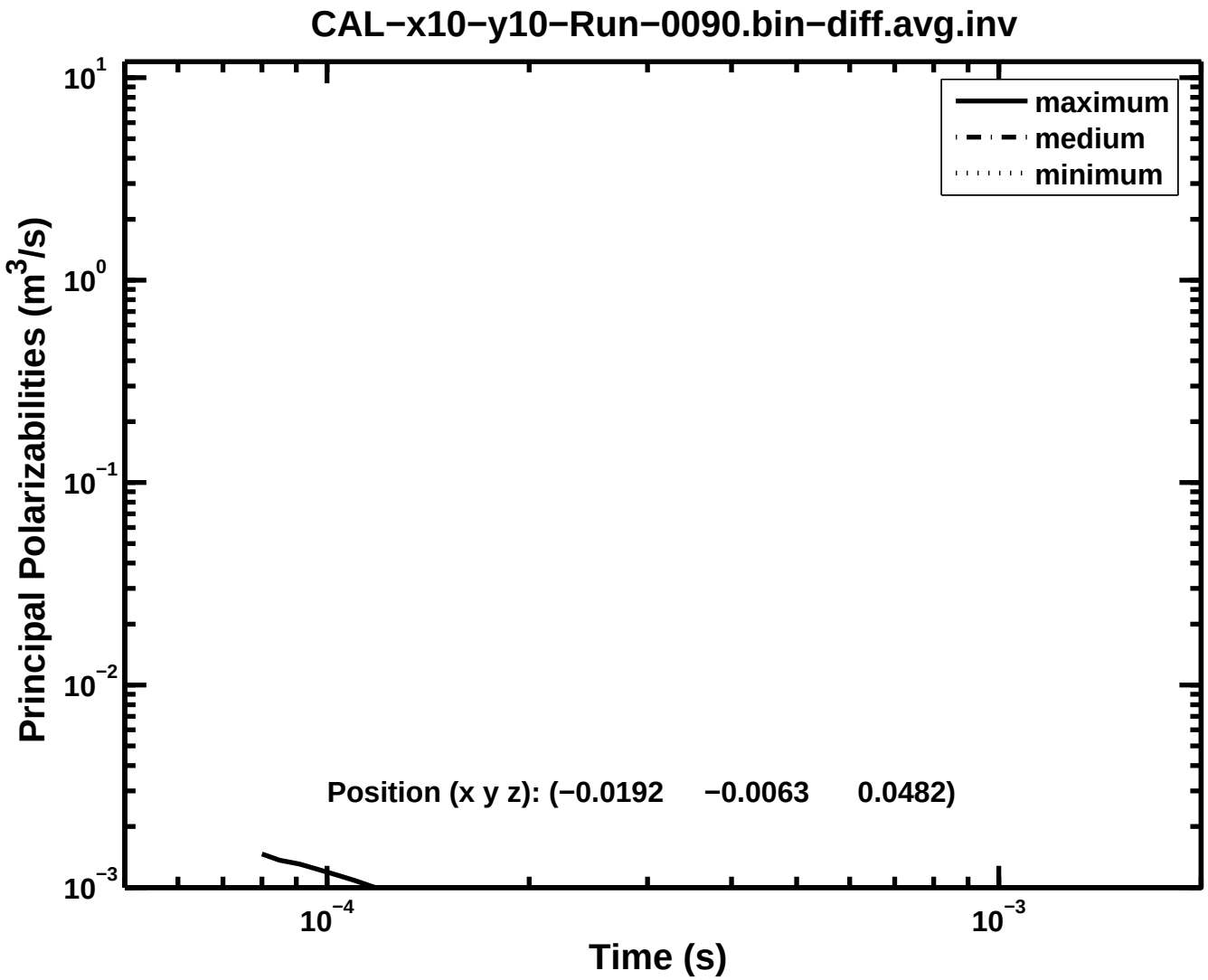
CAL−x10−y10−Run−0090.bin−diff.avg.inv
maximum
medium
minimum
Principal Polarizabilities (m3/s)
10^1
10^0
10^−1
10^−2
10^−3
Position (x y z): (−0.0192 −0.0063 0.0482)
10^−4
10^−3
Time (s)

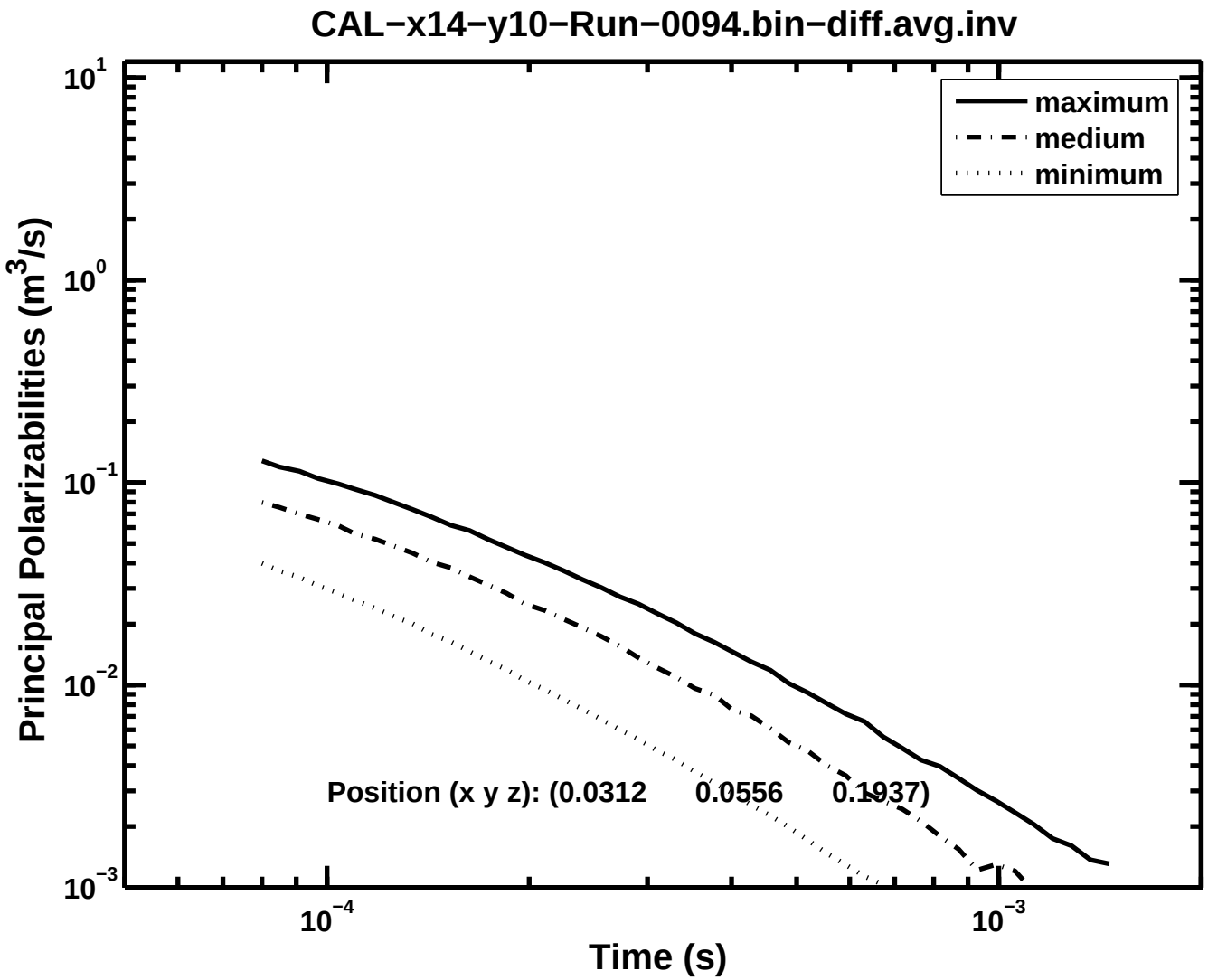
CAL−x14−y10−Run−0094.bin−diff.avg.inv
maximum
medium
minimum
Principal Polarizabilities (m3/s)
10^1
10^0
10^−1
10^−2
10^−3
Position (x y z): (0.0312 0.0556 0.1937)
10^−4
10^−3
Time (s)

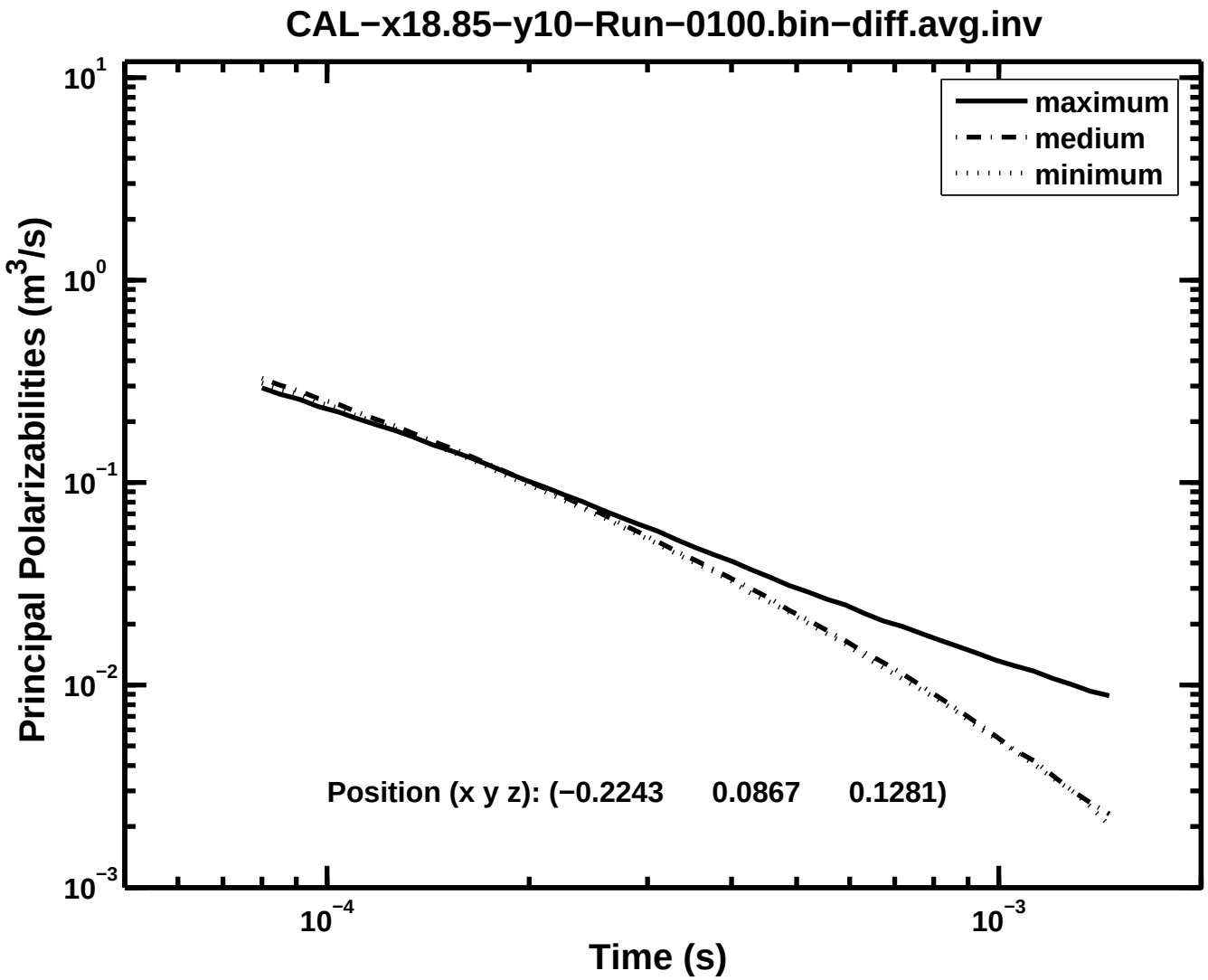
CAL−x18.85−y10−Run−0100.bin−diff.avg.inv
maximum
medium
minimum
Principal Polarizabilities (m3/s)
10^1
10^0
10^−1
10^−2
10^−3
Position (x y z): (−0.2243 0.0867 0.1281)
10^−4
10^−3
Time (s)

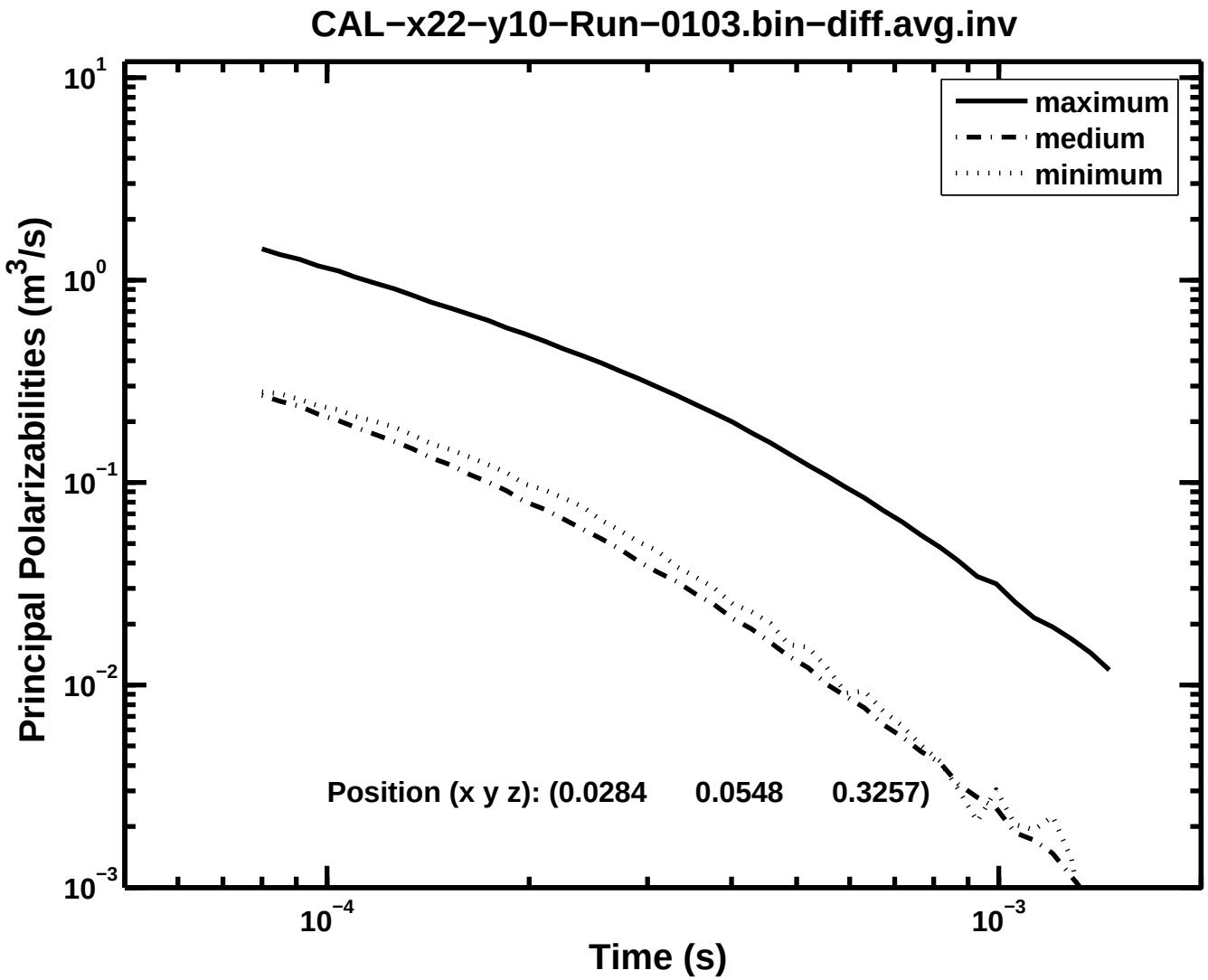
CAL−x22−y10−Run−0103.bin−diff.avg.inv
maximum
medium
minimum
Position (x y z): (0.0284 0.0548 0.3257)
Principal Polarizabilities (m3/s)
Time (s)
10^1
10^0
10^−1
10^−2
10^−3
10^−4
10^−3

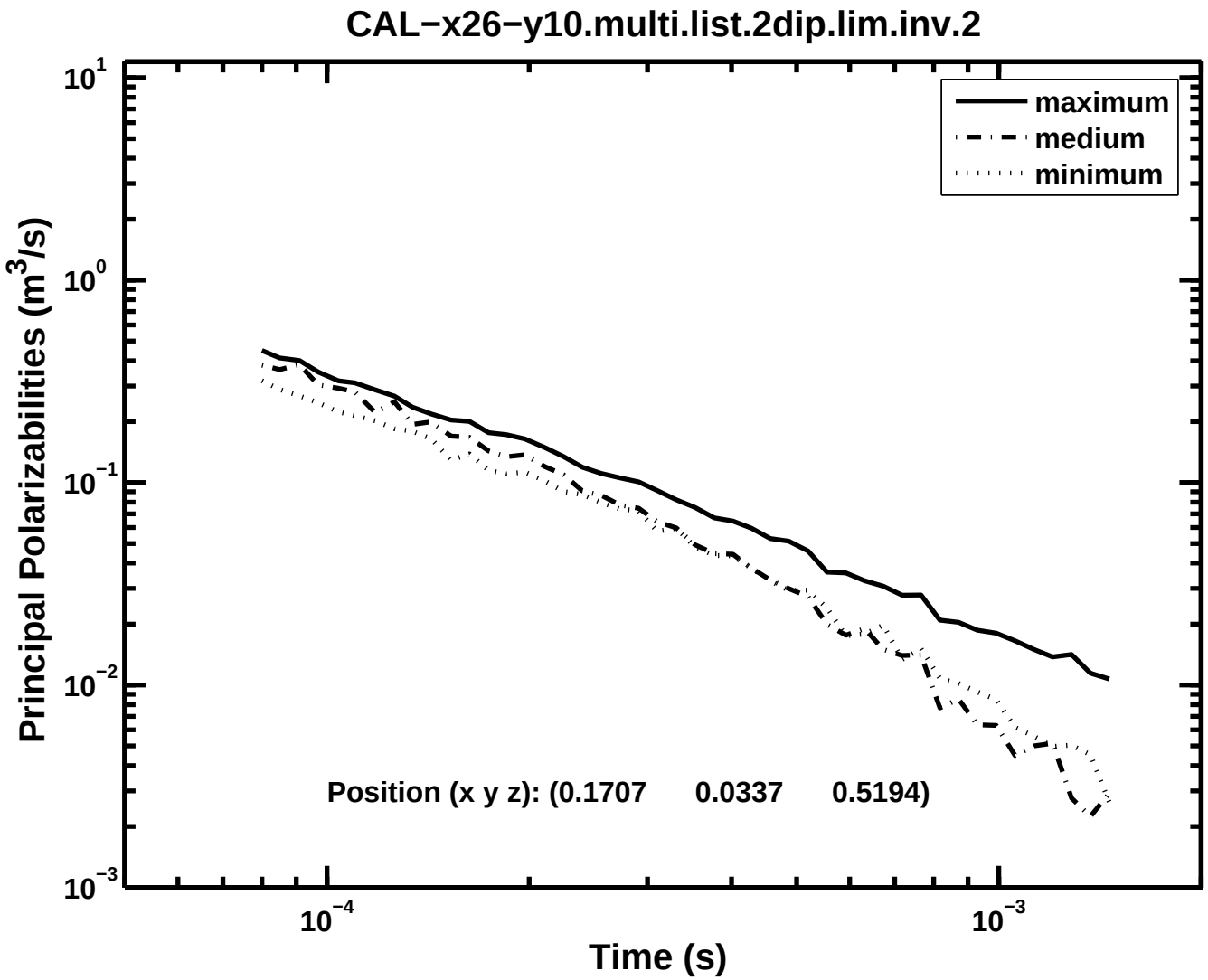
CAL−x26−y10.multi.list.2dip.lim.inv.2
maximum
medium
minimum
Principal Polarizabilities (m3/s)
10^1
10^0
10^−1
10^−2
10^−3
Position (x y z): (0.1707 0.0337 0.5194)
10^−4
10^−3
Time (s)

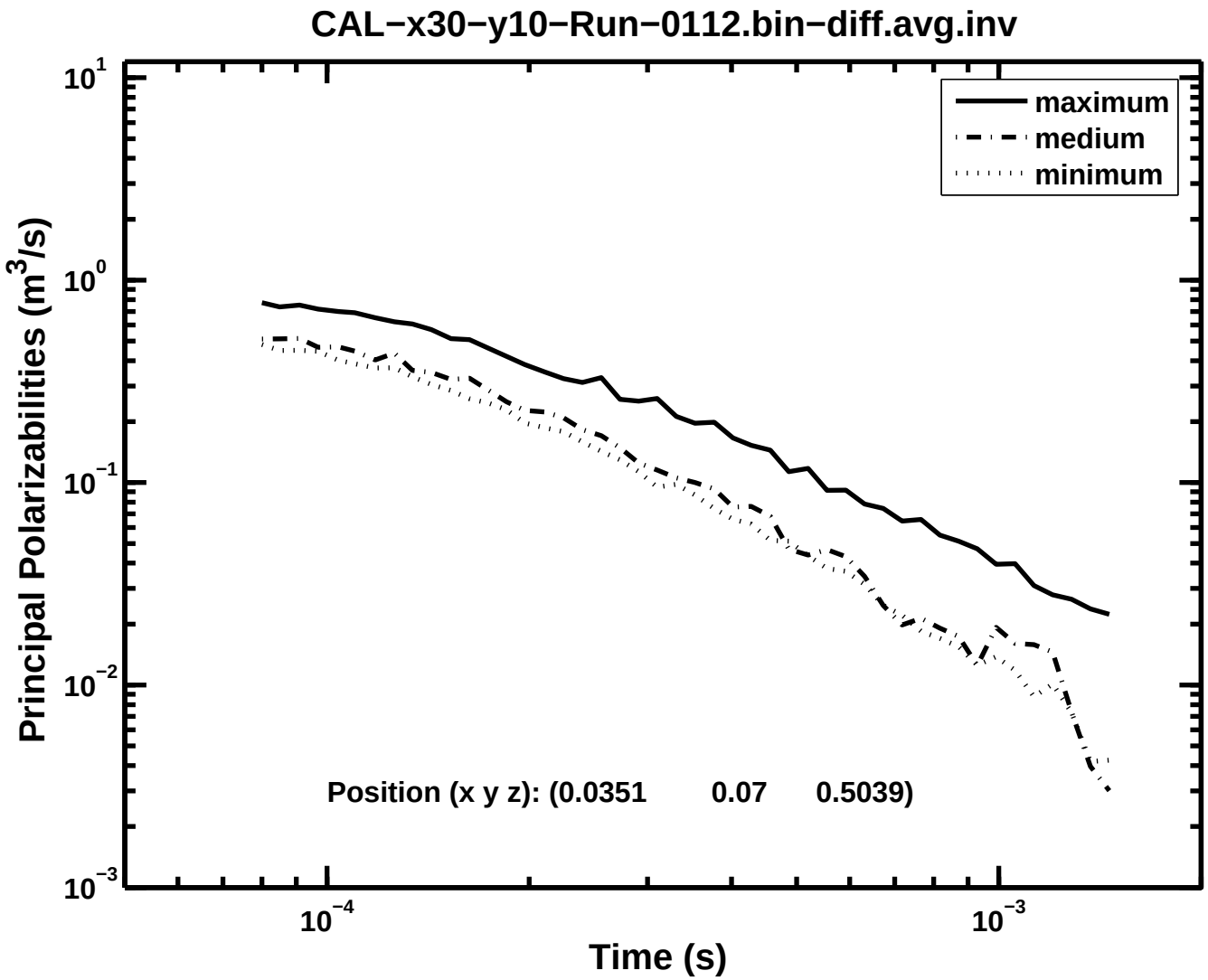
CAL−x30−y10−Run−0112.bin−diff.avg.inv
maximum
medium
minimum
Principal Polarizabilities (m3/s)
10^1
10^0
10^−1
10^−2
10^−3
Position (x y z): (0.0351 0.07 0.5039)
10^−4
10^−3
Time (s)

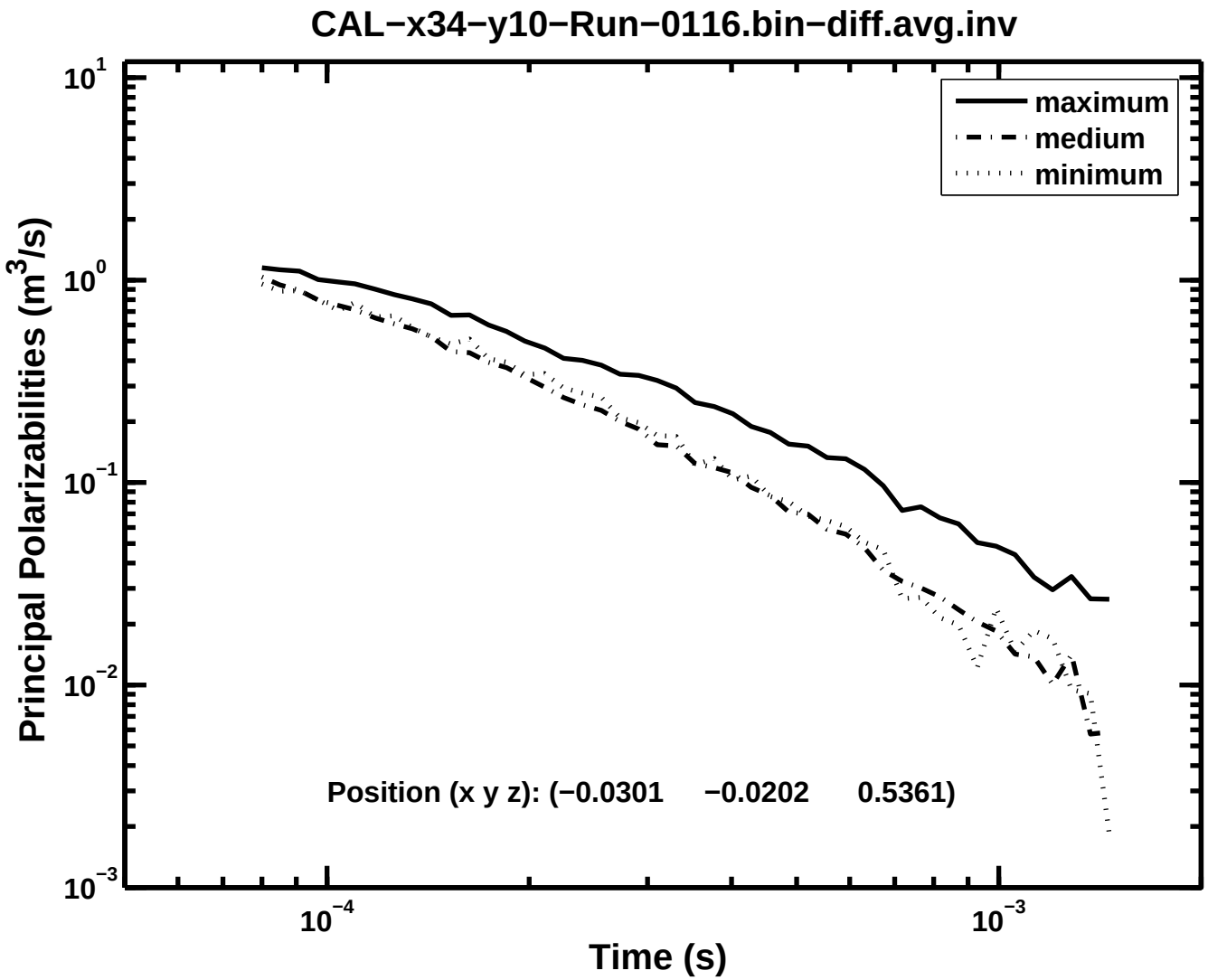
CAL−x34−y10−Run−0116.bin−diff.avg.inv
maximum
medium
minimum
Principal Polarizabilities (m3/s)
10^1
10^0
10^−1
10^−2
10^−3
Position (x y z): (−0.0301 −0.0202 0.5361)
10^−4
10^−3
Time (s)

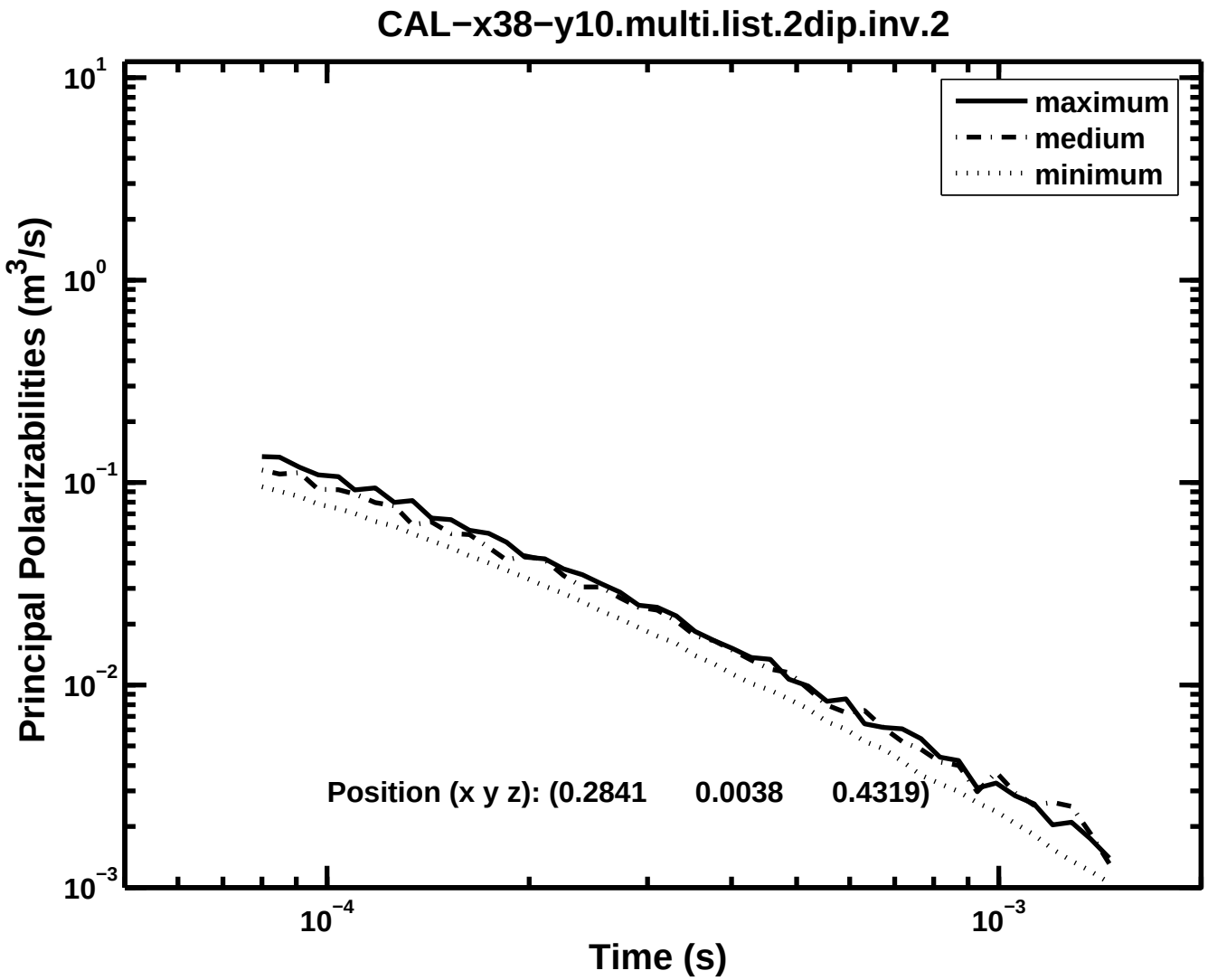
CAL−x38−y10.multi.list.2dip.inv.2
maximum
medium
minimum
Principal Polarizabilities (m3/s)
10^1
10^0
10^−1
10^−2
10^−3
Position (x y z): (0.2841 0.0038 0.4319)
10^−4
10^−3
Time (s)

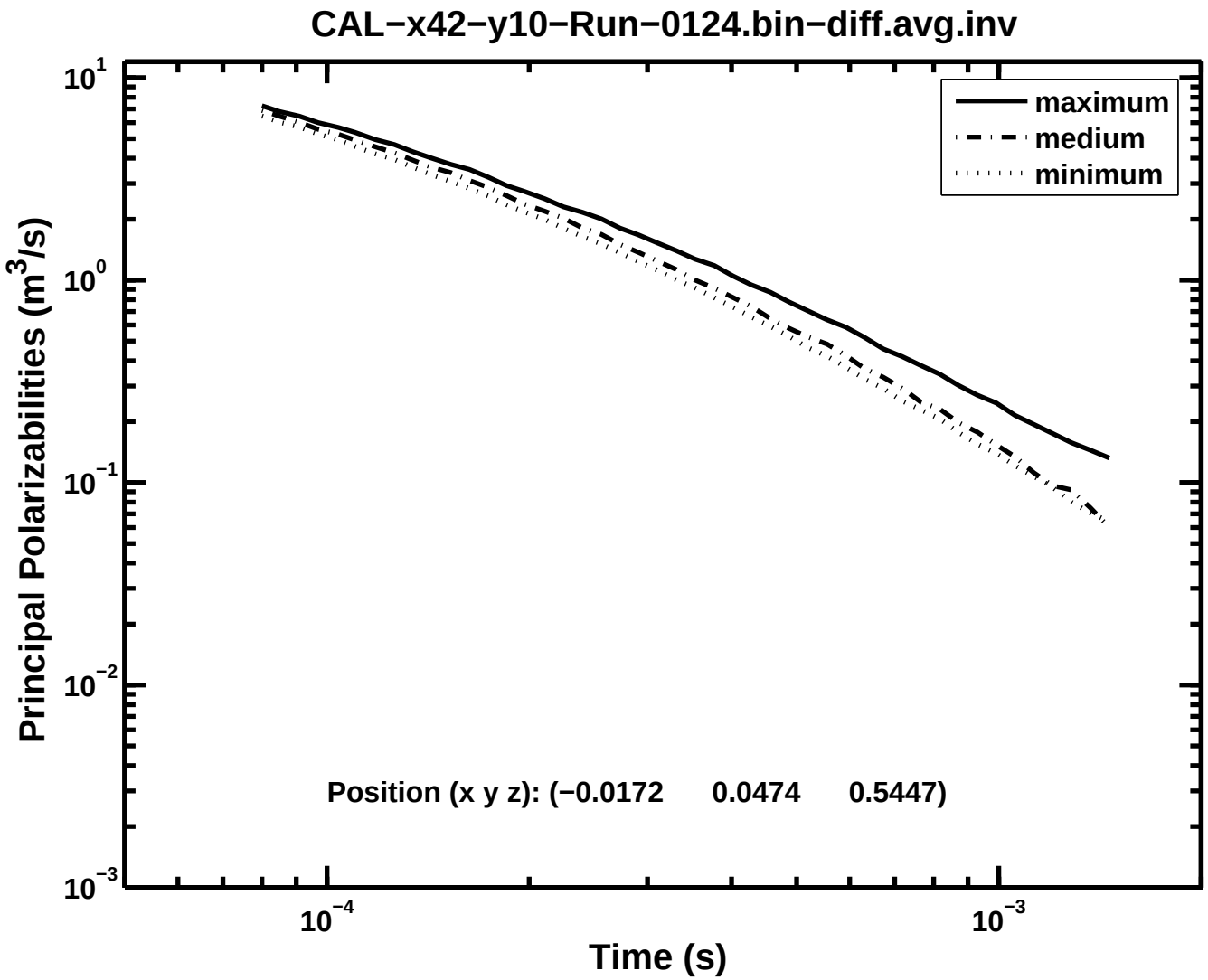
CAL−x42−y10−Run−0124.bin−diff.avg.inv
maximum
medium
minimum
Principal Polarizabilities (m3/s)
10^1
10^0
10^−1
10^−2
10^−3
Position (x y z): (−0.0172 0.0474 0.5447)
10^−4
10^−3
Time (s)

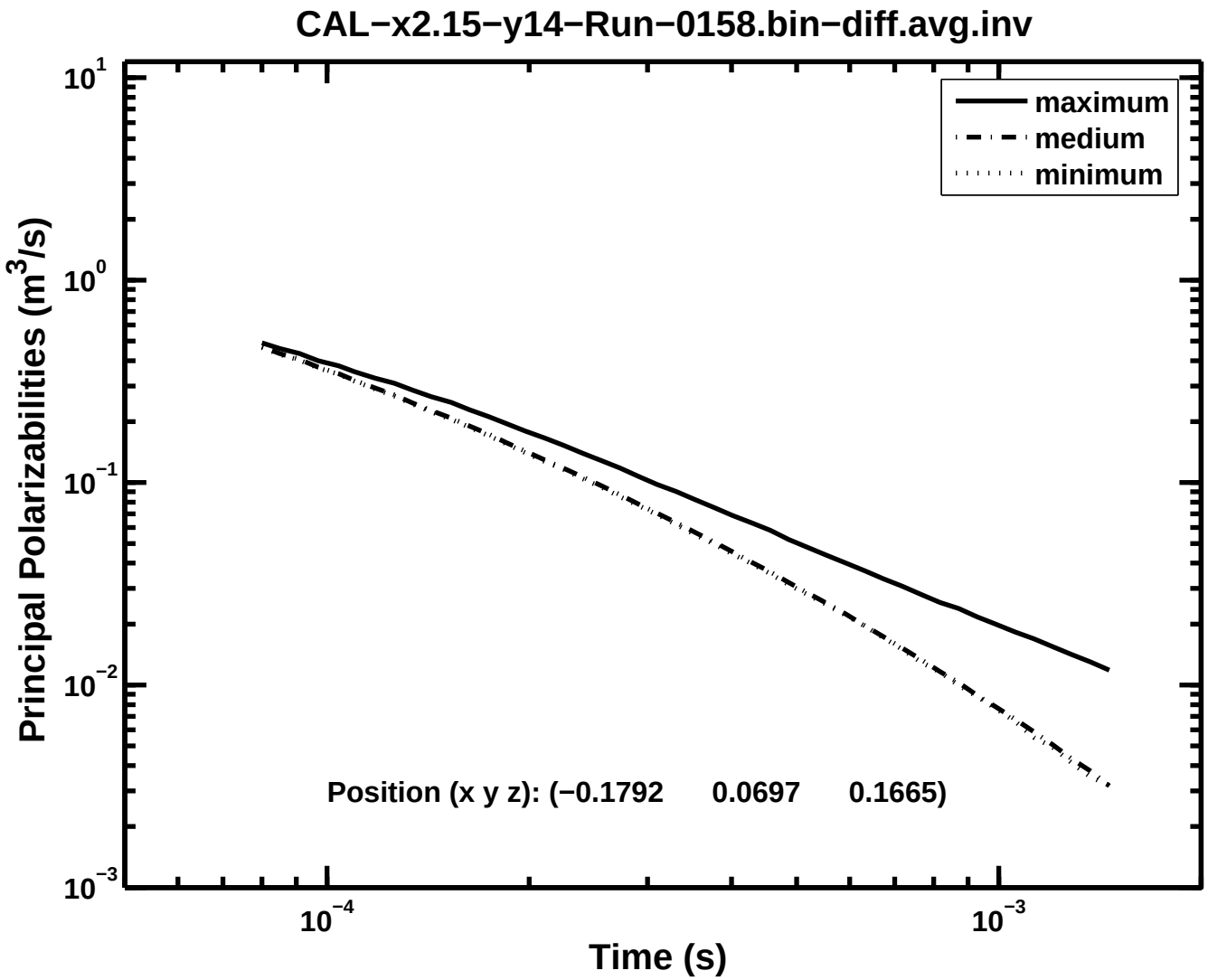
CAL−x2.15−y14−Run−0158.bin−diff.avg.inv
maximum
medium
minimum
Principal Polarizabilities (m3/s)
10^1
10^0
10^−1
10^−2
10^−3
Position (x y z): (−0.1792 0.0697 0.1665)
10^−4
10^−3
Time (s)

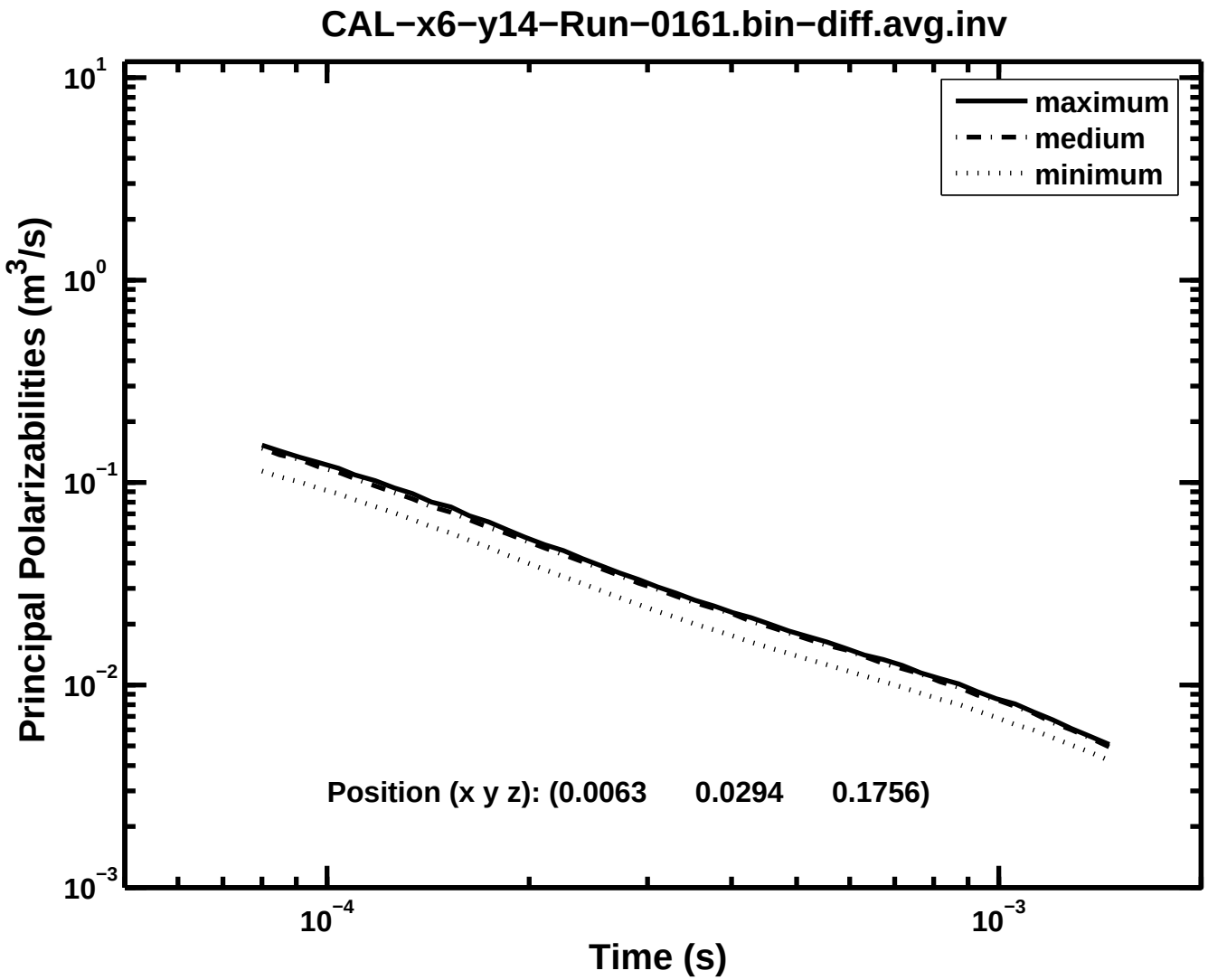
CAL−x6−y14−Run−0161.bin−diff.avg.inv
maximum
medium
minimum
Principal Polarizabilities (m3/s)
10^1
10^0
10^−1
10^−2
10^−3
Position (x y z): (0.0063 0.0294 0.1756)
10^−4
10^−3
Time (s)

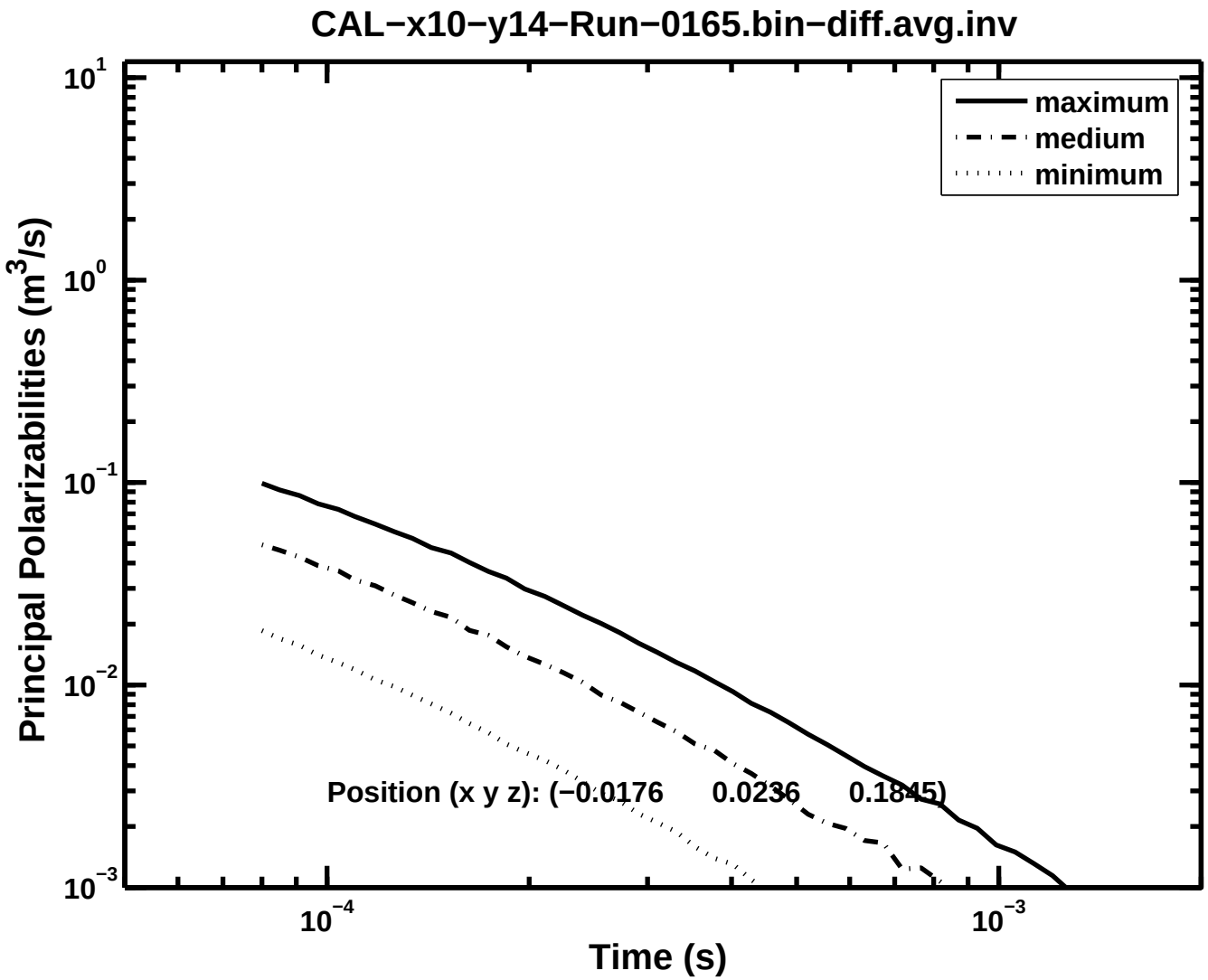
CAL−x10−y14−Run−0165.bin−diff.avg.inv
maximum
medium
minimum
Principal Polarizabilities (m3/s)
10^1
10^0
10^−1
10^−2
10^−3
Position (x y z): (−0.0176 0.0236 0.1845)
10^−4
10^−3
Time (s)

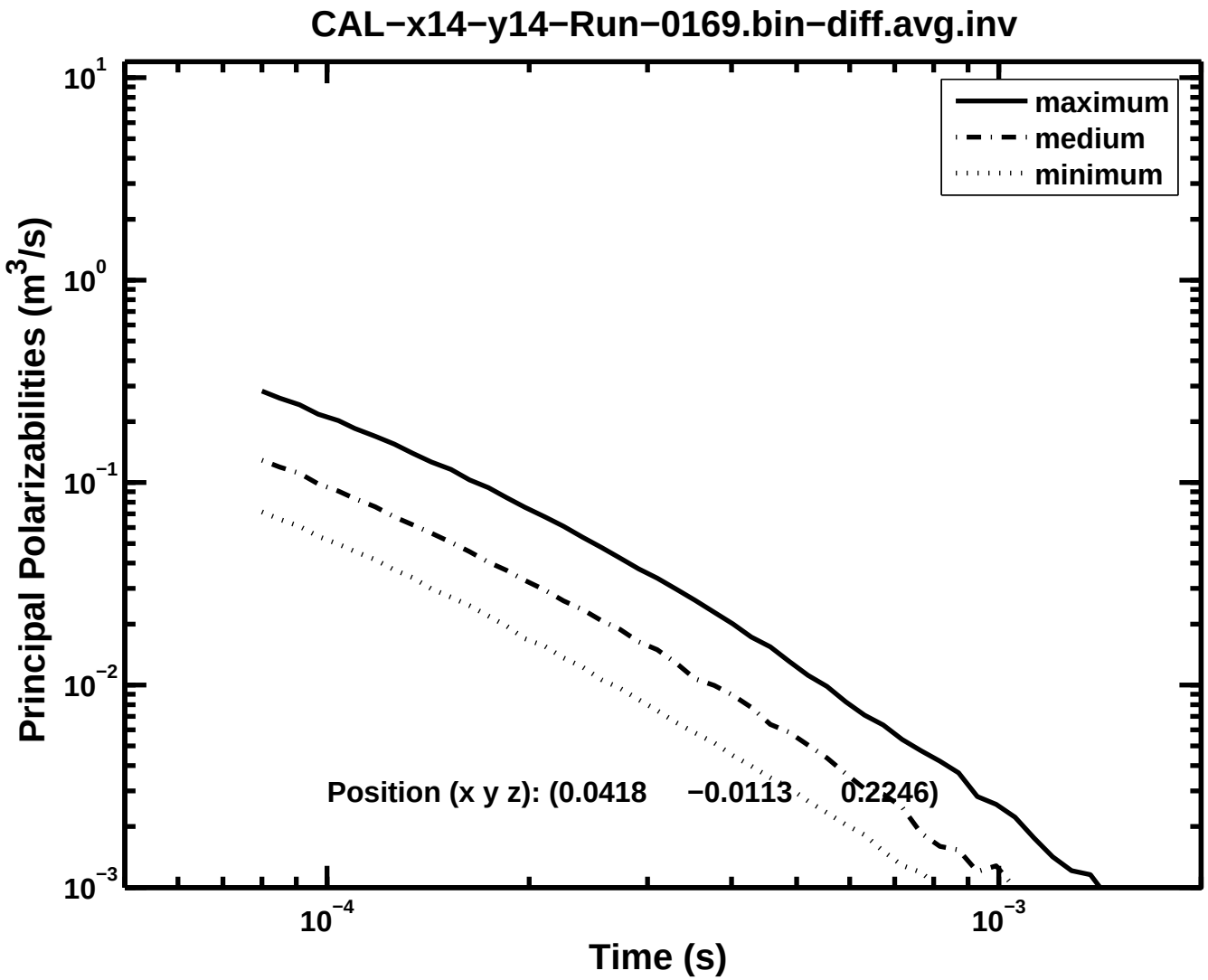
CAL−x14−y14−Run−0169.bin−diff.avg.inv
maximum
medium
minimum
Principal Polarizabilities (m3/s)
10^1
10^0
10^−1
10^−2
10^−3
Position (x y z): (0.0418 −0.0113 0.2246)
10^−4
10^−3
Time (s)

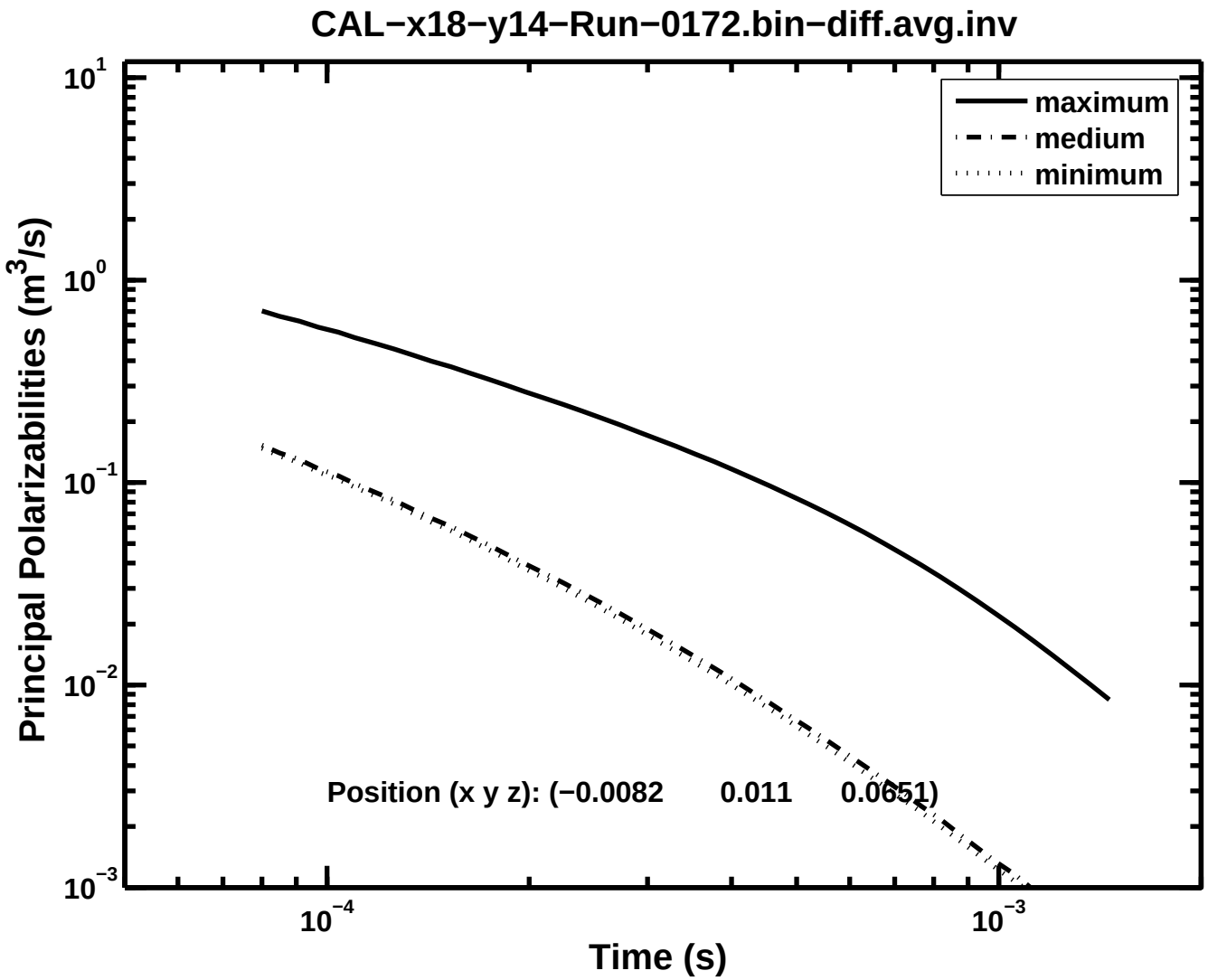
CAL−x18−y14−Run−0172.bin−diff.avg.inv
maximum
medium
minimum
Principal Polarizabilities (m3/s)
10^1
10^0
10^−1
10^−2
10^−3
Position (x y z): (−0.0082 0.011 0.0651)
10^−4
10^−3
Time (s)

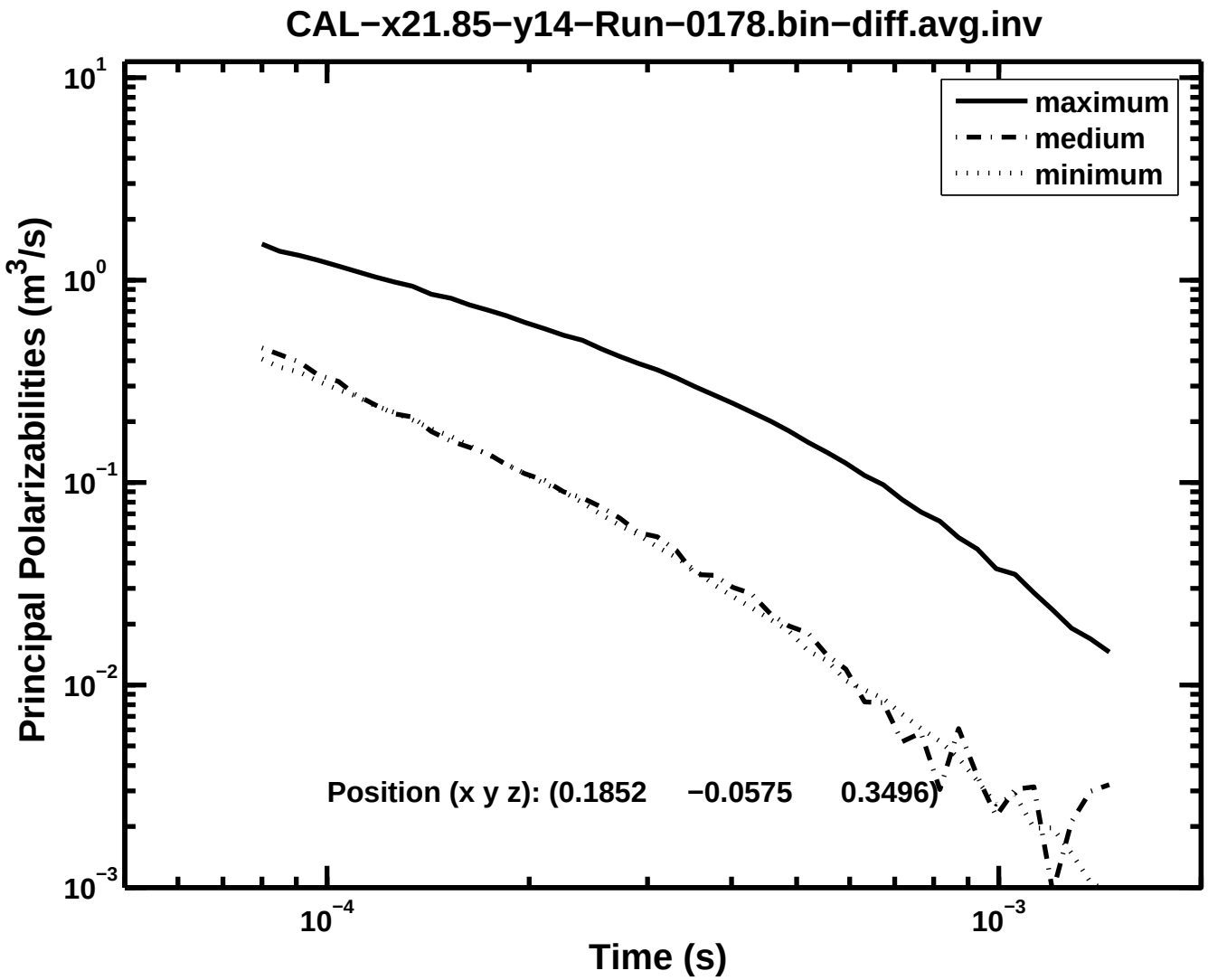
CAL−x21.85−y14−Run−0178.bin−diff.avg.inv
maximum
medium
minimum
Position (x y z): (0.1852 −0.0575 0.3496)
Principal Polarizabilities (m3/s)
Time (s)
10^1
10^0
10^−1
10^−2
10^−3
10^−4
10^−3

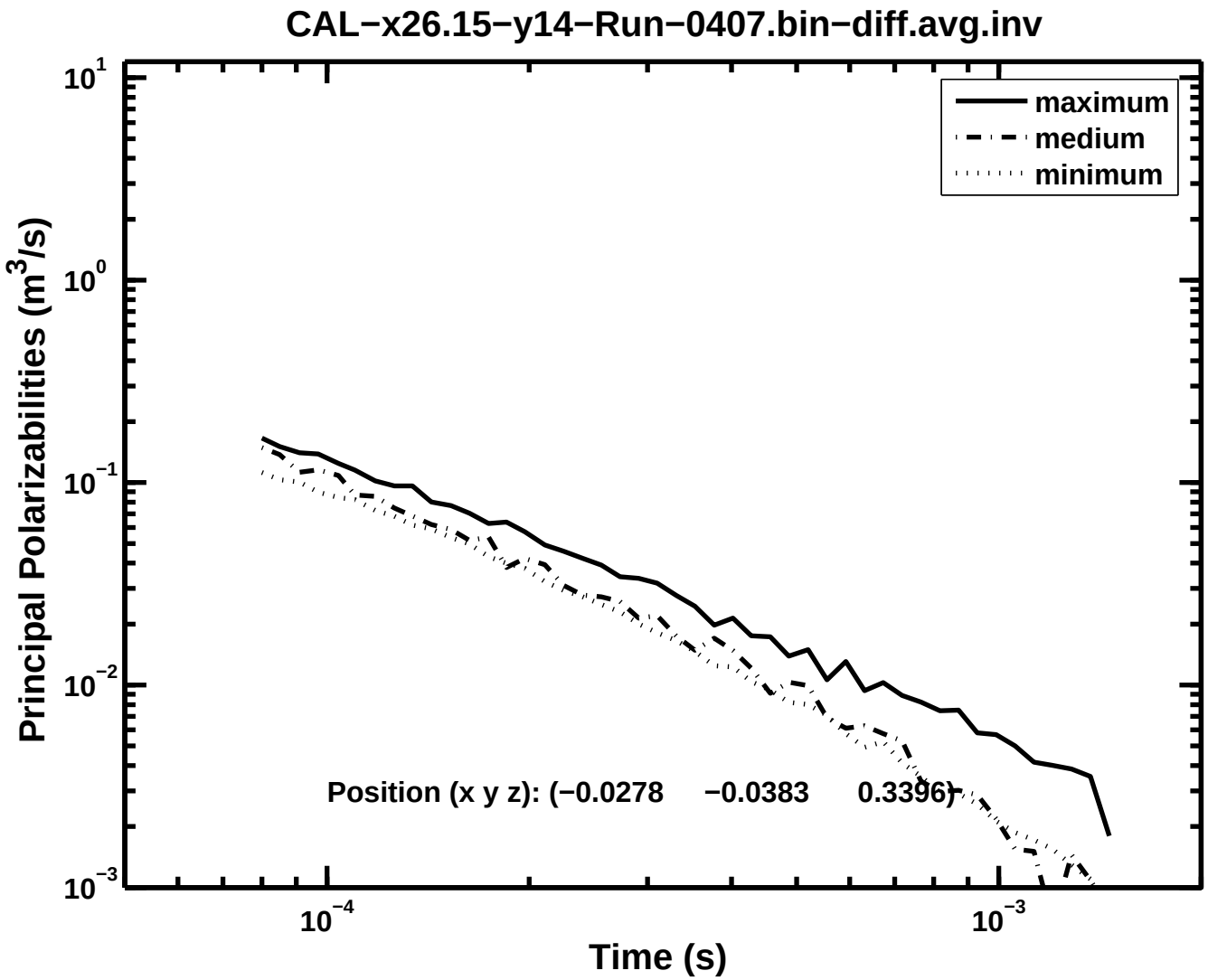
CAL−x26.15−y14−Run−0407.bin−diff.avg.inv
maximum
medium
minimum
Principal Polarizabilities (m3/s)
10^1
10^0
10^−1
10^−2
10^−3
Position (x y z): (−0.0278 −0.0383 0.3396)
10^−4
10^−3
Time (s)

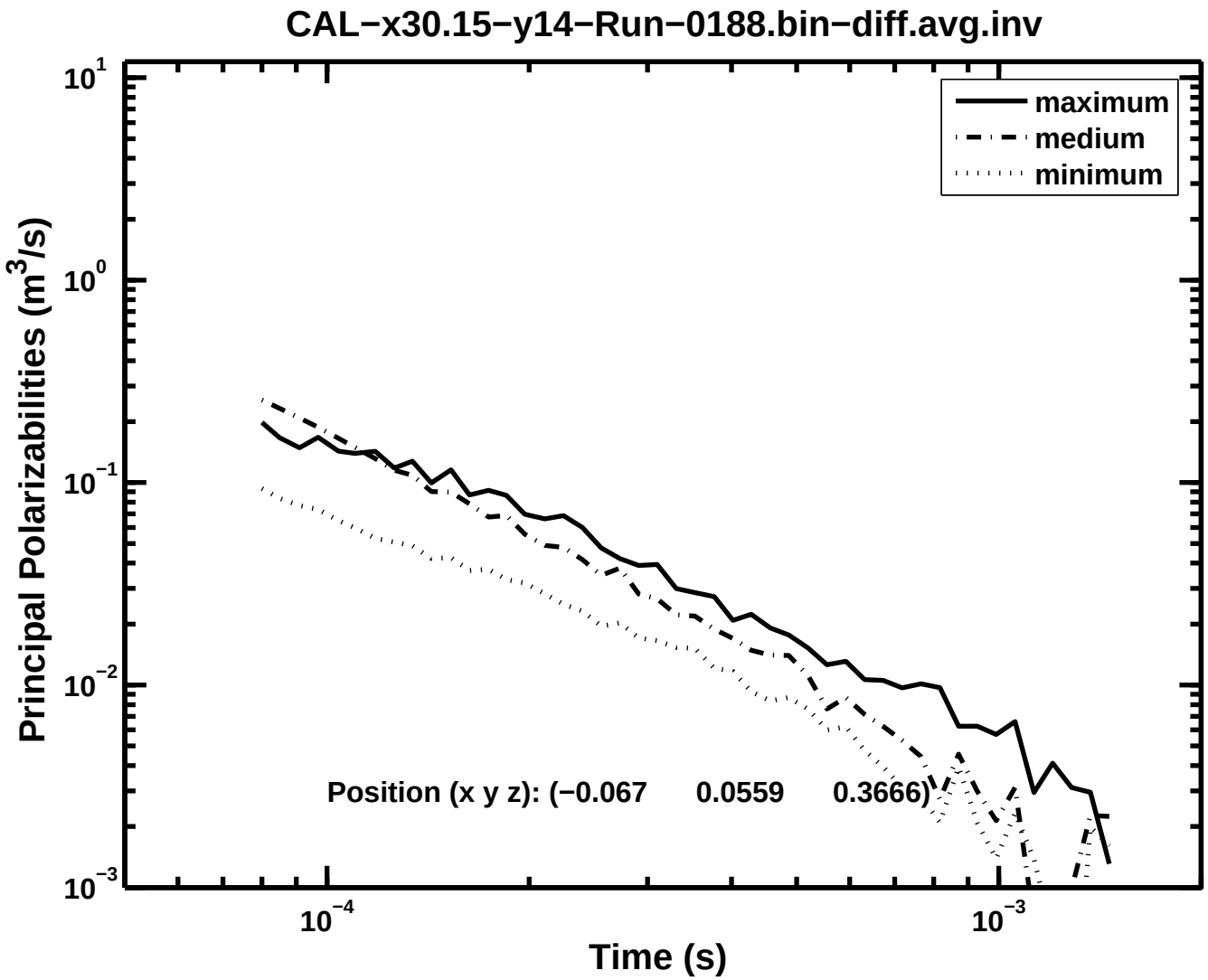
CAL−x30.15−y14−Run−0188.bin−diff.avg.inv
maximum
medium
minimum
Principal Polarizabilities (m3/s)
10^1
10^0
10^−1
10^−2
10^−3
10^−4
10^−3
Time (s)
Position (x y z): (−0.067 0.0559 0.3666)

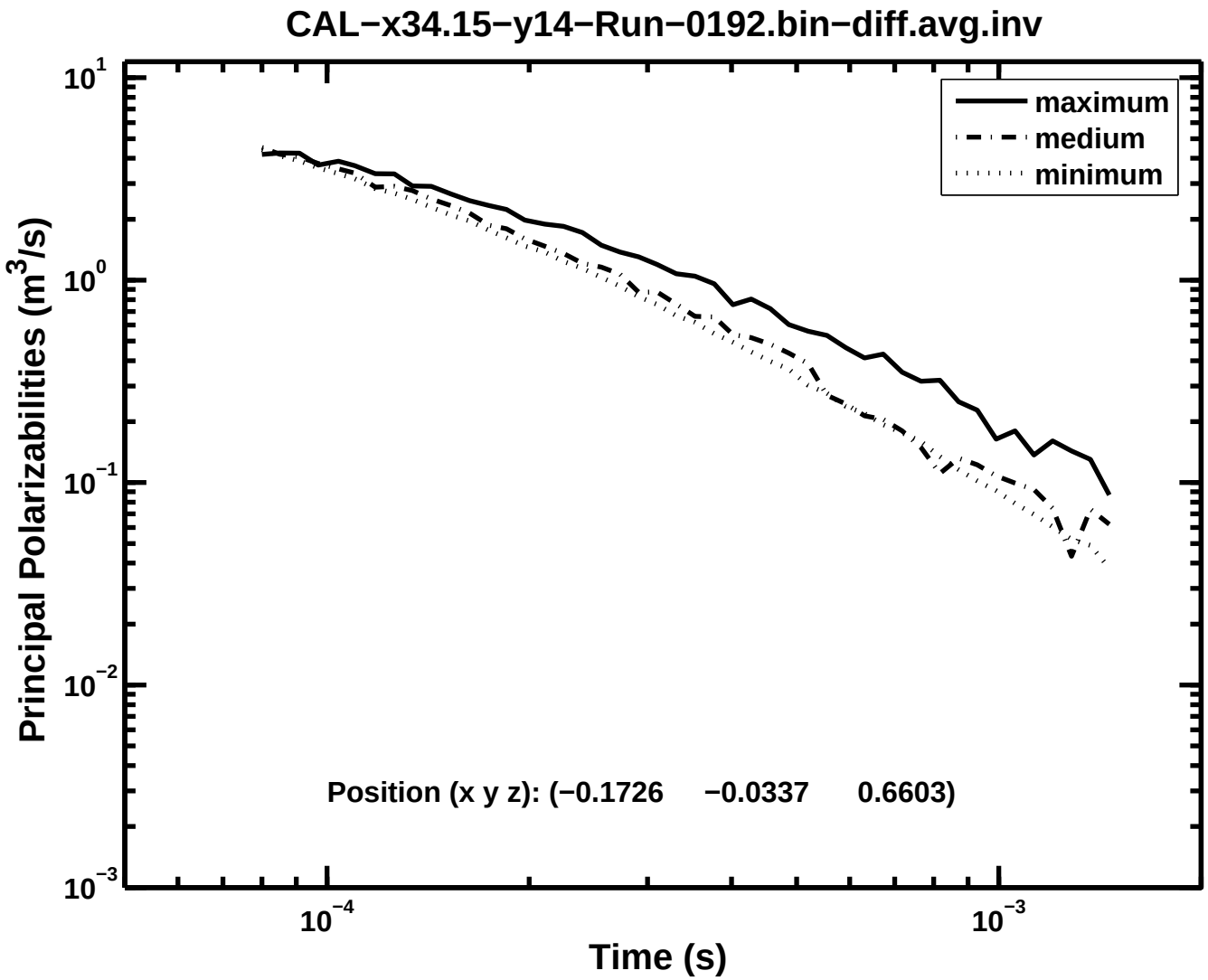
CAL−x34.15−y14−Run−0192.bin−diff.avg.inv
maximum
medium
minimum
Principal Polarizabilities (m3/s)
10^1
10^0
10^−1
10^−2
10^−3
Position (x y z): (−0.1726 −0.0337 0.6603)
10^−4
10^−3
Time (s)

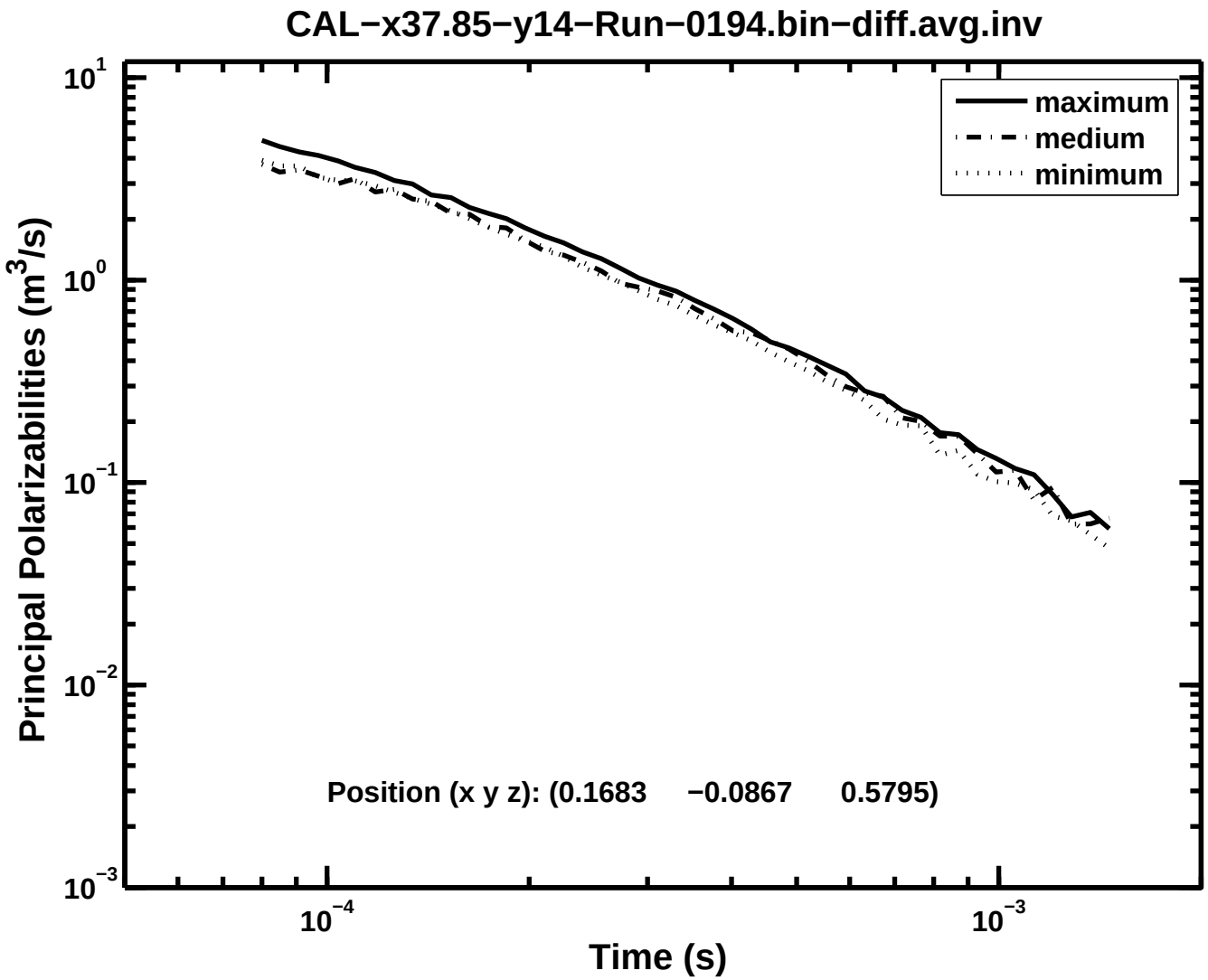
CAL−x37.85−y14−Run−0194.bin−diff.avg.inv
maximum
medium
minimum
Principal Polarizabilities (m3/s)
10^1
10^0
10^−1
10^−2
10^−3
Position (x y z): (0.1683 −0.0867 0.5795)
10^−4
10^−3
Time (s)

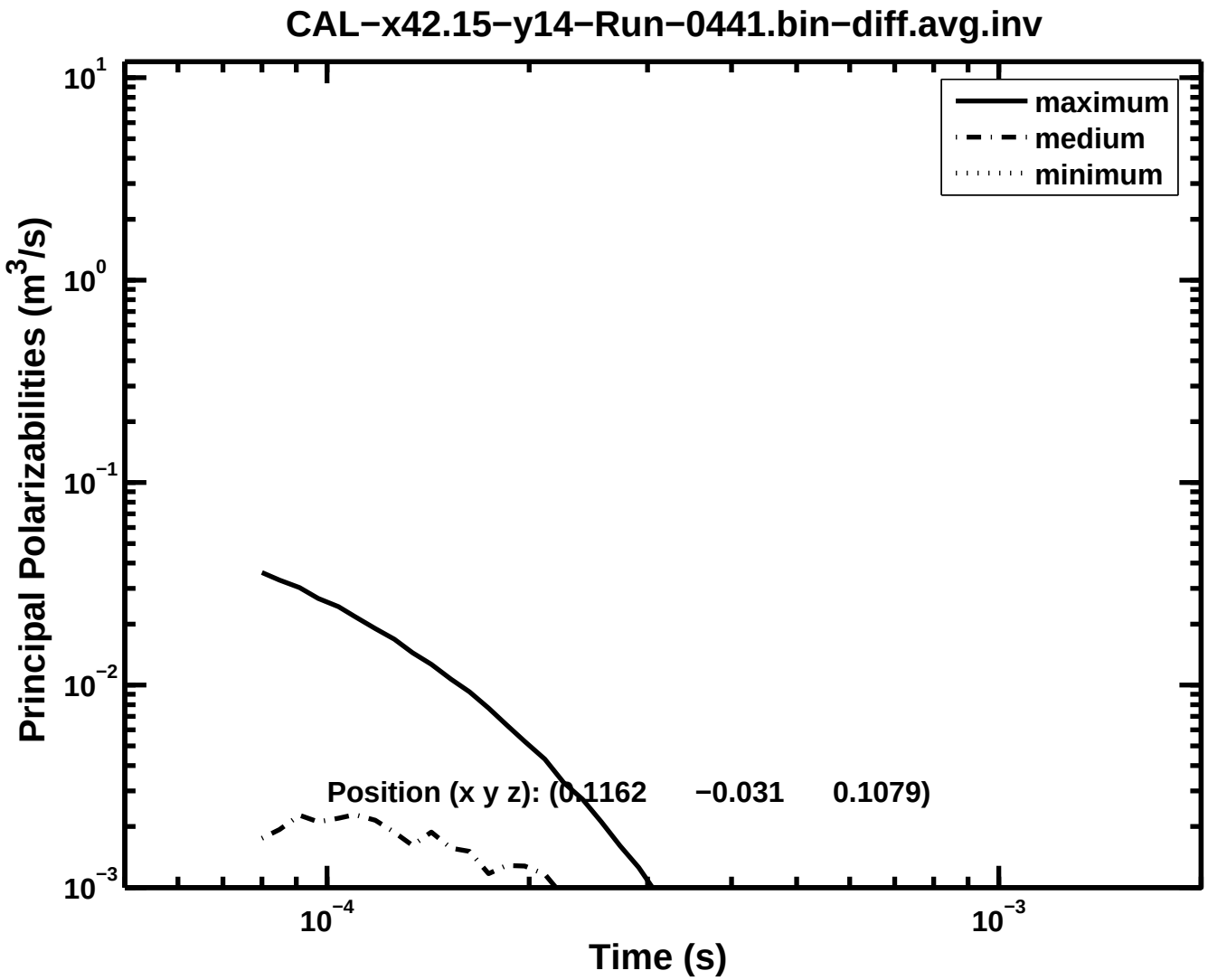
CAL−x42.15−y14−Run−0441.bin−diff.avg.inv
maximum
medium
minimum
Position (x y z): (0.1162 −0.031 0.1079)
Principal Polarizabilities (m3/s)
Time (s)
10^1
10^0
10^−1
10^−2
10^−3
10^−4
10^−3

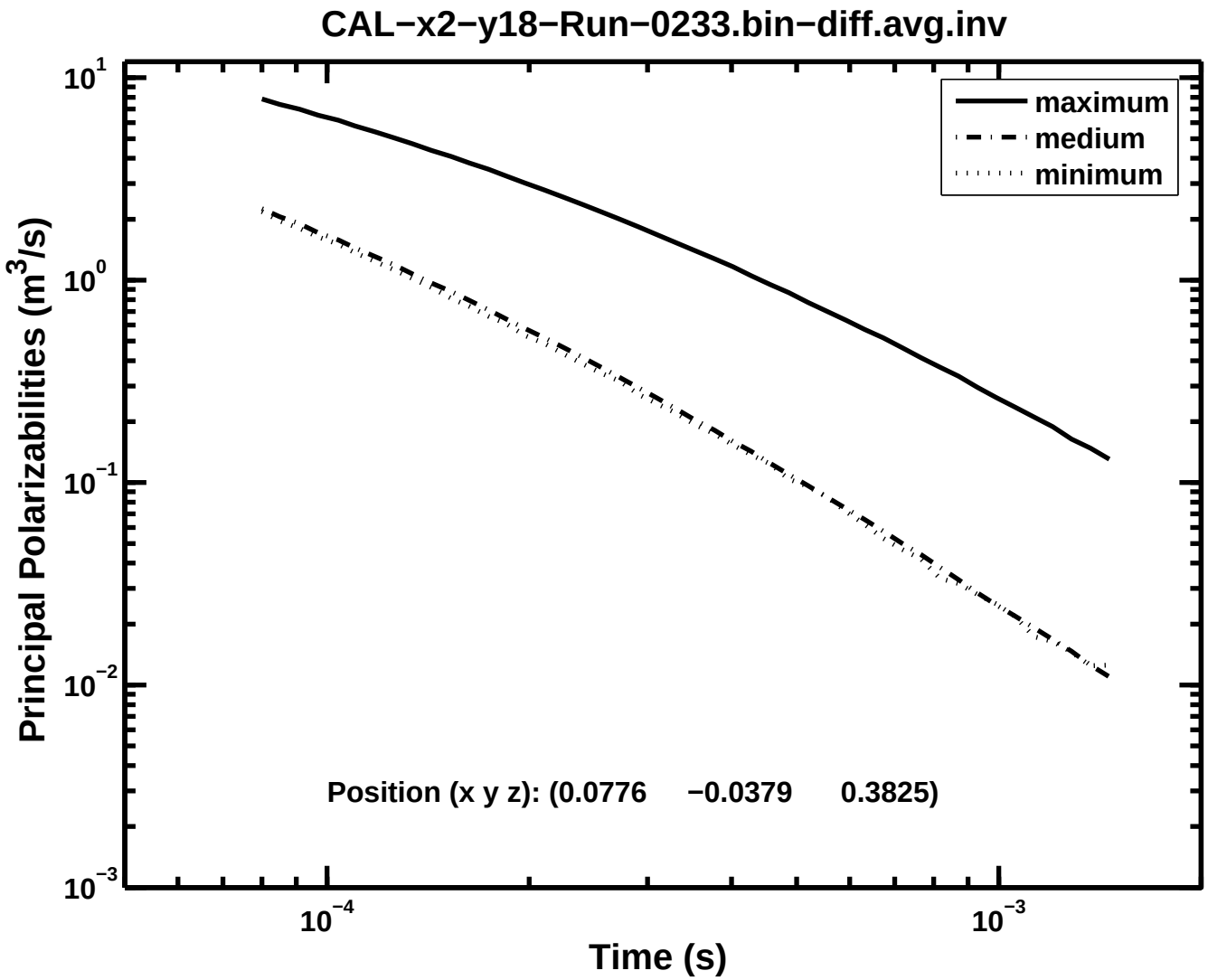
CAL−x2−y18−Run−0233.bin−diff.avg.inv
maximum
medium
minimum
Principal Polarizabilities (m3/s)
10^1
10^0
10^−1
10^−2
10^−3
Position (x y z): (0.0776 −0.0379 0.3825)
10^−4
10^−3
Time (s)

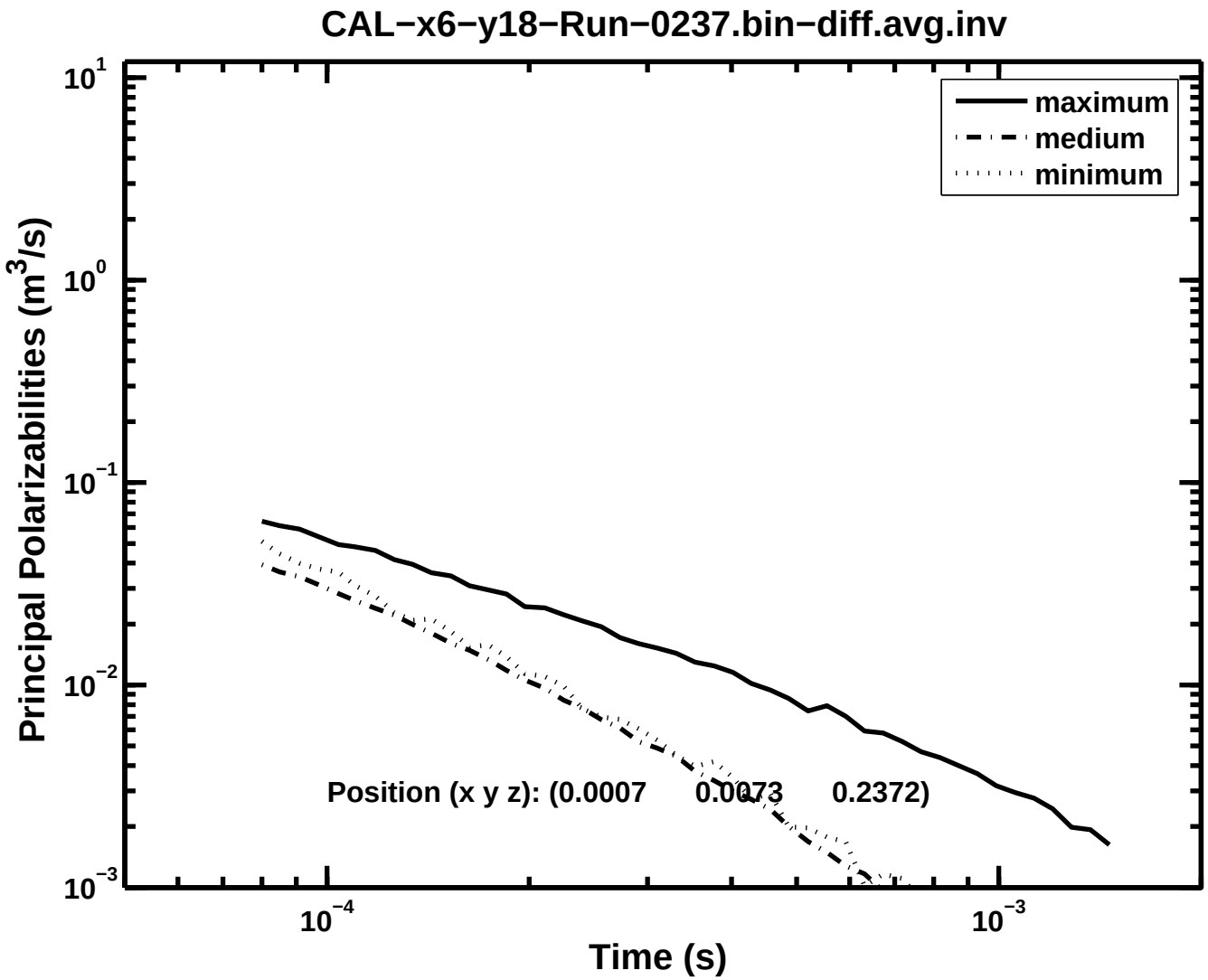
CAL−x6−y18−Run−0237.bin−diff.avg.inv
maximum
medium
minimum
Principal Polarizabilities (m3/s)
10^1
10^0
10^−1
10^−2
10^−3
Position (x y z): (0.0007 0.0073 0.2372)
10^−4
10^−3
Time (s)

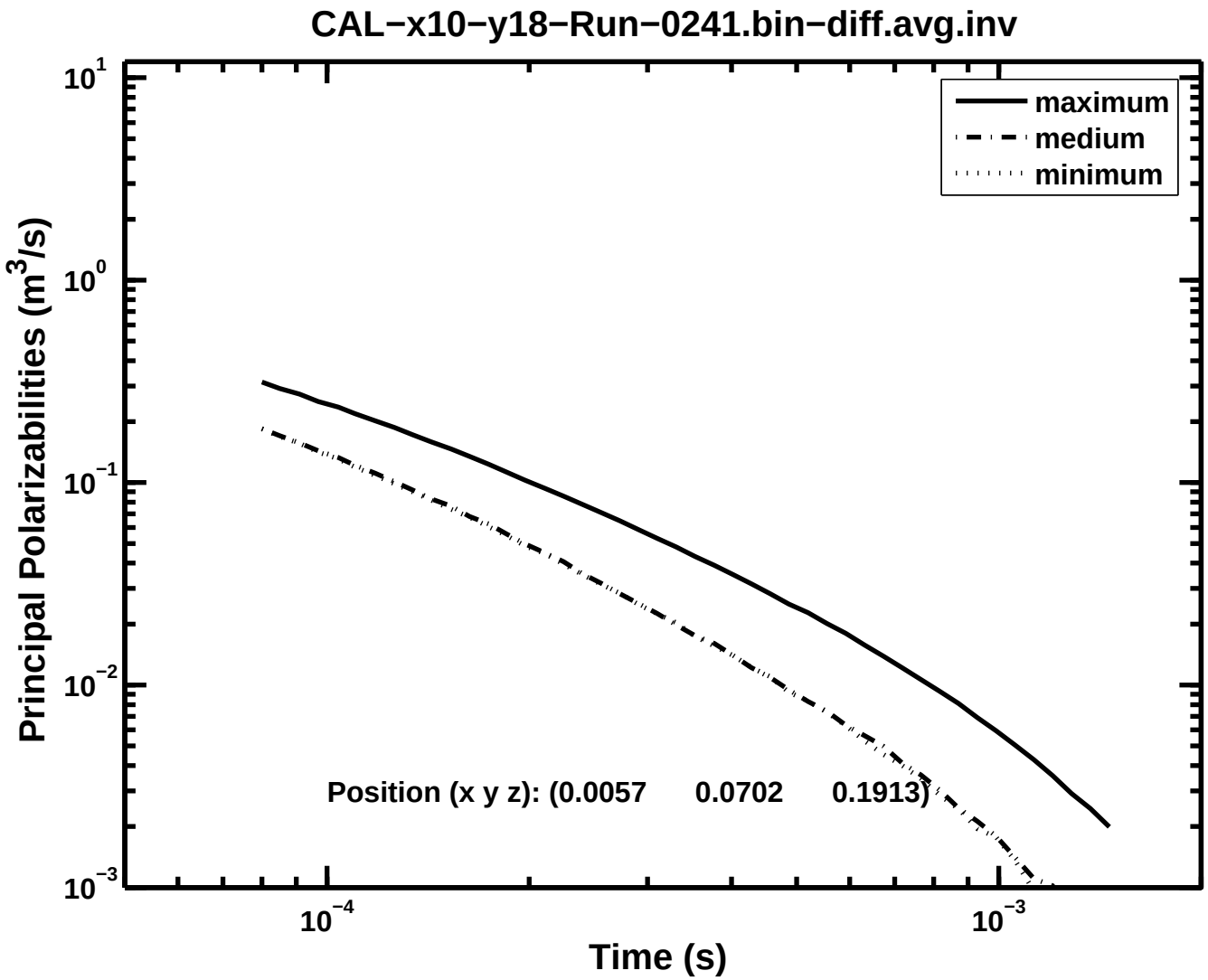
CAL−x10−y18−Run−0241.bin−diff.avg.inv
maximum
medium
minimum
Principal Polarizabilities (m3/s)
10^1
10^0
10^−1
10^−2
10^−3
Position (x y z): (0.0057 0.0702 0.1913)
10^−4
10^−3
Time (s)

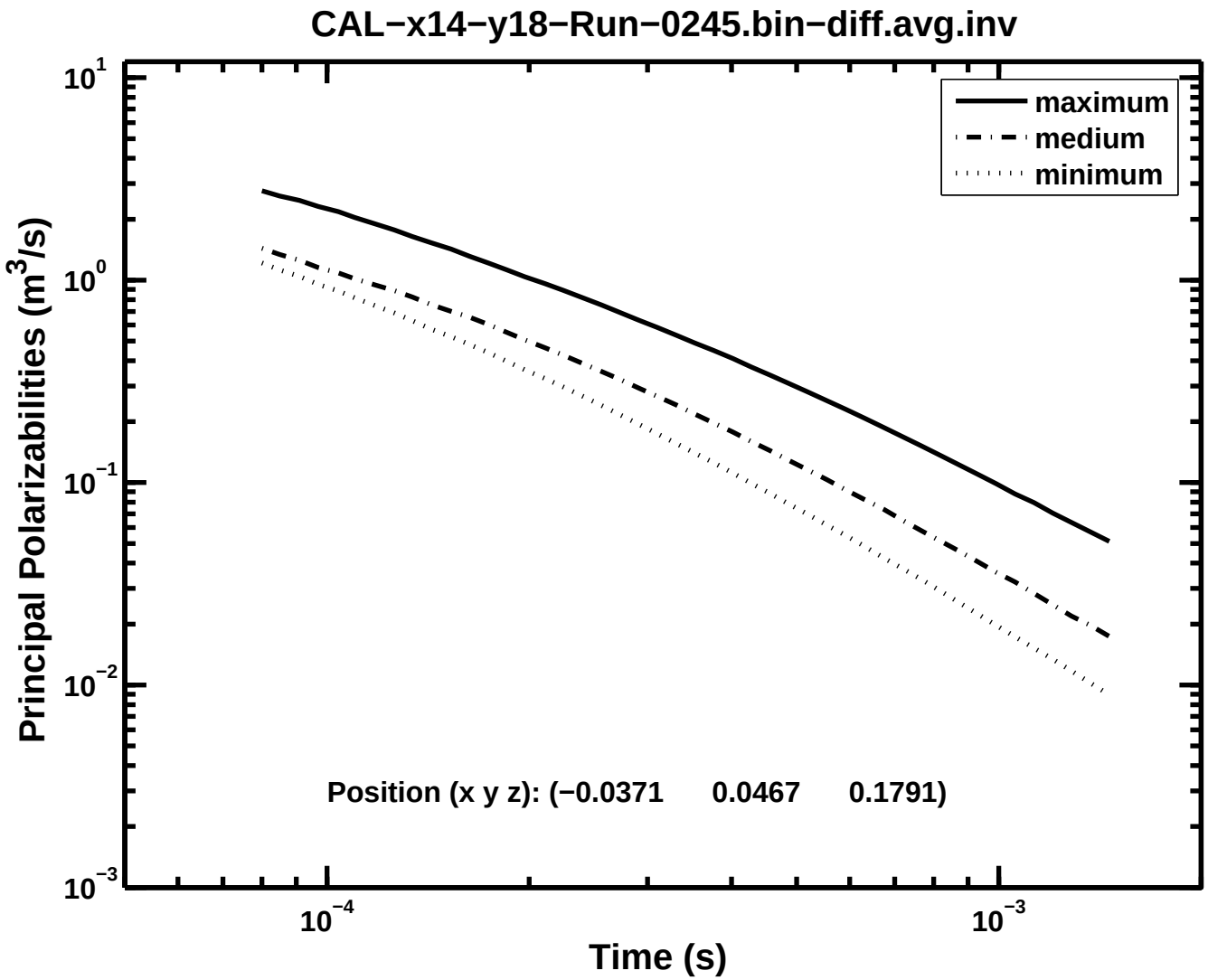
CAL−x14−y18−Run−0245.bin−diff.avg.inv
maximum
medium
minimum
Principal Polarizabilities (m3/s)
10^1
10^0
10^−1
10^−2
10^−3
Position (x y z): (−0.0371 0.0467 0.1791)
10^−4
10^−3
Time (s)

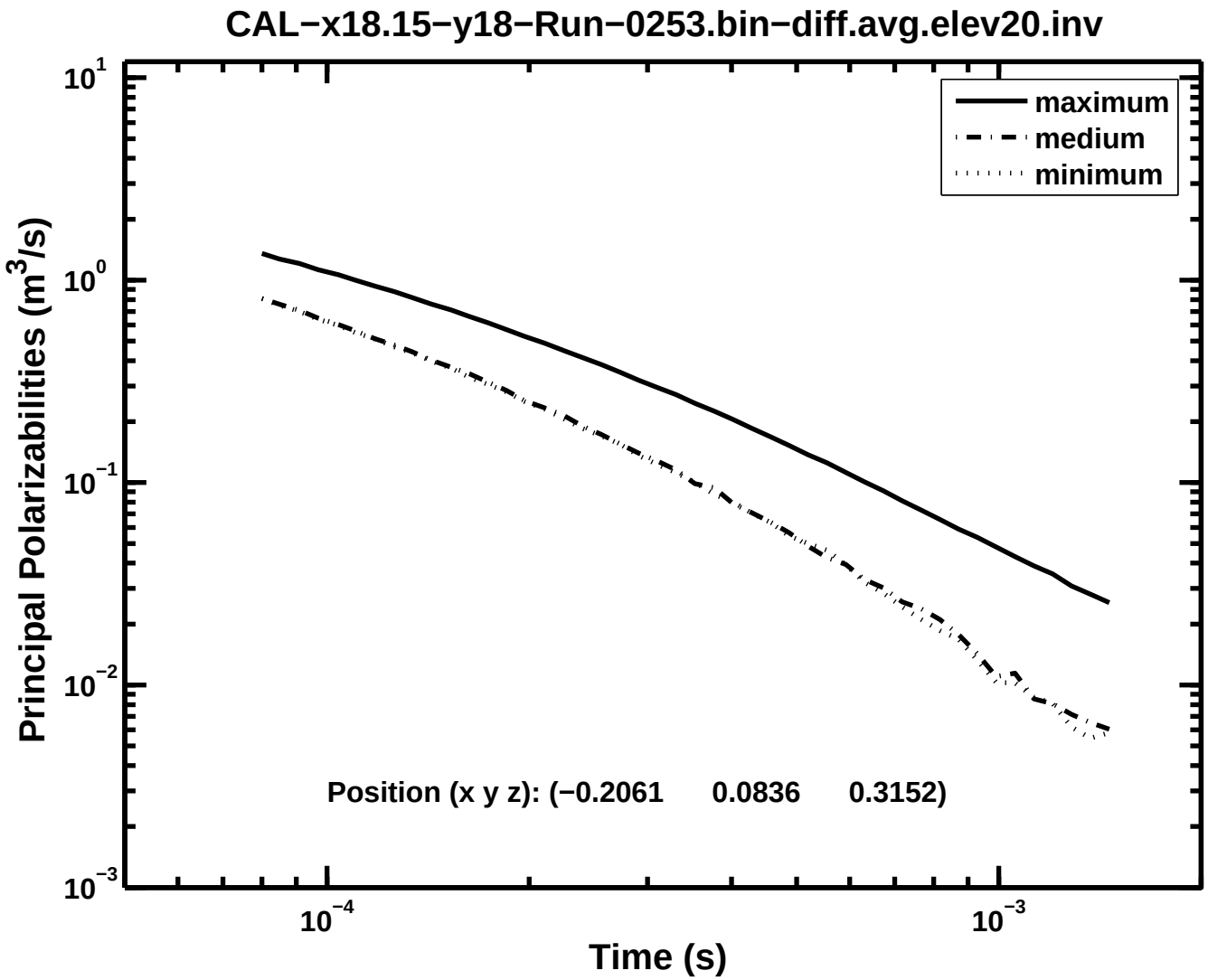
CAL−x18.15−y18−Run−0253.bin−diff.avg.elev20.inv
maximum
medium
minimum
Principal Polarizabilities (m3/s)
10^1
10^0
10^−1
10^−2
10^−3
Position (x y z): (−0.2061 0.0836 0.3152)
10^−4
10^−3
Time (s)

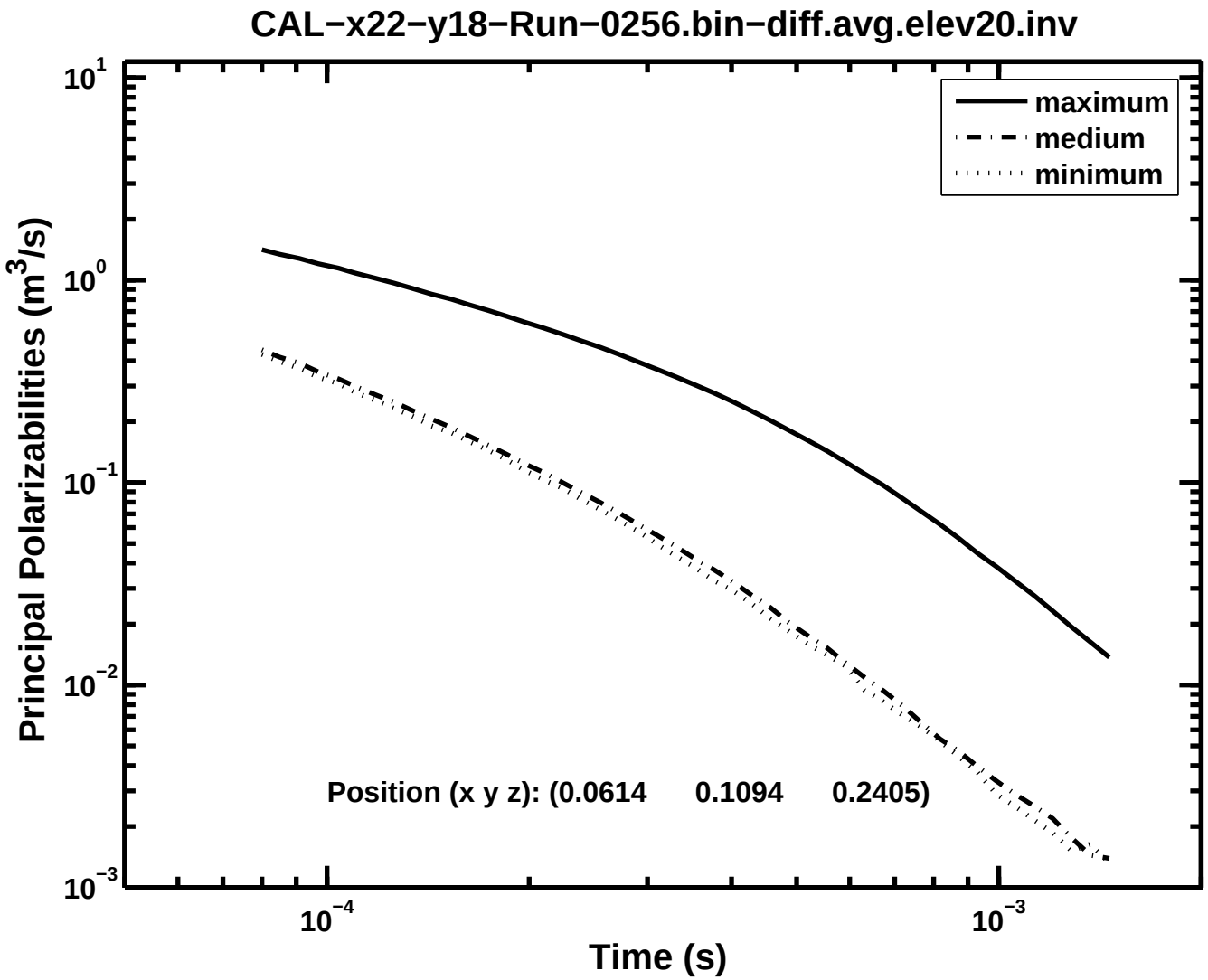
CAL−x22−y18−Run−0256.bin−diff.avg.elev20.inv
maximum
medium
minimum
Principal Polarizabilities (m3/s)
10^1
10^0
10^−1
10^−2
10^−3
Position (x y z): (0.0614 0.1094 0.2405)
10^−4
10^−3
Time (s)

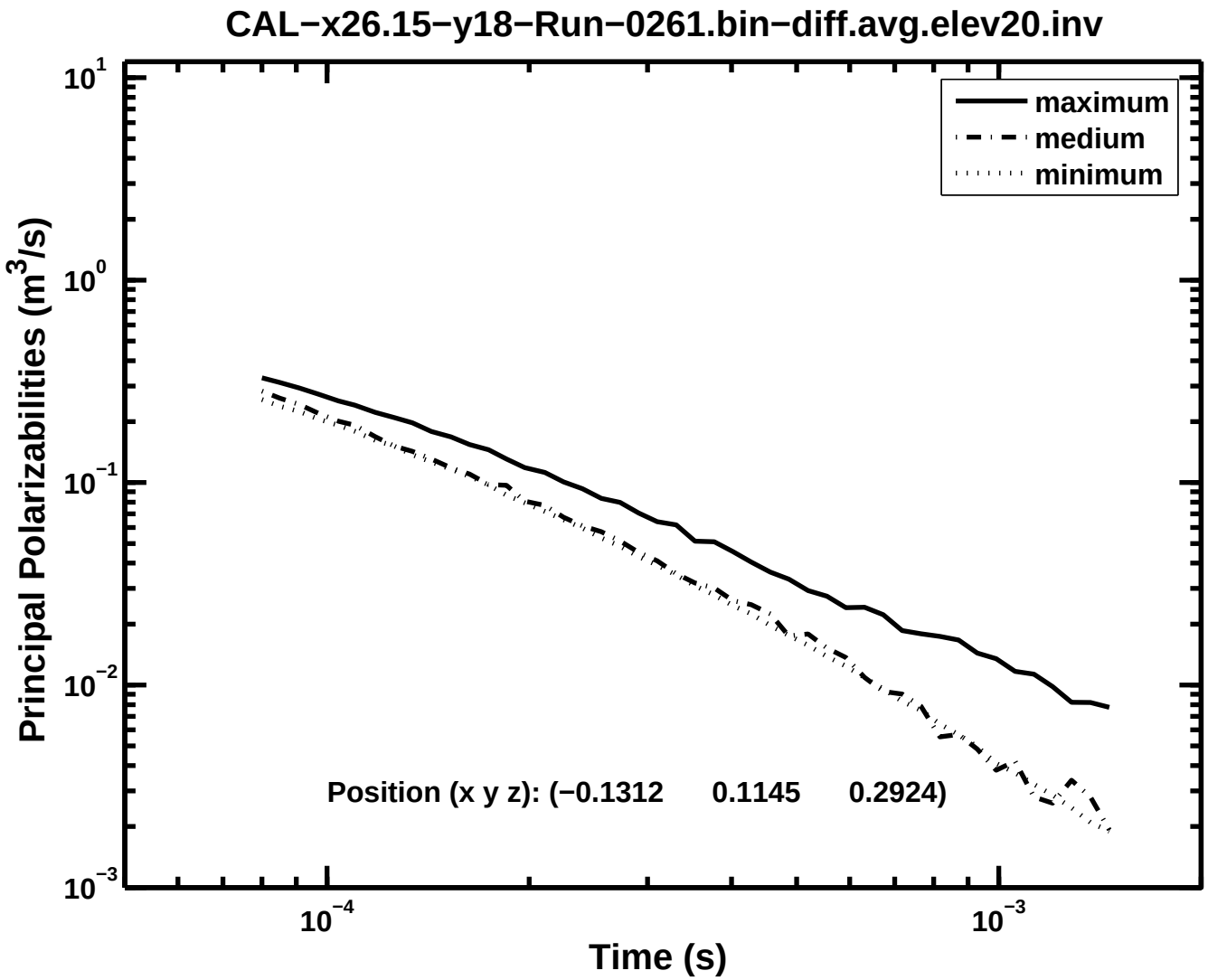
CAL−x26.15−y18−Run−0261.bin−diff.avg.elev20.inv
maximum
medium
minimum
Principal Polarizabilities (m3/s)
10^1
10^0
10^−1
10^−2
10^−3
Position (x y z): (−0.1312 0.1145 0.2924)
10^−4
10^−3
Time (s)

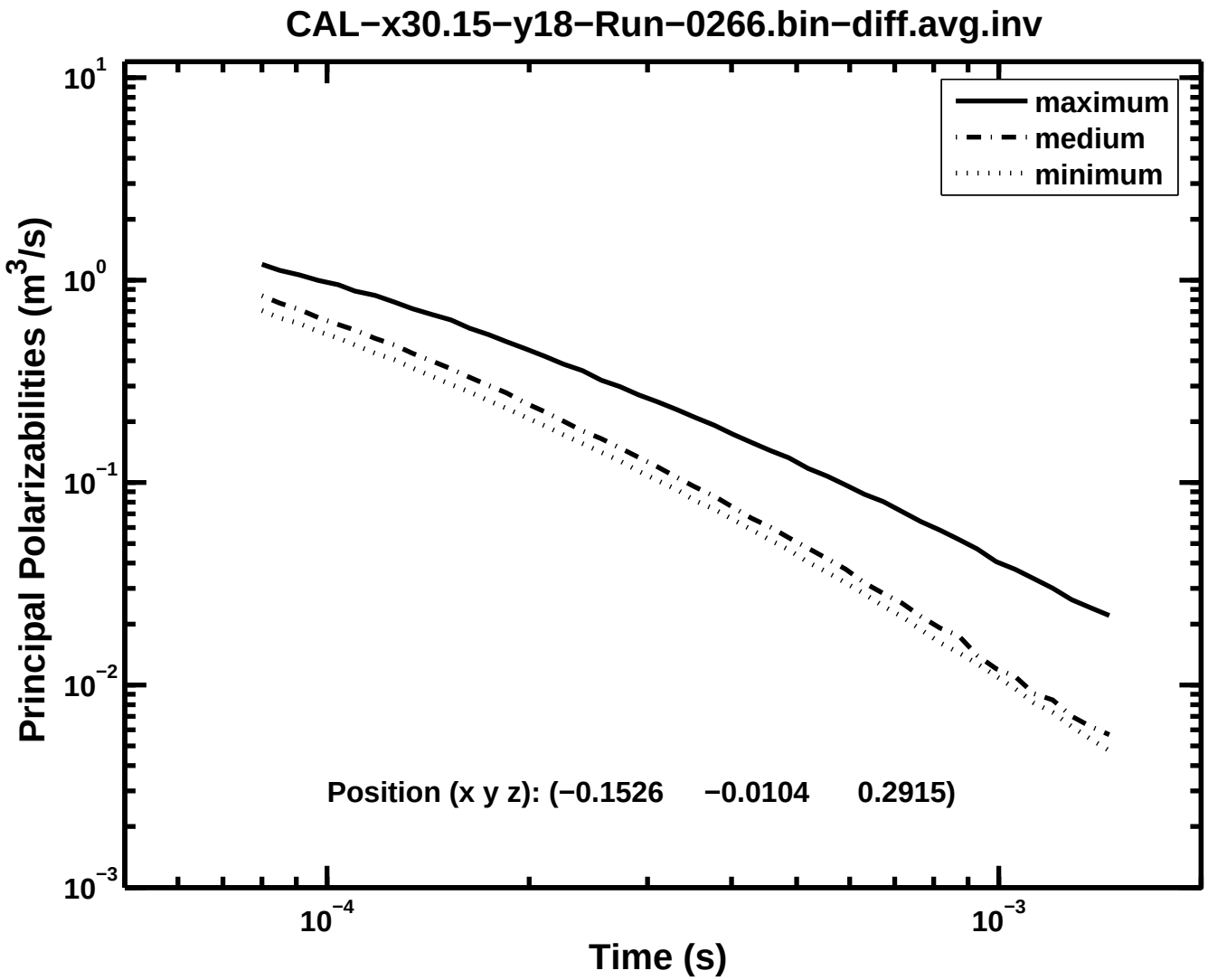
CAL−x30.15−y18−Run−0266.bin−diff.avg.inv
maximum
medium
minimum
Principal Polarizabilities (m3/s)
10^1
10^0
10^−1
10^−2
10^−3
Position (x y z): (−0.1526 −0.0104 0.2915)
10^−4
10^−3
Time (s)

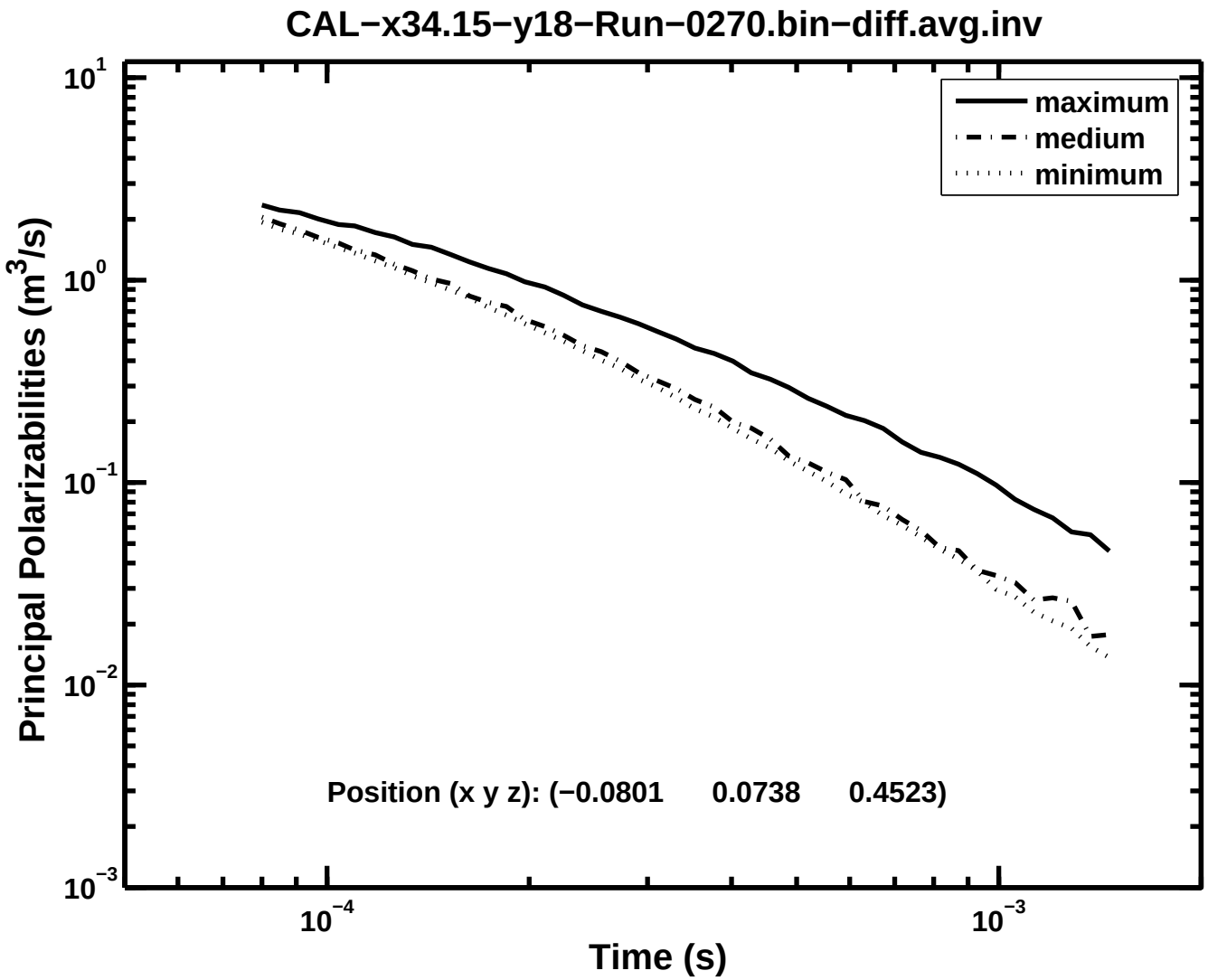
CAL−x34.15−y18−Run−0270.bin−diff.avg.inv
maximum
medium
minimum
Principal Polarizabilities (m3/s)
10^1
10^0
10^−1
10^−2
10^−3
Position (x y z): (−0.0801 0.0738 0.4523)
10^−4
10^−3
Time (s)

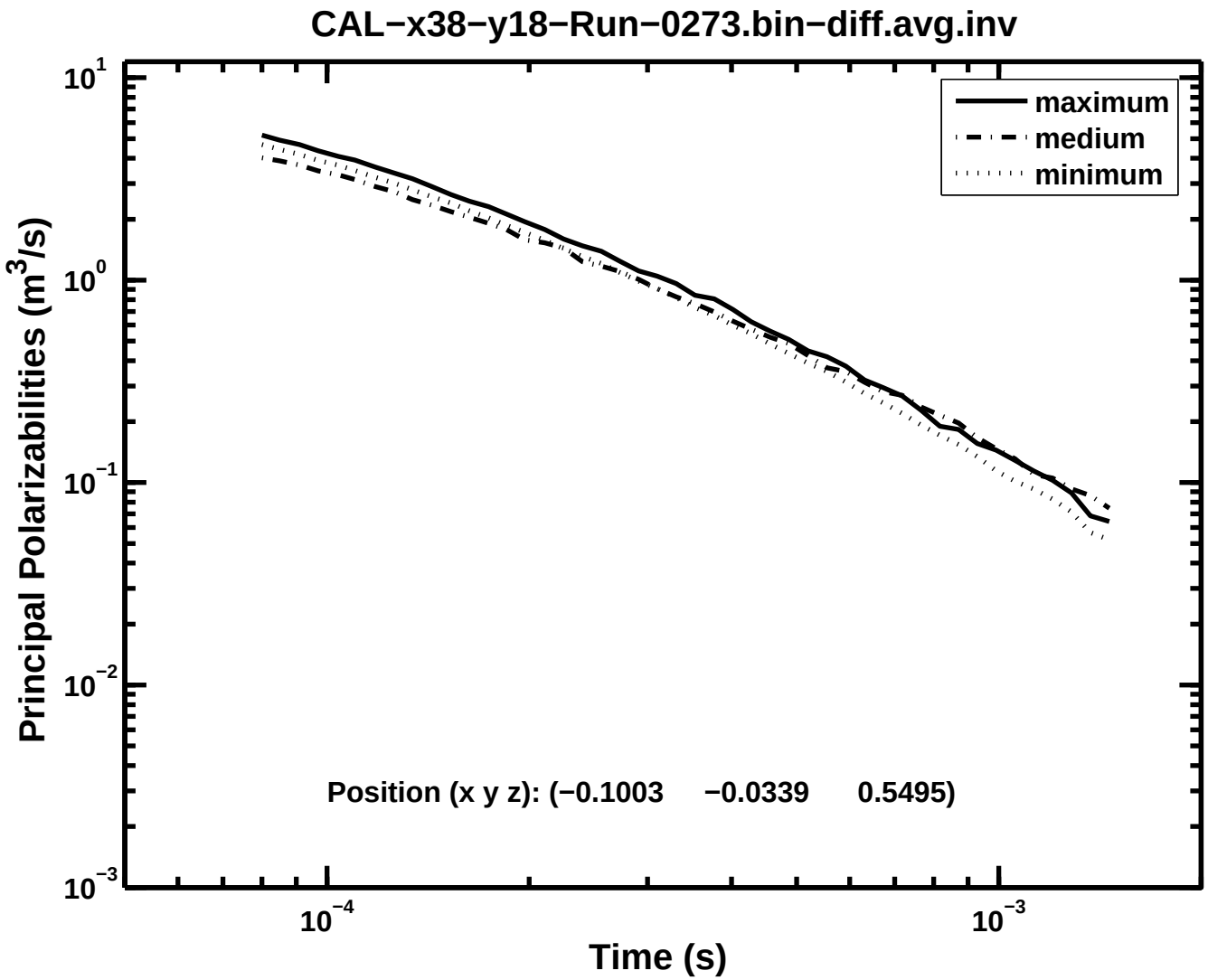
CAL−x38−y18−Run−0273.bin−diff.avg.inv
maximum
medium
minimum
Principal Polarizabilities (m3/s)
10^1
10^0
10^−1
10^−2
10^−3
Position (x y z): (−0.1003 −0.0339 0.5495)
10^−4
10^−3
Time (s)

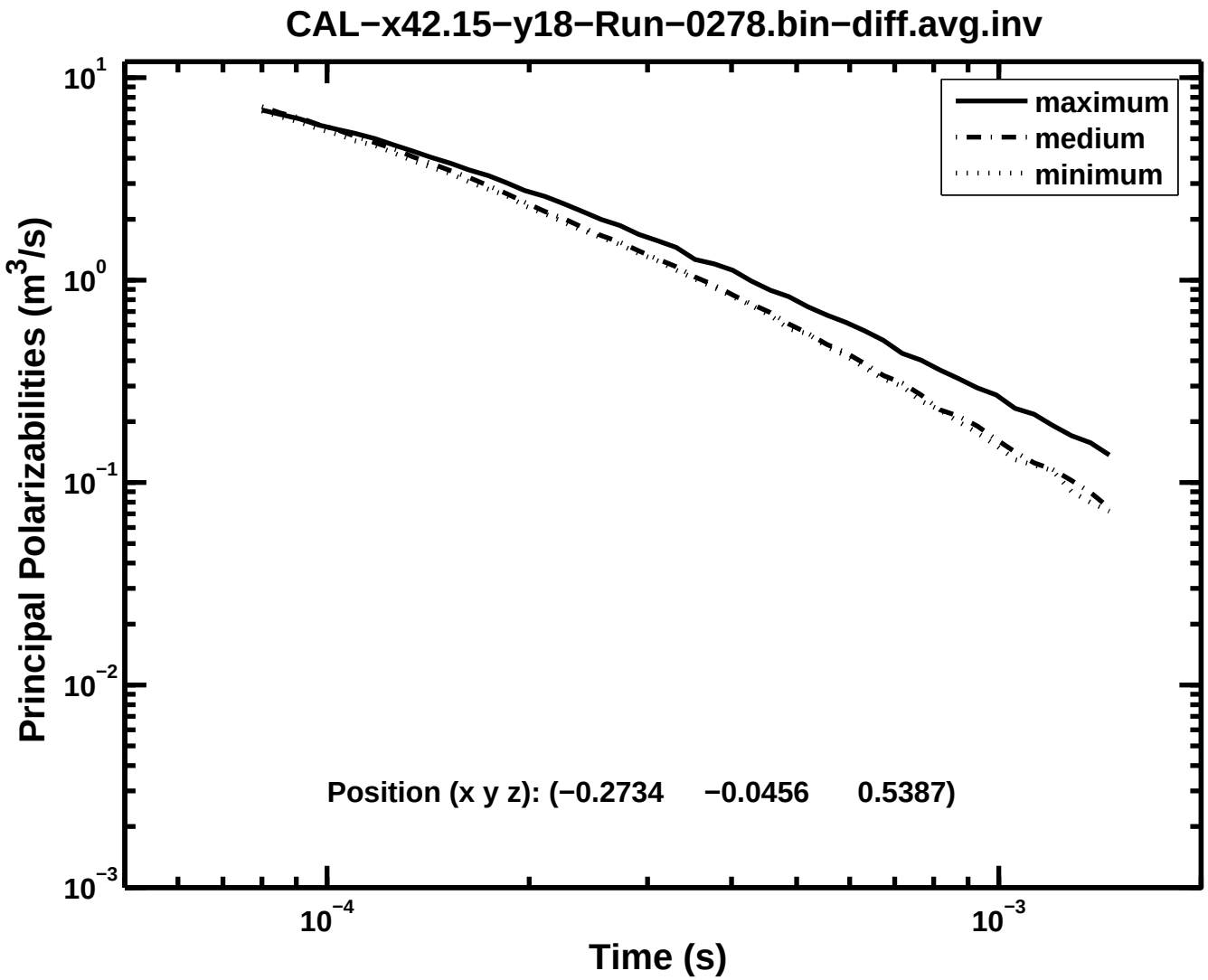
CAL−x42.15−y18−Run−0278.bin−diff.avg.inv
maximum
medium
minimum
Principal Polarizabilities (m3/s)
10^1
10^0
10^−1
10^−2
10^−3
Position (x y z): (−0.2734 −0.0456 0.5387)
10^−4
10^−3
Time (s)

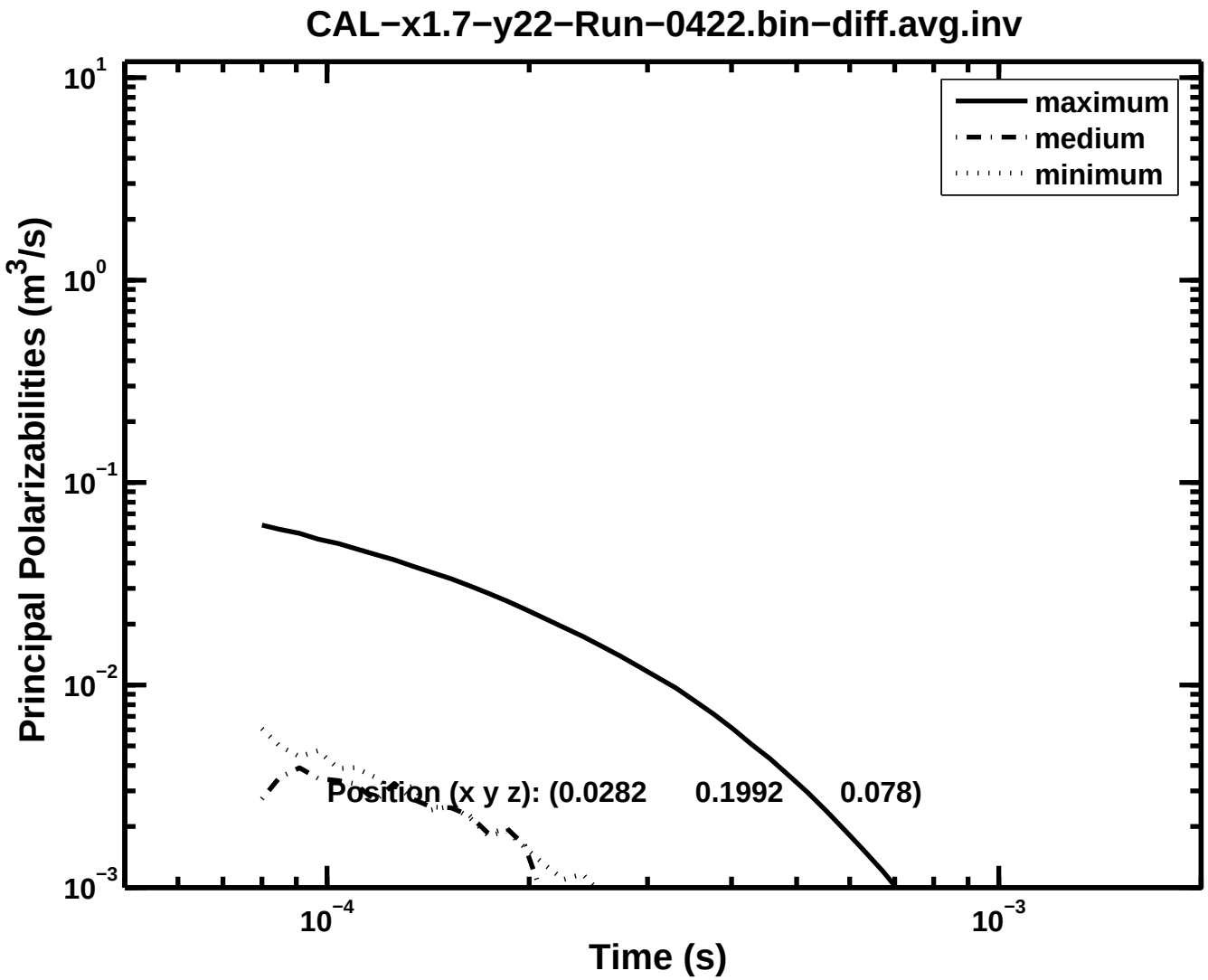
CAL−x1.7−y22−Run−0422.bin−diff.avg.inv
maximum
medium
minimum
Principal Polarizabilities (m3/s)
10^1
10^0
10^−1
10^−2
10^−3
Position (x y z): (0.0282 0.1992 0.078)
10^−4
10^−3
Time (s)

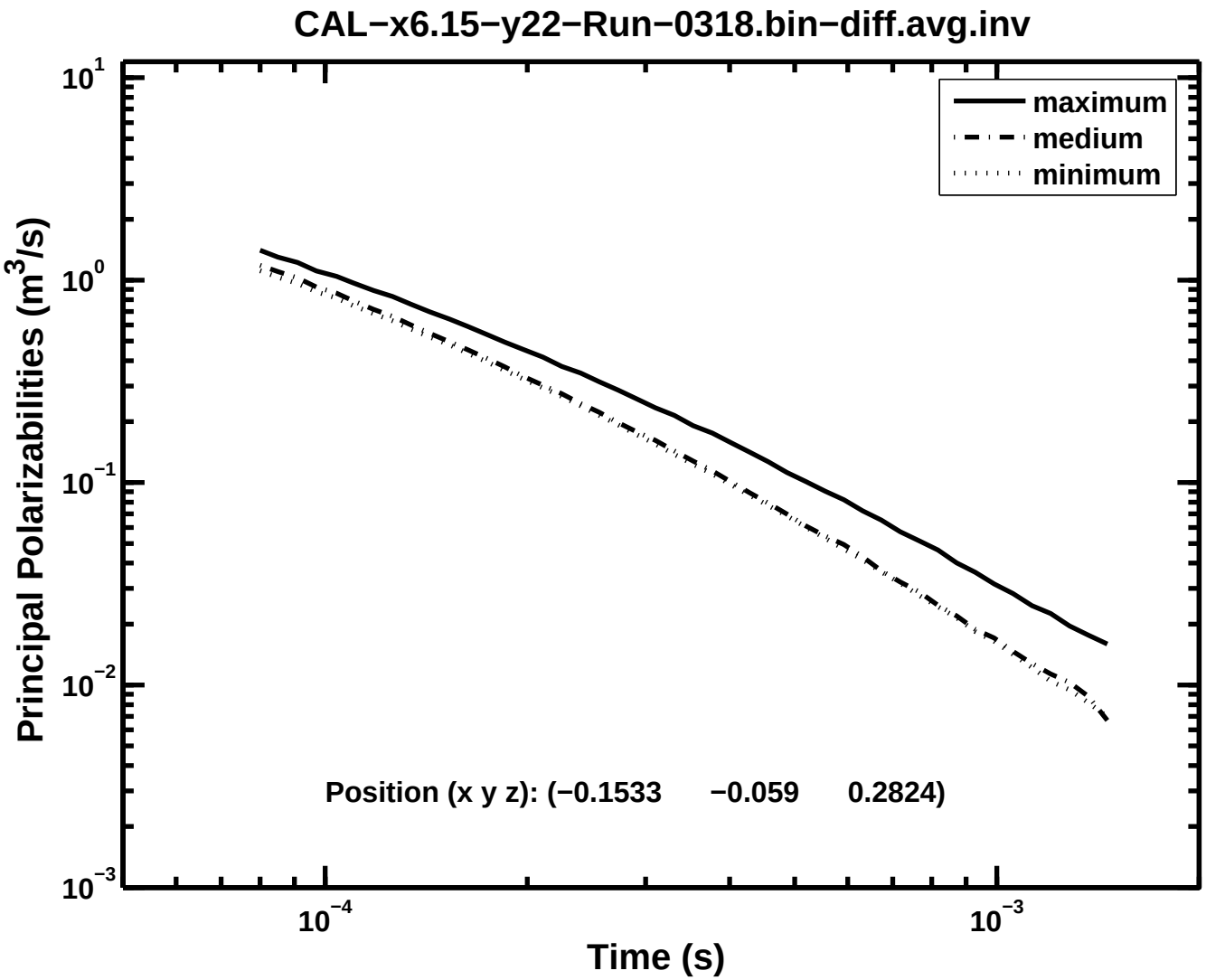
CAL−x6.15−y22−Run−0318.bin−diff.avg.inv
maximum
medium
minimum
Principal Polarizabilities (m3/s)
10^1
10^0
10^−1
10^−2
10^−3
Position (x y z): (−0.1533 −0.059 0.2824)
10^−4
10^−3
Time (s)

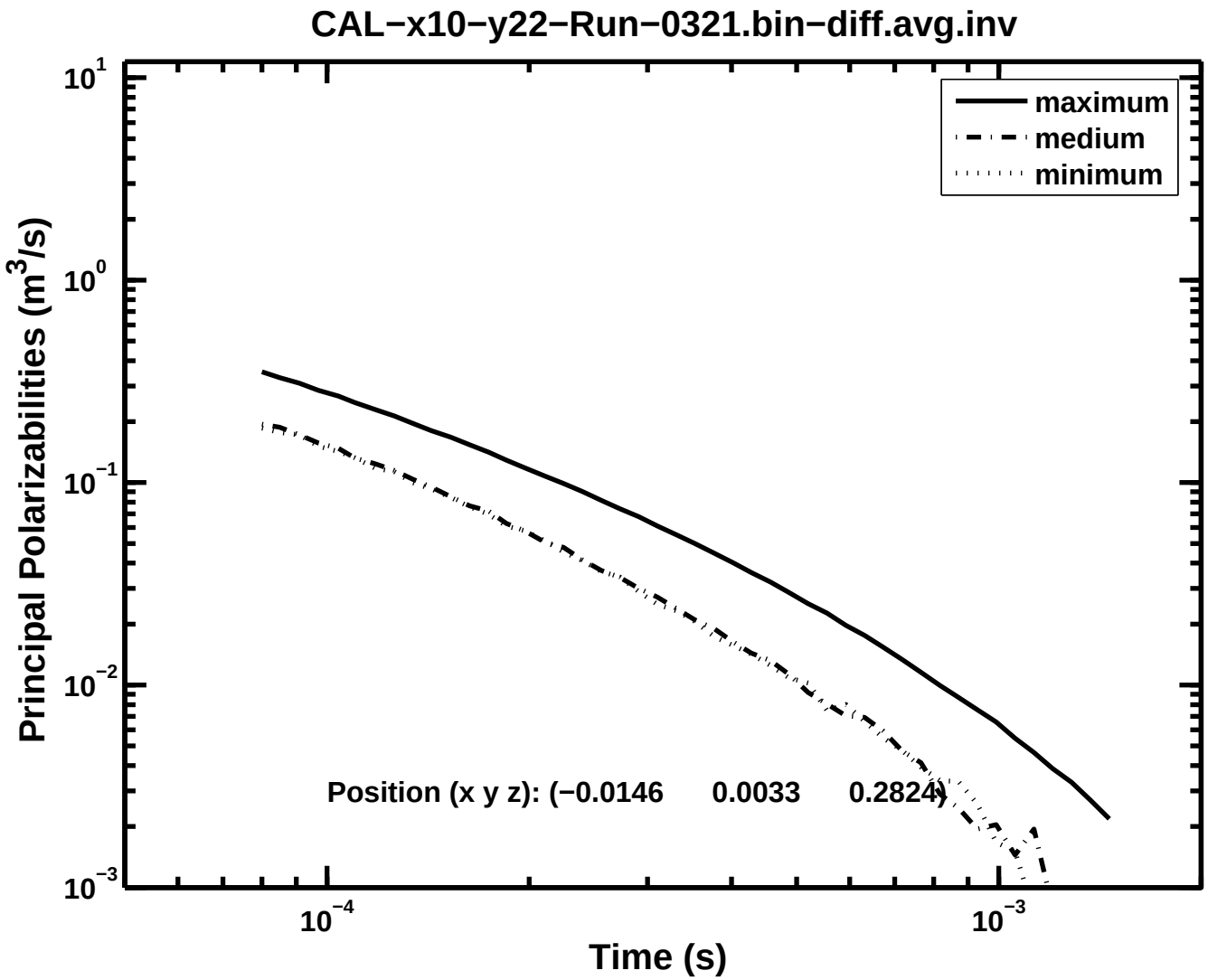
CAL−x10−y22−Run−0321.bin−diff.avg.inv
maximum
medium
minimum
Principal Polarizabilities (m3/s)
10^1
10^0
10^−1
10^−2
10^−3
Position (x y z): (−0.0146 0.0033 0.2824)
10^−4
10^−3
Time (s)

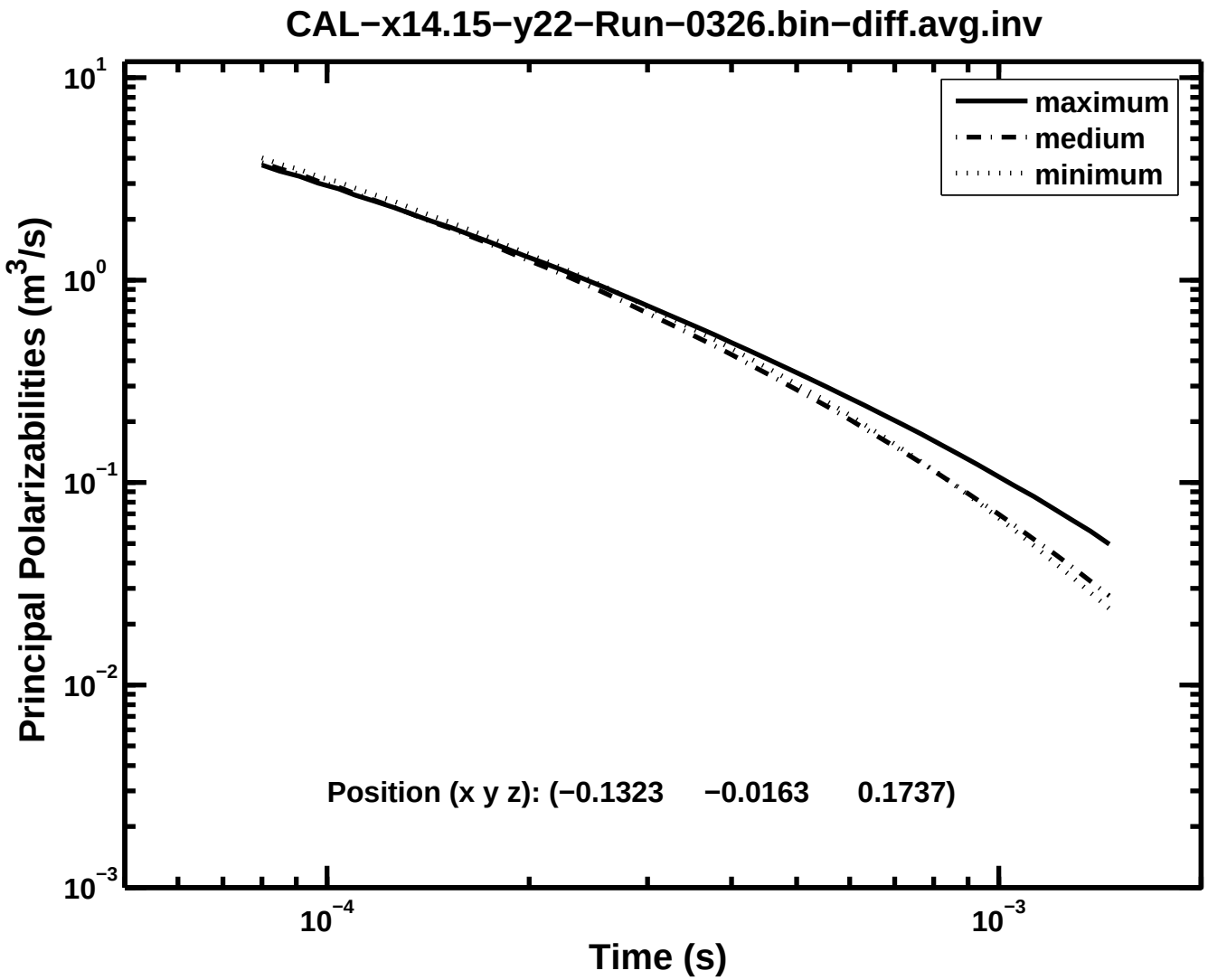
CAL−x14.15−y22−Run−0326.bin−diff.avg.inv
maximum
medium
minimum
Principal Polarizabilities (m3/s)
10^1
10^0
10^−1
10^−2
10^−3
Position (x y z): (−0.1323 −0.0163 0.1737)
10^−4
10^−3
Time (s)

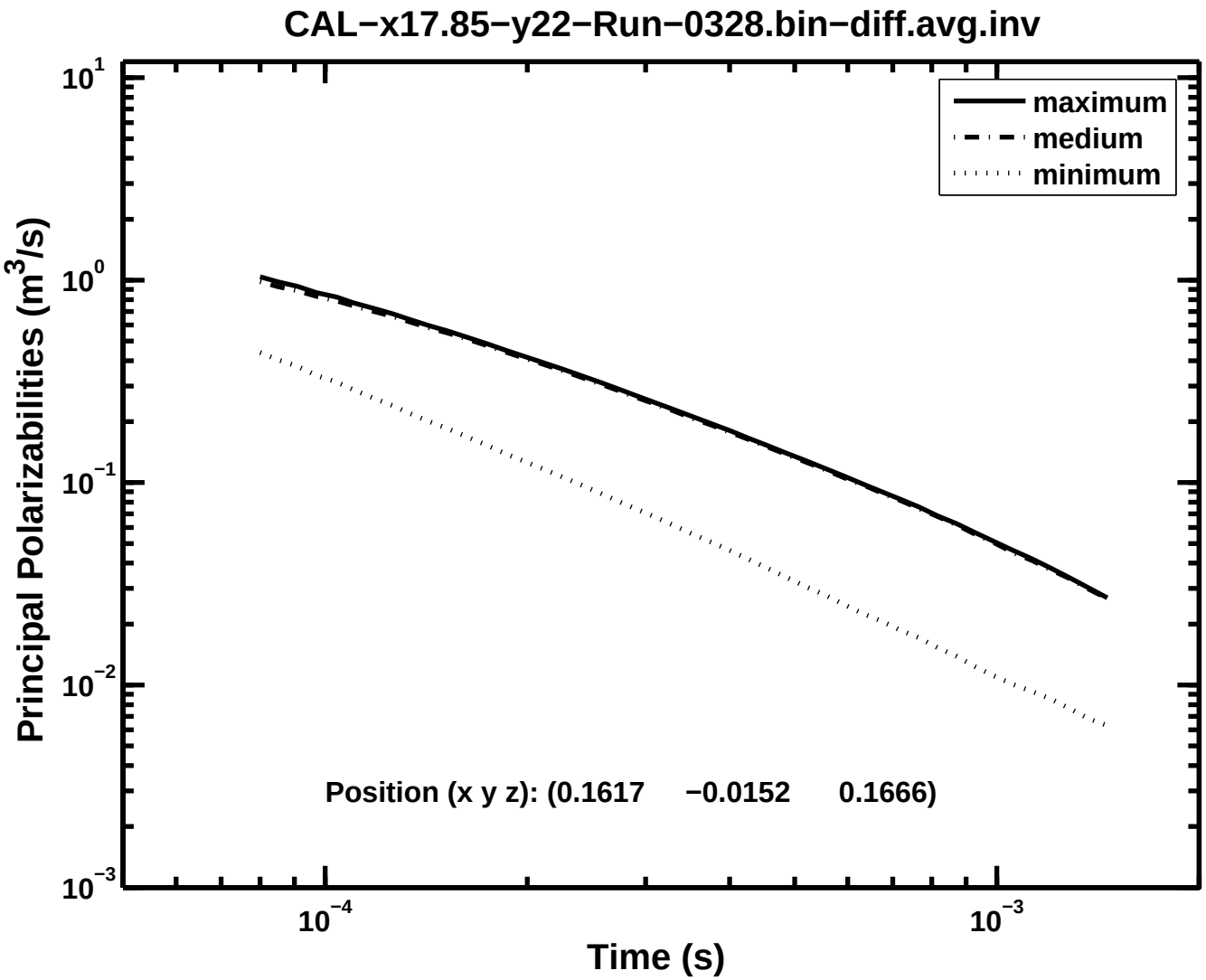
CAL−x17.85−y22−Run−0328.bin−diff.avg.inv
maximum
medium
minimum
Principal Polarizabilities (m3/s)
10^1
10^0
10^−1
10^−2
10^−3
Position (x y z): (0.1617 −0.0152 0.1666)
10^−4
10^−3
Time (s)

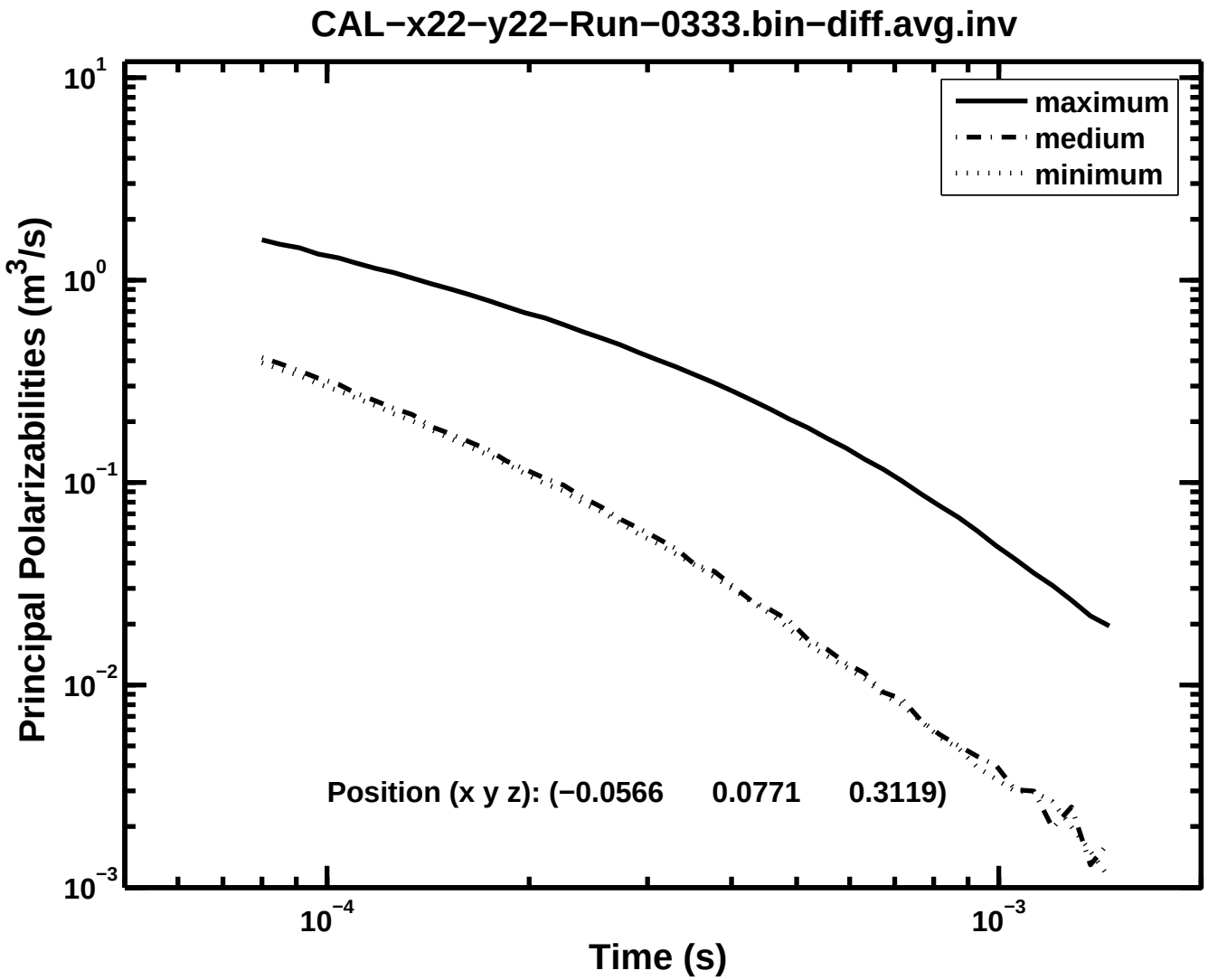
CAL−x22−y22−Run−0333.bin−diff.avg.inv
maximum
medium
minimum
Principal Polarizabilities (m3/s)
10^1
10^0
10^−1
10^−2
10^−3
Position (x y z): (−0.0566 0.0771 0.3119)
10^−4
10^−3
Time (s)

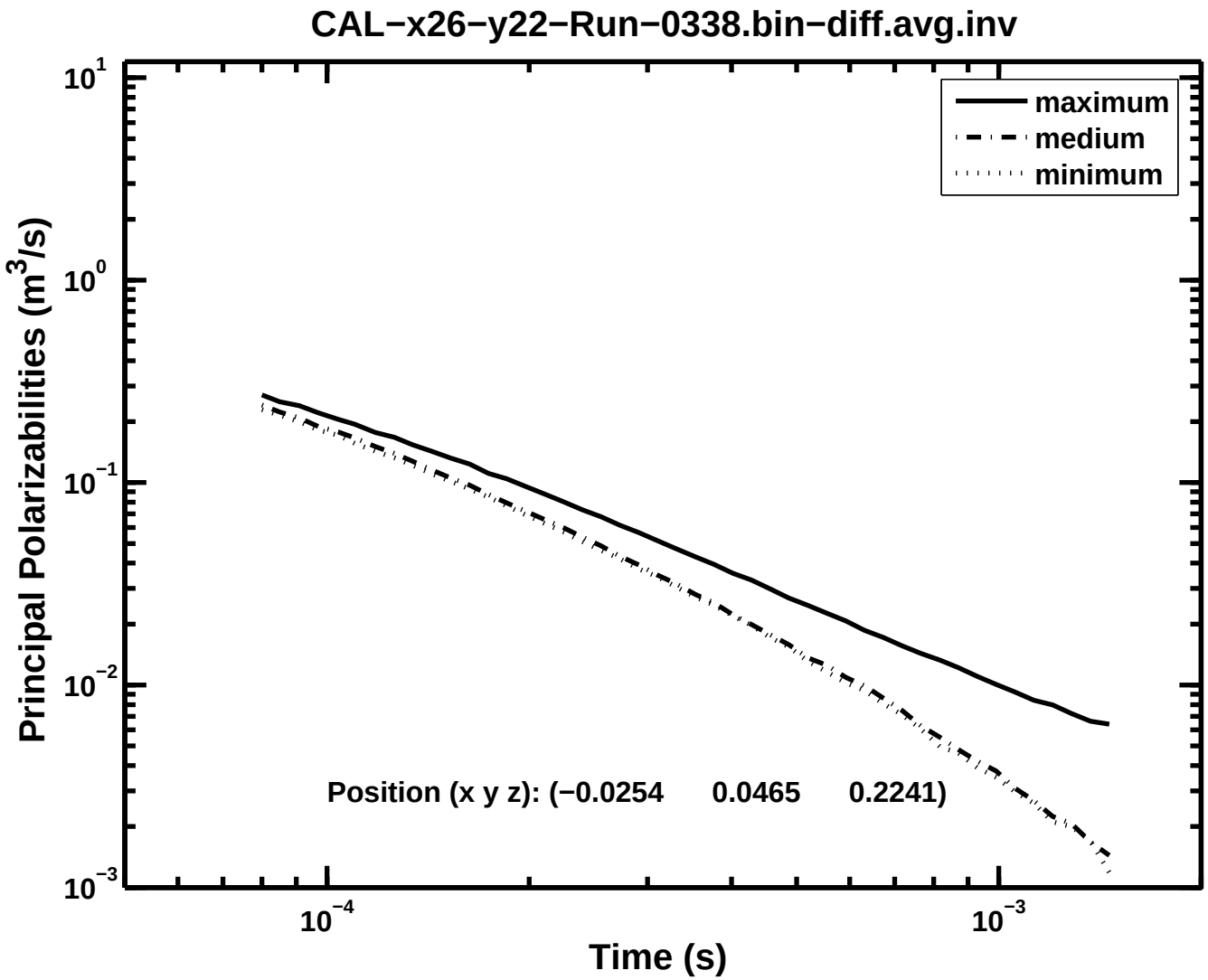
CAL−x26−y22−Run−0338.bin−diff.avg.inv
maximum
medium
minimum
Principal Polarizabilities (m3/s)
10^1
10^0
10^−1
10^−2
10^−3
Position (x y z): (−0.0254 0.0465 0.2241)
10^−4
10^−3
Time (s)

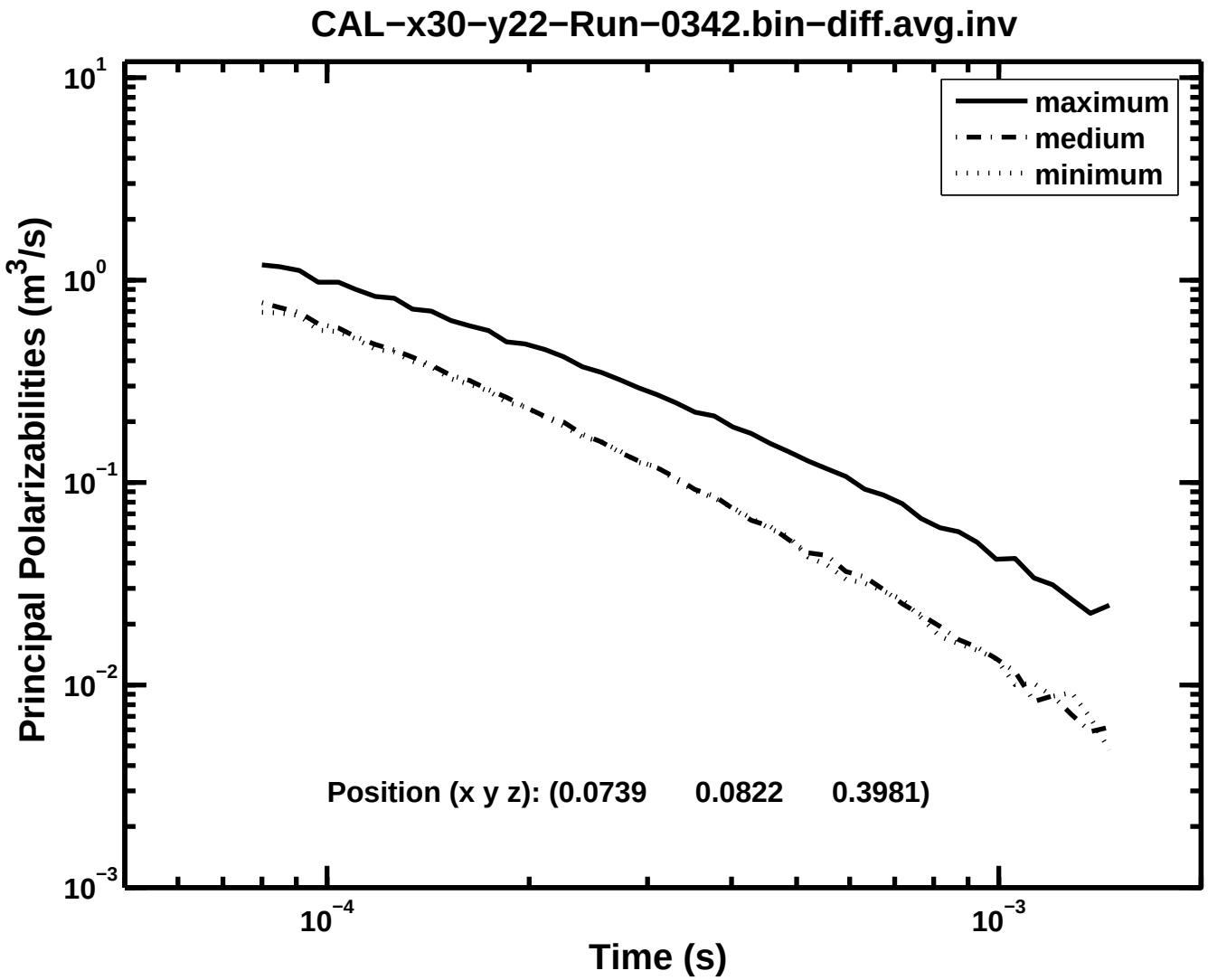
CAL−x30−y22−Run−0342.bin−diff.avg.inv
maximum
medium
minimum
Principal Polarizabilities (m3/s)
10^1
10^0
10^−1
10^−2
10^−3
Position (x y z): (0.0739 0.0822 0.3981)
10^−4
10^−3
Time (s)

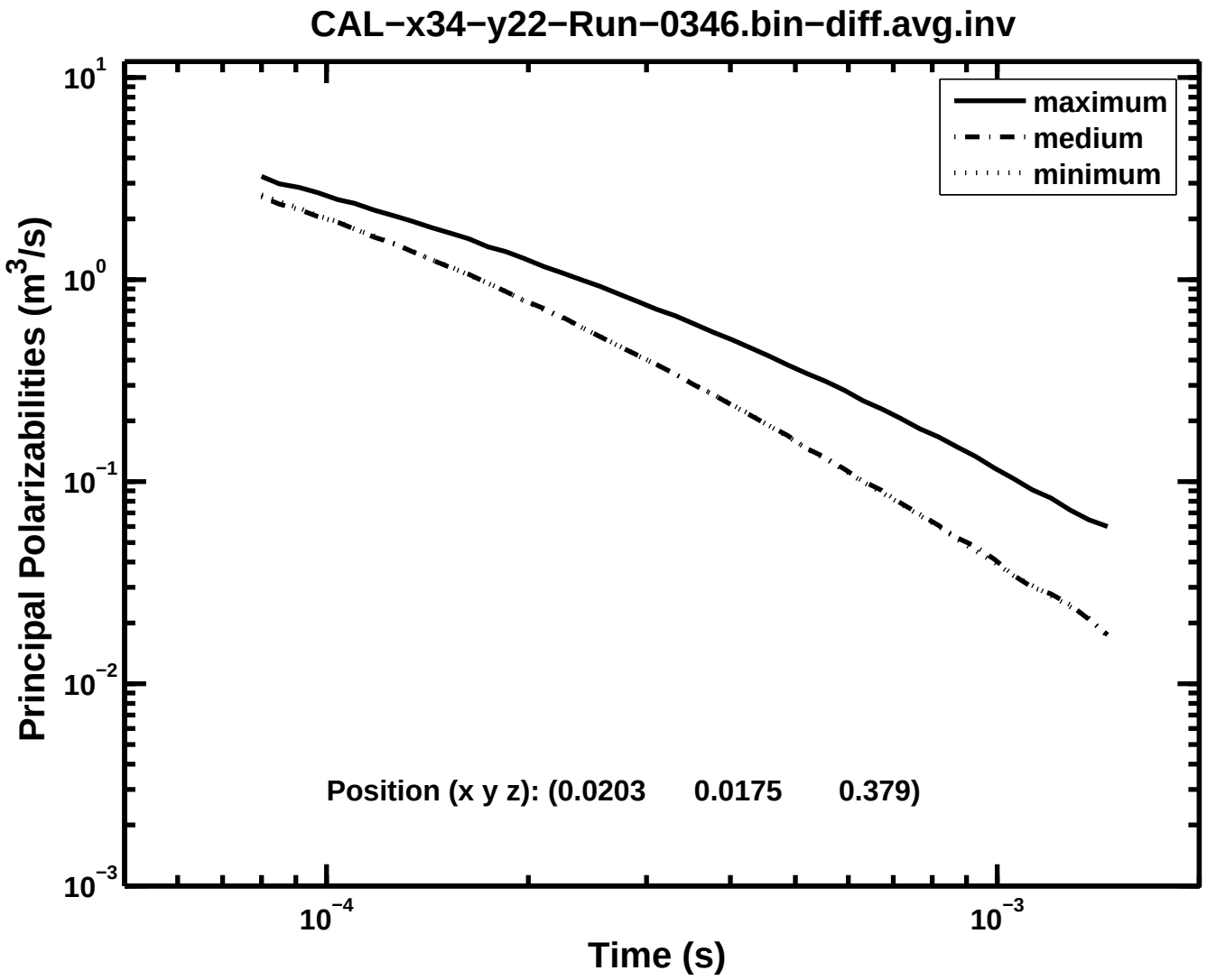
CAL−x34−y22−Run−0346.bin−diff.avg.inv
maximum
medium
minimum
Principal Polarizabilities (m3/s)
10^1
10^0
10^−1
10^−2
10^−3
Position (x y z): (0.0203 0.0175 0.379)
10^−4
10^−3
Time (s)

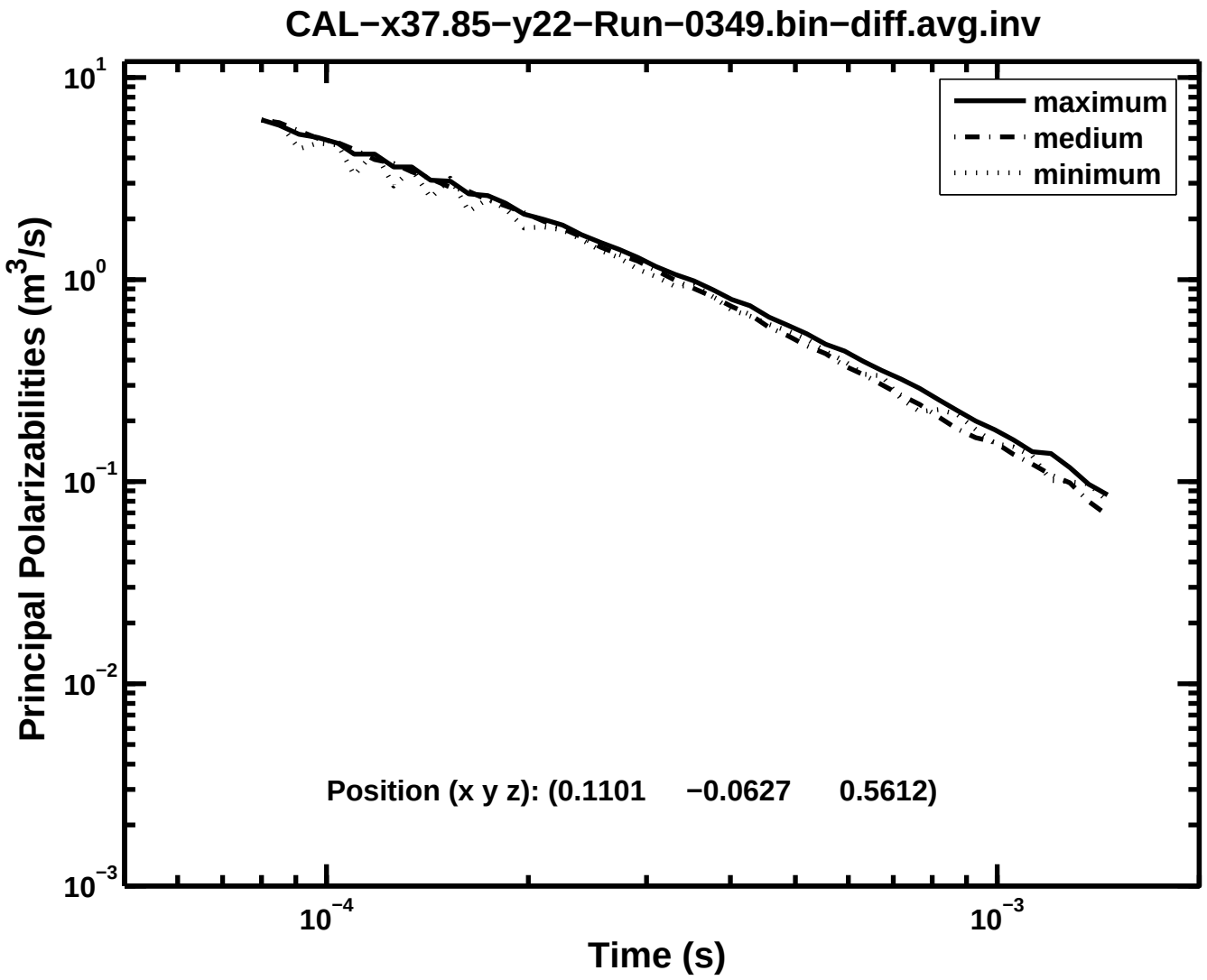
CAL−x37.85−y22−Run−0349.bin−diff.avg.inv
maximum
medium
minimum
Principal Polarizabilities (m3/s)
10^1
10^0
10^−1
10^−2
10^−3
Position (x y z): (0.1101 −0.0627 0.5612)
10^−4
10^−3
Time (s)

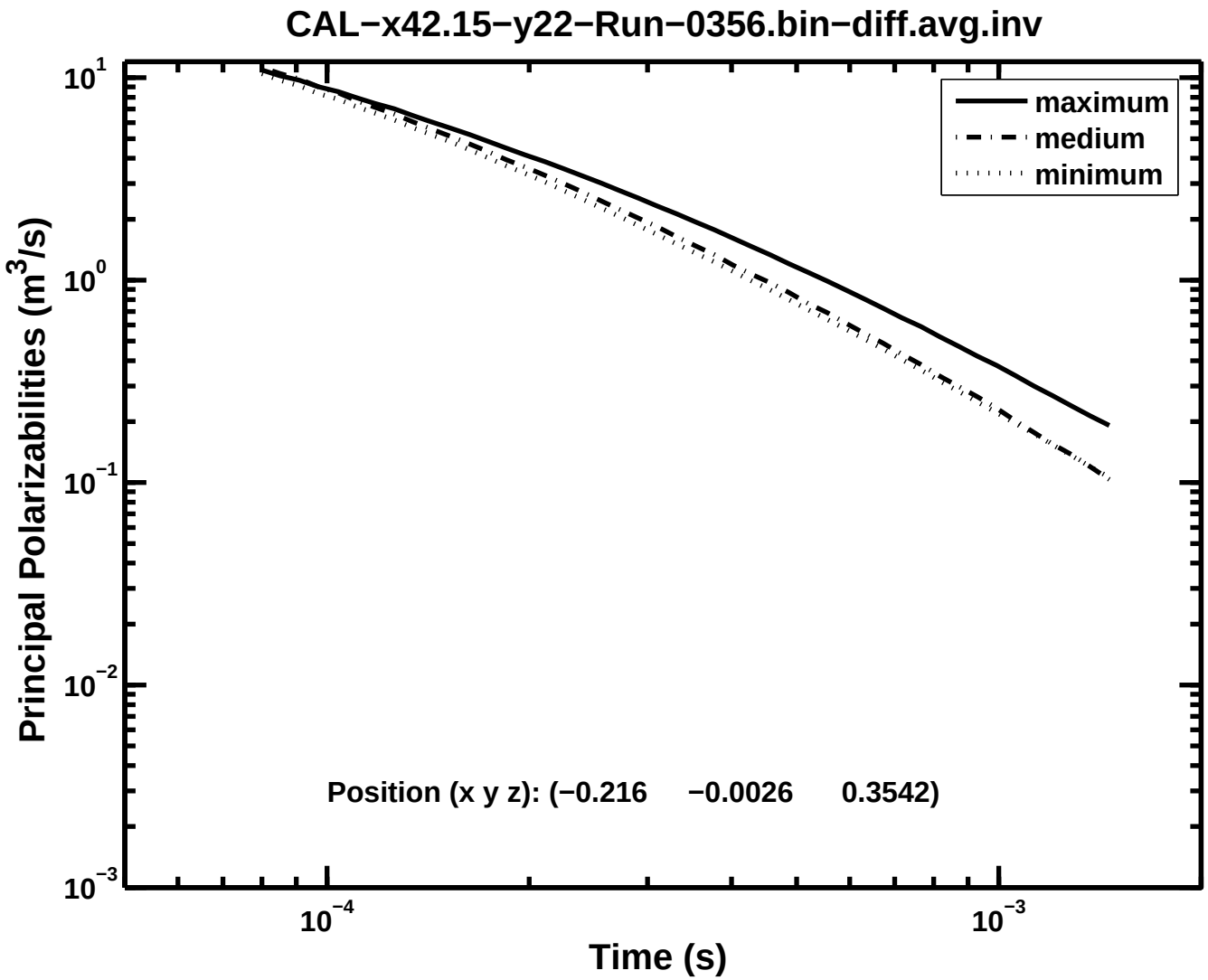
CAL−x42.15−y22−Run−0356.bin−diff.avg.inv
maximum
medium
minimum
Principal Polarizabilities (m3/s)
10^1
10^0
10^−1
10^−2
10^−3
Position (x y z): (−0.216 −0.0026 0.3542)
10^−4
10^−3
Time (s)